UNIVERSITY OF NAIROBI

EFFECT OF ANNEALING AMBIENT ON THE STRUCTURAL, OPTICAL AND ELECTRICAL PROPERTIES OF TiO_2:Ge THIN FILMS FOR PHOTOVOLTAIC APPLICATION

BY

LILIAN ANYANGA OWINO

I56/6761/2017

DEPARTMENT OF PHYSICS

A Thesis Submitted in Partial Fulfillment of the Requirements for the Degree of Master of Science in Physics of the University of Nairobi

May, 2021.

DECLARATION

I declare this thesis my original work and has not been submitted elsewhere for examination in the form of dissertation or thesis leading to the award of a degree. Where other people's work or my own work has been used, this has appropriately been acknowledged and referenced in accordance with the University of Nairobi's requirements.

Signature: Date: 3/05/2021

LILIAN ANYANGA OWINO

I56/6761/2017

Department of Physics, University of Nairobi

The thesis has been submitted for examination with our approval as supervisors:

	Signature	Date
Dr. Sebastian Waita		7th May, 2021
Department of Physics, University of Nairobi swaita @uonbi.ac.ke		
Prof. Robinson Musembi Department of Physics University of Nairobi musembirj@uonbi.ac.ke	………………	May 7, 2021
Prof. Francis Nyongesa Department of Physics University of Nairobi, fnyongesa @uonbi.ac.ke	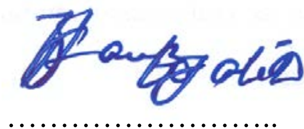 ……………………..	…May 9, 2021..

DEDICATION

This work is dedicated to my family for their support all through my study period.

ACKNOWLEDGEMENT

I want to sincerely appreciate my supervisors Dr. Sebastian Waita, Prof. Robinson Musembi and Prof. Francis Nyongesa for their guidance, encouragement and invaluable support that helped me in completion of this study. Their constant reminder that I needed to get done with research kept me on toes. I am grateful to the International Science Programme (ISP) for the provision of sponsorship for this study.

I wish to thank all members of condensed matter group, University of Nairobi for their motivation and assistance whenever I was stuck somewhere. Many thanks to Mr. Justine Nyarige, Department of Physics, University of Pretoria, South Africa, for assisting with X-ray Diffraction (XRD) and Scanning Electron Microscope (SEM) analysis of the films. I wish to thank friends and family for their moral, spiritual and financial support all through the pursuit of my Master of Science studies.

Abstract

Titanium dioxide is a wide bandgap semiconductor widely used in optoelectronics. Despite its potential application in photovoltaics, the overall efficiency of fabricated solar cells using TiO_2 is usually low due to losses through electron-hole recombination. Introduction of defects such as the use of dopants in the TiO_2 structure has been used to overcome some of these limitations. However, some of the dopants used still acts as sites of recombination for the generated electron-hole pair. In this study, pure TiO_2 and TiO_2:Ge composite thin films of varying Ge concentration (5%, 10%,and 15%) were deposited on conducting glass substrates by radio frequency sputtering technique at ambient temperature of 23 °C -25 °C under optimum sputtering power of 200 W and argon flow rate of 35 sccm. Post annealing heat treatment was done on the films at 450 °C in air, argon and nitrogen atmosphere respectively, in an attempt to tune the structural, optical and electrical properties of TiO_2:Ge films. The effect of annealing ambient on structural, optical and electrical properties for the films was later analyzed. The films annealed in nitrogen and argon appeared dark brown indicating an increase in oxygen vacancies while those annealed in air were utterly transparent. The X-ray diffraction patterns of both pure TiO_2 and TiO_2:Ge films showed that the films were composed of anatase and rutile phases irrespective of the annealing atmosphere with crystallite sizes ranging between 19-21 nm. Scanning Electron Microscope images of the films showed crack- free structures that had good adherence to the substrates, with the films annealed in nitrogen showing larger crystals compared to those annealed in air and argon. This is an indication of improved crystallinity. It was observed that, increase in Ge content in TiO_2 matrix decreased both the optical properties and electrical properties. TiO_2:Ge ratio of 85:15 recorded the lowest transmittance average of 70% in wavelengths 400-700 nm. The bandgap decreased from 3.64 eV to 3.57 eV while the electrical resistivity decreased from 11×10^{-2} $\Omega-cm$ to 2.24×10^{-2} $\Omega-cm$. On the other hand, TiO_2:Ge thin films annealed in nitrogen recorded the best optical and electrical properties with the bandgap and resistivity averaging about 3.55 eV and 5.23×10^{-2} $\Omega-cm$ respectively. Generally, good films were obtained at optimal condition of 10% Ge concentration in TiO_2 matrix and annealed in N_2. It was therefore recommended that TiO_2:Ge thin films with 10% Ge concentration and annealed in nitrogen atmosphere could be considered as a potential photoanode in Dye Sensitized Solar Cells applications.

Table of Contents

DECLARATION ii

DEDICATION iii

ACKNOWLEDGEMENT iv

Abstract v

List of Figures ix

List of Tables xii

List of Abbreviation xiii

List of Symbols xiv

CHAPTER ONE 1

INTRODUCTION 1

1.1 Background 1

1.2 Statement of the problem 4

1.3 Objectives 5

1.3.1 Main Objective 5

1.3.2 Specific objectives 5

1.4 Significance and Justification of the Study 5

CHAPTER TWO 7

LITERATURE REVIEW 7

2.1 Introduction 7

2.2 Deposition Techniques for TiO_2 Thin Films 7

2.3 Improvement of TiO_2 Properties for Photovoltaic and Photocatalytic Application 8

2.3.1 Dye sensitization 8

2.3.2 Doping of TiO_2 9

2.3.3 Effects of Optimization of Deposition Parameters on Properties of TiO_2 10

2.3.4 Annealing TiO_2 in different Ambient/Atmospheres 11

2.4 Germanium 13

2.5 Titanium dioxide: Germanium (TiO_2:Ge) nanocomposite 13

CHAPTER THREE 16

THEORETICAL BACKGROUND 16

3.1 Introduction 16

3.2 Titanium Dioxide Semiconductor 16

3.3 Optical Characterization 17
3.3.1 Transmittance and Reflectance 17
3.3.2 Absorption 19
3.3.3 The Energy Bandgap 19
3.4 SCOUT Software 20
3.4.1 Drude Model 21
3.4.2 OJL Model 21
3.4.3 KIM Oscillator Model 22
3.5 Deposition Techniques of Thin Films 23
3.5.1 Sputtering Technique 23
3.5.2 Reactive DC Magnetron Sputtering 24
3.5.3 RF Magnetron Sputtering Technique 24
3.6 Thin Film Formation Process 25
3.6.1 Film Growth Models 25
CHAPTER FOUR 27
MATERIAL AND METHODS 27
4.1 Introduction 27
4.2 Acquisition of Materials and Purity Levels 27
4.3 Substrate Cleaning 27
4.4 Deposition of TiO_2:Ge Thin Films 28
4.5 Optimization of Argon Flow Rate and Sputtering Power 30
4.6 Optical Characterization 31
4.7 Electrical Characterization 31
4.8 Morphological and Structural Characterization 33
4.9 Raman Spectroscopy 33
4.10 Elemental Analysis-EDXRF 34
CHAPTER FIVE 36
RESULTS AND DISCUSSION 36
5.1 Introduction 36
5.2 Raman Spectroscopy 36
5.3 Energy Dispersive X-Ray Fluorescence for TiO_2:Ge Thin films 37
5.4 Effect of Annealing and Sputtering Power on Optical Properties for TiO_2:Ge Thin Films 38

5.4.1 Transmittance 39
5.4.2 Absorbance 43
5.4.3 Optical Energy Bandgap 44
5.4.4 Refractive Index (n_f) 47
5.4.5 Extinction Coefficient (k_λ) 50
5.5 Influence of Sputtering Power on Electrical Resistivity for TiO_2:Ge Thin Films 52
5.6 Influence of Argon Flow Rate on Optical Properties for TiO_2:Ge Thin Films 54
5.6.1 Transmittance 54
5.6.2 Energy Bandgap 57
5.6.3 Refractive Index 60
5.7 Effect of Argon Flow Rate on Electrical Resistivity for TiO_2: Ge Thin Films 61
5.8 Elemental Analysis for Pure TiO_2 and TiO_2: Ge Thin Films 64
5.8.1 Energy Dispersive X-ray Fluorescence (EDXRF) for Pure TiO_2 and TiO_2: Ge Thin Films 64
5.9 Structural Analysis of TiO_2:Ge Thin Films 65
5.10 Morphological Analysis for TiO_2: Ge Thin Films Annealed in Different Atmospheres 70
5.11 Effect of Ge Concentration and Annealing Ambient on Optical Properties for TiO_2: Ge thin Films 72
5.11.1 Transmittance 72
5.11.2 Energy Bandgap 76
5.11.3 Refractive Index 81
5.12 Effect of Ge Concentration in TiO_2 and Annealing Atmosphere on Electrical Resistivity of TiO_2: Ge Thin Films 82
CHAPTER SIX 85
CONCLUSION AND RECOMMENDATION 85
6.1 Conclusion 85
6.2 Recommendation for Further work 86
References 87

List of Figures

Figure 3. 1 :Crystalline Phases of Titanium dioxide 17
Figure 3. 2: Transmission and reflection of a unidirectional beam of light 18
Figure 3. 3: Direct and Indirect Bandgaps 20
Figure 3. 4: The fit parameters of OJL interband transition 22
Figure 3. 5: Film formation process 25
Figure 3. 6: The three growth modes of thin films 26

Figure 4. 1: The standard substrate cleaning procedure 28

Figure 4. 2: Auto 306 sputtering chamber during deposition 29
Figure 4. 3: The tube furnace set up for annealing samples 31
Figure 4. 4: The four point probe system 32
Figure 4. 5: X-ray Fluorescent set up 35

Figure 5. 1: Raman Spectra for annealed TiO_2:Ge (95:5) thin films deposited at various sputtering powers 37

Figure 5. 2: EDXRF energy spectrum of TiO_2:Ge (95:5) thin films 38
Figure 5. 3:Optical transmittance for as-deposited (a) and annealed (b) TiO_2:Ge (95:5) thin films deposited at different sputtering powers 40
Figure 5. 4: SCOUT fitting for transmittance spectra for annealed TiO_2:Ge (95:5) thin films deposited with sputtering power of 150W (44.3 nm): Inset is SCOUT fitting transmittance graph for annealed TiO_2:Ge films deposited at 75W (10.8 nm) 41
Figure 5. 5: Variation of film thickness (a) and sputtering yield (b) with of sputtering power for TiO_2:Ge (95:5) films 43
Figure 5. 6: Variation of absorbance with sputtering power for TiO_2:Ge (95:5) films 44
Figure 5. 7: The energy bandgaps for the annealed TiO_2:Ge (95:5) films deposited at 75W and 220W (a), 120W (b) and 150W (c) 45
Figure 5. 8: Energy bandgap versus sputtering power 47

Figure 5. 9: Refractive index versus wavelength for TiO_2:Ge (95:5) films deposited at various sputtering powers 48
Figure 5. 10: Refractive index versus wavelength for as-deposited and annealed TiO_2:Ge (95:5) films deposited at 150W 49
Figure 5. 11: Extinction Coefficient versus wavelength for annealed TiO_2:Ge (95:5) films deposited at various sputtering powers 50
Figure 5. 12: Extinction coefficient against wavelength for as-deposited and annealed TiO_2:Ge (95:5) film deposited at 150W 51
Figure 5. 13: Resistivity for the as-deposited and annealed TiO_2:Ge (95:5) films deposited at different sputtering powers 53
Figure 5. 14: Transmittance spectra of TiO_2:Ge (95:5) films with variation in argon flow rate for as-deposited (a) and annealed samples (b) 55
Figure 5. 15: Variation of thickness (a) and sputtering yield (b) with of argon flow rates (30-60 sccm) for TiO_2:Ge (95:5) thin film 57
Figure 5. 16: The energy bandgap of as-deposited TiO_2:Ge (95:5) thin films deposited at 30sccm (a), 35 sccm (b), 40 sccm (c) and 60 sccm(d). 58
Figure 5. 17: Energy bandgap variation for annealed TiO_2:Ge (95:5) films deposited at 30 sccm (a), 35 sccm (b), 40 sccm (c), and 60 sccm (d). 59
Figure 5. 18: Refractive index versus wavelength for TiO_2:Ge (95:5) thin films at different argon flow rates 61
Figure 5. 19: Variation of resistivity for as-deposited and annealed TiO_2:Ge (95:5) thin films with argon flow rate 63
Figure 5. 20: EDXRF spectra for pure TiO_2 (a) and TiO_2:Ge (95:5) (b) thin films. The other nanocomposites films with Ge have a similar spectrum an in (b) above 65
Figure 5. 21: XRD patterns for pure TiO_2 and TiO_2:Ge films annealed in (a) N_2, (b) Ar and (c) Air 67
Figure 5. 22: Determination of FWHM for TiO_2:Ge (90:10) thin films using 38^0 (004) peak 69
Figure 5. 23: The SEM micrographs images for Pure TiO_2 (a_1, b_1 and c_1) and TiO_2:Ge (85:15) a_2,b_2 and c_2 annealed in Nitrogen (a_1 and a_2), Argon (b_1 and b_2) and Air ($c_1$and c_2) 71

Figure 5. 24: Optical transmittance for TiO_2:Ge thin films for (a) as-prepared (b) annealed in Ar, (c) annealed N_2 and (d) annealed in Air with different concentration of the Ge (from 0-15 %) ... 73
Figure 5. 25: Optical transmittance for pure TiO_2 (a), TiO_2:Ge (95:5) (b), TiO_2:Ge (90:10) (c), and TiO_2:Ge (85:15) (d) films annealed in different atmosphere (Air, Ar, and N_2) at 450 ^{0}C ... 75
Figure 5. 26: Bandgap variation with Ge Concentration for TiO_2:Ge 85:15 and 90:10 (a), 95:5 (b) and pure TiO (c) annealed in Argon ... 77
Figure 5. 27: Bandgap variation with Ge concentration for TiO_2:Ge films 85:15 (a), 90:10 (b), 95:5 (c) and pure TiO_2 (d) annealed in Air ... 78
Figure 5. 28: Bandgap variation with Ge concentration for TiO_2:Ge films 85:15 (a), 90:10 (b), 95:5 (c) and pure TiO_2 (d) annealed in Nitrogen ... 79
Figure 5. 29: Energy bandgap versus different ratios of TiO_2:Ge thin films annealed in N_2, Ar and Air ... 81
Figure 5. 30: Dependence of Refractive Index on annealing atmosphere of pure TiO_2 thin films ... 82
Figure 5. 31: Resistivity versus Ge concentration in TiO_2 for different annealing atmosphere .. 84

List of Tables

Table 4. 1: Deposition parameters for TiO_2:Ge thin films 30

Table 5. 1: Thickness and yield rate for as-deposited and annealed TiO_2:Ge films deposited at different powers 42

Table 5. 2: Resistivity and conductivity for as-deposited and annealed TiO_2:Ge thin films deposited at different powers. 52

Table 5. 3: Thickness and sputtering yield variation with argon flow rate for TiO_2:Ge films..... 56

Table 5. 4: The energy bandgap for the as-deposited and annealed TiO_2:Ge films deposited at various argon flow rates (30 sccm-60 sccm) 60

Table 5. 5: Resistivity and conductivity for as-deposited and annealed TiO_2:Ge films deposited at various argon flow rate 62

Table 5. 6: Different percentages of TiO_2:Ge films annealed in air, Ar and N_2 and their contents in PPM. 64

Table 5. 7 : Crystallite sizes for the 38° (004) peak of TiO_2:Ge films using Scherrer's formula 69

Table 5. 8: The dislocation defect density for TiO_2:Ge films as 70

Table 5. 9: Particle size of pure TiO_2 and TiO_2:Ge (85:15) annealed in N_2, Ar and air.............. 72

Table 5. 10 : Variation of thickness with Ge concentration in TiO_2:Ge films annealed in air, Ar, and N_2 gases. 76

Table 5. 11 : Variation of the bandgap values with Ge concentration for films annealed in air, nitrogen, and argon atmosphere 80

Table 5. 12: Resistivity variation for TiO_2:Ge annealed in a different atmosphere 83

List of Abbreviation

CB	Conduction Band
CVD	Chemical Vapour Deposition
DSSC	Dye sensitized solar cell
DC	Direct Current
EDXRF	Energy Dispersive X-Ray Fluorescence
eV	Electron Volts
FTO	Fluorine doped Tin Oxide
FWHM	Full Width at Half Maximum
IR	Infra-red
OJL	O'Leary-Johnson
PLD	Pulse Laser Deposition
PPM	Parts Per Million
PVD	Physical Vapour Deposition
PV	Photovoltaic
RF	Radio Frequency
SEM	Scanning Electron Microscope
Toe	Tons of oil equivalent
TiO_2	Titanium dioxide
UV	Ultra-Violet
VB	Valence Band
XRD	X-Ray Diffraction

List of Symbols

α	Absorption coefficient
Ar	Argon
p_f	Average film density
p_m	Bulk density
I	Current
q	Charge
D	Crystallite size
Ω_τ	Damping constant
m	Effective mass carrier
E_g	Energy band gap
E	Electric field
μ	Electron mobility
k_λ	Extinction coefficient
d	Film Thickness
β	Full Width at Half Maximum
F	Force
B	Magnetic field
n	Refractive index
$n_{TiO_2:Ge}$	Refractive index of TiO_2:Ge films
n_{TiO_2}	Refractive index of dense TiO_2 anatase Phase
Ω_{TO}	Resonance position
Ω_p	Oscillator Strength

O^{2-}	Oxygen vacancy
ε_0	Permittivity of free space
$h \nu$	Photon energy
ρ	Resistivity
K	Shape factor
θ	Theater
λ	Wavelength

CHAPTER ONE

INTRODUCTION

1.1 Background

Thin films were first made by Busen and grove in 1852 using chemical reactions (Shinen *et al.*, 2018). In 1857, Faraday was able to obtain a thin film by thermal evaporation (Eckortova, 1977). Recently, the theoretical and experimental study of thin films has generated a lot of scientific and technological interest because of the unique electronic and optical properties and exhibition of new quantum phenomenon. The knowledge gained from research done in the area of thin films has been applied successfully for technological development in many countries. Thin films are widely used in our current technology and their applications are likely to broaden in future. Through this advancement in technology, there has been tremendous change in a lot of sectors such as in communication, transportation and industrialization just to mention a few (Tiginyanu *et al.*, 2016).

Optoelectronics, which is the study of the interaction of light with electronic devices, is one among the technological advancements that have been widely studied. Optoelectronics device advancement has led to tremendous development activities accompanied by dynamism. Some of the optoelectronic devices that have a wide application in the current day to day life include; Light Emitting Diodes (LEDs), solar cells, optical fibers, photodiodes and laser diodes which have brought a lot of advancement in the storage and production of data, fiber optic communication, laser pointers, CD/DVD disc reading and laser printing and scanning (Brennan, 1999).

Solar cell is one of the optoelectronic devices that has been widely studied through thin film technology. Thin films solar cells (TFSCs) are the second-generation type of solar cells that have very thin layer of thickness (few nanometers). These solar cells are relatively economical compared to the conventional silicon technology. Examples of second generation TFSCs include cadmium Telluride (CdTe), amorphous silicon (a-Si) and Copper Indium Gallium Deselenide (CIGS) (Kosyachenko, 2011). Other thin film technologies that have recently emerged are the third-generation cells including perovskite, DSSCs, nanocrystal solar cells among others (Green, 2002). Research into new materials in form of thin films has been intensified in order to fabricate

simple and affordable solar cells that have the capability to generate electricity for use with improved efficiency.

Metal oxides such as TiO_2, CuO, and ZnO reveal good mechanical and chemical properties and hardly show deterioration (Youssef *et al.*, 2018). Being one of the essential wide bandgap semiconductors, TiO_2 has been subjected to extensive research for decades. This is because of its attractive properties and its wide application in optoelectronic (Usha *et al.*, 2014). Intensive and extensive research has been done on TiO_2 semiconductor but still new approaches are coming up to improve its properties and synthesize quality films for better performance.

Titanium dioxide semiconductor has attractive physical, optical, chemical, and electronic properties including; high photocatalytic activity, excellent transmission in the visible light, high dielectric constant, high refractive index, non toxicity, low cost and good thermal and chemical stability (DeLoach *et al.*, 1999). These characteristics majorly depend on the crystallinity and microstructure of TiO_2. Titanium dioxide is characterized as an n-type semiconductor because of its oxygen deficiency in its structure.

Titanium dioxide thin films have been fabricated for several applications. It has been used extensively as a photoelectrode in DSSC applications (Kang *et al.*, 2009; Tan and Wu, 2006; Okuya *et al.*, 2002). TiO_2 has also be applied as an antireflection coating, as a UV filter in cosmetics, as a photocatalyst, gas sensor as well as anti-corrosion protective coating. It can be used in ceramics, in transistors, as an a node material for Li-ion batteries and as a biocompatible component of bone implants among others (Carmichael *et al.*, 2013; Carp *et al.*, 2004; Kirner *et al.*, 1990)

One major limitation of titanium dioxide semiconductor in its photovoltaic application is the recombination of photogenerated charge carriers (Devi and Kumar, 2011). This may be associated with the impurities, defects or surface imperfections of the crystal structure. Generally, recombination reduces the efficiency of the solar cell fabricated (Choi *et al.*, 1994a). In addition, being a wide bandgap semiconductor, TiO_2 can only be activated upon irradiation with rays from the UV region ($\leq$ 380 nm). Ultraviolet light accounts for $<$ 10% of the solar spectrum. This limits

the practical efficiency for solar application and therefore need for broadening the spectral response to the visible range.

Research into various ways of improving the photovoltaic performance of TiO_2 is underway. Among the various strategies adopted include increasing the porosity in the TiO_2 structure. This reduces the rate of recombination at the grain boundaries. The incorporation of other additional component such as metals and metal ions in titanium dioxide structure has proved to be among the best techniques used to control its properties for various applications. There are two ways of doping elements in TiO_2, substitution and interstitial doping (Aourag *et al.*, 1993). In interstitial doping, the dopant fits in the empty space between the TiO_2 lattices while in substitution doping, either oxygen or titanium are replaced within the lattice (Lynch *et al.*, 2015). Dopants increase TiO_2 conductivity by providing free carriers hence reducing the resistivity. In addition, dopants also introduce defects levels in the crystal symmetry which increases the absorption of visible light. Transition metals have proved to enhance the properties of TiO_2 semiconductor. However, these metals still act as sites of recombination of the photogenerated electron-hole pair, results in thermal instability in TiO_2 structure and cause photocorrosion of the material. This lowers the general quantum performance of the fabricated device (Zeng *et al.*, 2007).

Apart from doping, other approaches to introduce defects in the TiO_2 structure are mediation through incorporation of Ti^{3+} and oxygen vacancies by reduction (Zheng *et al.*, 2013). Most researchers employ the use of hydrogen reducing environment and annealing films at elevated temperatures to produce defective TiO_2 structure (Naldoni *et al.*, 2012; Chen *et al.*, 2011). However, defective TiO_2 nanoparticles can also be achieved by annealing amorphous TiO_2 nanoparticles in an oxygen deficient environment such as in a vacuum, argon or nitrogen environment (Tian *et al.*, 2015).

Recent research demonstrated that formation of TiO_2 composites nanostructures could also improve the properties of the semiconductor. Metals and non- metals nanoparticles are often introduced in TiO_2 matrix to increase the separation of photo-induced charge carriers during photocatalytic processes in areas of photocatalysis and solar energy conversion. Although many elements have been proposed for this purpose, carbon and its allotropes remain to be the primary choice due to their large surface area which yield an increase in adsorbed pollutants and also

exhibit a large electron storage capacity which may accept electrons excited by photons thus retarding the recombination process (Woan *et al.*, 2009). So far, composite film of graphine/TiO_2 has been used as a photoanode in the fabrication of DSSC and yielded a solar cell with improved efficiency (Tsai *et al.*, 2011). Other composites such as TiO_2/carbon nanotubes TiO_2/mesoporous carbon have produced solar cells with improved efficiencies (Yin *et al.*, 2013; Jang *et al.*, 2004).

Germanium element, being among the carbon family, has also shown great potential when used as a composite with TiO_2 in fabrication of DSSC. Chatterjee (2008a), studied TiO_2:Ge nanocomposite as a photovoltaic material. From his findings, it was suggested that TiO_2:Ge composite is a promising material for fabrication of DSSC. Titanium: Germaniun (TiO_2:Ge) composite has not been widely studied and therefore in this work, TiO_2:Ge thin films were deposited using rf magnetron sputtering and thereafter, the amorphous TiO_2:Ge thin films were annealed in nitrogen, argon and air atmospheres to tailor their properties. The structural, electrical and optical properties of different ratios of TiO_2:Ge thin films annealed in different atmospheres were then investigated under optimum sputtering power and argon flow rate.

1.2 Statement of the problem

Titanium dioxide semiconductor has been applied in many areas including optoelectronics. Despite its potential application in photovoltaic, the fast recombination of the photogenerated electron-hole pair both on the surface and inside its lattice reduces its practical use. In addition, being a wide bandgap semiconductor, TiO_2 can only be activated upon irradiation with rays from UV region. Ultra-violet light accounts for less than 10% of the solar spectrum and therefore, this limits its practical efficiency for solar application and hence the need to broaden the spectral response to the visible region. Doping TiO_2 with other elements have proved to be effective in countering the two shortcomings mentioned above, but still some dopants especially the transition metals act as sites of recombination of the photogenerated charge carriers, some cause thermal instability in the TiO_2 structure and others results in photocorrosion of the material. Formations of TiO_2 composites as well as annealing the films in oxygen deficient environment are among new approaches that are being used to improve the properties of TiO_2 semiconductor. Not much attention has been given to Ge semiconductor, as a composite of TiO_2 and therefore, there is need to study TiO_2:Ge composite and explore its properties. Additionally, the potential of annealing

these films in different atmospheres in order to tune their properties further has not been exploited. This work, therefore, focuses on the electrical, structural and optical properties of rf magnetron sputtered TiO_2:Ge thin films annealed in air, argon and nitrogen for photovoltaic application.

1.3 Objectives

1.3.1 Main Objective

This study aims at investigating the effect of annealing ambient on the structural, optical and electrical properties of TiO_2:Ge thin films for photovoltaic application.

1.3.2 Specific objectives

i. To evaluate the influence of annealing ambient on structural and morphological properties of TiO_2:Ge thin films.
ii. To study the effect of annealing atmospheres on the optical and electrical and properties of TiO_2:Ge thin films.
iii. To evaluate the effect of Ge concentration on structural, optical and electrical properties of TiO_2:Ge thin films.

1.4 Significance and Justification of the Study

Titanium dioxide semiconductor and its attractive characteristics have been the focus of many studies, due to its wide applications in photocatalytic and photovoltaic devices. Despite its potential application, the fast recombination of the photo-induced charge carriers on the surface and inside its lattice limits its practical use. Introducing germanium nanodots in TiO_2 matrix could result in an attractive semiconductor with improved properties that can be applied as an antireflection coating in devices like LED, smart windows and also as a photoanode layer in DSSC. Germanium exhibits a good electron transfer due to its narrow bandgap and this widens its use in solar cells and in other optoelectronic devices. Also, germanium has a remarkable absorption in the infrared region and also has a low sintering temperature which increases the inter-particle contact leading to improved electron transfer. However, germanium as the material has not been widely exploited and little has been reported about it. Additionally, rf magnetron sputtering was

the most preferred method of depositing TiO_2:Ge thin films because of its ability to prevent charge from building up on the target and also its ability to yield high deposition at a relatively low pressure.

This study therefore provides more information on the properties of TiO_2:Ge thin films annealed in air, argon and nitrogen atmospheres. Radio frequency magnetron sputtering technique was used in the deposition of the films and was tailored to obtain the desired optical, structural and electrical properties of the films for photovoltaic application.

CHAPTER TWO

LITERATURE REVIEW

2.1 Introduction

This section focuses on work that has been done to enhance the structural, optical and electrical properties of TiO_2 semiconductor. The deposition methods used to deposit TiO_2 thin films for different applications have also been discussed. Different ways of tailoring the properties of TiO_2 nanoparticles such as doping, dye sensitization, variation of deposition parameters and the effect of annealing TiO_2 in different atmospheres on the properties of TiO_2 have been highlighted. Germanium as an element and TiO_2:Ge nanocomposite has also been discussed.

2.2 Deposition Techniques for TiO_2 Thin Films

Several deposition methods have been used to deposit TiO_2 films for various applications. These include: Pulsed laser deposition (Suda *et al.*, 2004), sol-gel method (Jagadale *et al.*, 2008; Zaleska, 2008), hydrothermal followed by screen printing (Zhu *et al.*, 2010), sputtering (Dholam *et al.*, 2009; Waita *et al.*, 2007; Zhang *et al.*, 2007; Lindgren *et al.*, 2003), chemical vapor deposition (Sarantopoulos *et al.*, 2009; Randeniya *et al.*, 2007) among others. One of the most widely used technique for preparing TiO_2 is sputtering mainly because:(1) It allows deposition of both insulating layer and metallic layer, (2) It's possible to get large surface films, (3) It allows for both quantitative and qualitative control of thin film deposition (Rossnagel *et al.*, 1991), (4) The process can be performed under lower temperature and furthermore, the method is considered to be clean, environmental friendly since the process is carried out in a closed system (Navinšek *et al.*, 1999).

Reactive sputtering has been widely used in deposition of TiO_2 (Yamada *et al.*, 2007; Zhang *et al.*, 2007; Carneiro *et al.*, 2005). Yamada *et al.*, (2007) fabricated Nb: TiO_2 thin films by reactive sputtering with an aim of having a reduced resistivity. According to their results, annealing the film in hydrogen at 600 °C resulted to a crystalline anatase phase of TiO_2. Further, resistivity of the order 10^{-4} Ω cm and transmittance of 75% in the visible range were reported for the annealed films. Yamada *et al.*, (2007) concluded that sputtering was a promising method for obtaining large area Nb doped TiO_2 thin films.

Lindgren *et al.*, (2003) used reactive sputtering method to investigate effects of doping TiO_2 with nitrogen in order to broaden its spectral response. Structural characteristics of the deposited films showed that as the content of the dopant, nitrogen increased to 1.2%, anatase phase began to evolve and became distinct when nitrogen content grew to 2.5%. The surface roughness value for the undoped titanium dioxide films was 60 nm while for the nitrogen doped TiO_2 films were 30 nm. This was associated to the diminishing grain size which resulted to a compact structure. Nitrogen doped titanium dioxide films indicated an excellent spectral response in the wavelength between 400-535 nm which is within visible region. In this study, it was observed that there was an optimum amount of the doping nitrogen for the best and highest response. Wafula *et al.*, (2008) confirmed similar results.

Oblique physical vapour deposition of TiO_2 has been reported to increase the rate of its light absorption and produce films with columnar structure resulting in a more porous film with large surface area (Waita *et al.*, 2007). Waita *et al.*, (2007) studied the performance of DSSCs synthesized from obliquely sputtered TiO_2 films and observed that the porosity of the deposited films increased with deposition angle. The rough surfaces of the films increased the dye adsorption thereby trapping more light compared to smooth surface. The highest solar cell efficiency achieved was 3.3% at a deposition angle of 60^{0}. The main cause attributed to the low conversion efficiency was the high rate of recombination of photogenererated charge carriers in TiO_2 lattice.

2.3 Improvement of TiO_2 Properties for Photovoltaic and Photocatalytic Application

Titanium dioxide nanoparticles have been customized by different methods, including; size optimization, surface modification, annealing in different atmospheres, dye sensitization, fabrication of composites with other material, metal and non metal doping among others as discussed below.

2.3.1 Dye sensitization

Titanium dioxide has been sensitized using organic dyes (methyl orange, methylene blue, rhodamine B etc.) in order to extend its photon absorption towards visible light (Diaz-Angulo *et al.*, 2019). Dye sensitization has been the most successful way of improving light absorption of TiO_2 nanoparticles and achieving useful efficiencies. However, the instability of the organic

complex in the dye together with charge transport still poses a major challenge (Chatterjee *et al.*, 2006). This calls for other ways of optimizing the properties of TiO_2.

2.3.2 Doping of TiO_2

The incorporation or substitution of foreign atoms in the structure of TiO_2 has proved to enhance its properties. Studies show that doping titanium dioxide with various elements have led to changes in certain properties like increment in porosity and surface area in the particle morphology (Stengl and Bakardjieva, 2010), change in phase composition and structural defects in the crystal lattice (Stengl *et al.*, 2011; Štengl *et al.*, 2010) . Doping of TiO_2 in order to broaden its spectral response of absorptions is important for photoelectrochemical applications. Nah *et al.*, (2010) reported on improved visible light absorption when titanium dioxide was doped with nitrogen. However, there was a strong decrease in the overall photoelectrochemical conversion efficiency. Similar results were confirmed by Mohamed and Rohani, (2011). This was due to the high rate of recombination of the photogenerated electron hole pair (Rani *et al.*, 2010).

Introduction of the metal ions in titanium dioxide semiconductor inhibit the rate of electron-hole recombination by trapping electrons. However, studies show that not all the metal ions doped with TiO_2 improve its photocatalytic performance. Choi *et al.*, (1994b) found that doping TiO_2 with $Co^{3+}$and Al^{3+} decreases the photoactivity performance of TiO_2 while doping with Fe^{3+}, Ru^{3+}, $V^{4+}$and Re^{5+} improves the photocatalytic activity. Studies also show that Cr^{3+} reduces the photocatalytic performance of TiO_2 (Al-Sayyed *et al.*, 1991). In addition, the photocatalytic performance of doped TiO_2 semiconductor strongly depends on the dopant content. Investigations show that the photo-activity of doped TiO_2 increases up to a certain concentration of the dopant and above which, it reduces. Zhou *et al.*, (2006) reported on the effect of iron dopant concentration on the photocatalytic activity of TiO_2 powder synthesized by ultrasonic technique. It was noted that at 25% of the iron dopant concentration, there was maximum photocatalytic performance of the prepared films. Further increase of Fe-doping concentration led to a reduction of the photoactivity of the prepared samples. This is because, excess Fe^{3+} ions behave as electron-hole recombination sites resulting in a decreased photocatalytic activity (Zhang *et al.*, 1998; Choi *et al.*, 1994c). Similar results were confirmed by Wang and Lewis, (2005). Other non-metals dopants

such as sulphur, phosphorous, fluorine, and carbon have also shown positive results in the photoresponse of TiO_2 in visible range (Irie *et al.*, 2003)

2.3.3 Effects of Optimization of Deposition Parameters on Properties of TiO_2

A lot of studies have been done to understand how deposition parameters affect the properties of magnetron sputtered TiO_2 thin films. For example, Jeyachandran *et al.*, (2006) studied the influence of sputtering pressure (1.1-3.3 Pa) , base vacuum ($4 \times 10^{-4} – 1.3 \times 10^{-4}$ pa) and cathode power (75-150 W) on properties of TiO_2 films deposited by dc magnetron sputtering. From their studies, it was reported that the morphological properties of the TiO_2 films were least influenced by the variation of preparation conditions. However, the electrical and structural properties of the films were affected by the variation of deposition parameters. Jeyachandran *et al.*, (2007) investigated the influence of thickness of the film on the properties of dc sputtered TiO_2 thin films. It was noted that the film with a lower thickness was amorphous and the crystallinity improved with increase in thickness. Muslim *et al.*, (2015) studied the influence sputtering power (75 W,120 W, 150 W) on optical, electrical and structural properties of rf magnetron sputtered TiO_2 and reported a decrease in the electrical resistivity of the deposited films with increase in sputtering power. This was attributed to the increase in atomic mobility as described by Boccuzzi *et al.*, (2001). It was also noted that crystallinity, surface roughness and the film grain size increased as sputtering power increased while optical transmittance decreased. Other researchers who studied the influence of power on TiO_2 films include; Luo *et al.*, (2015) and Pansila *et al.*, (2012) who confirmed that the crystalline structure of TiO_2 thin films strongly depended on the sputtering power. Higher sputtering power facilitates growth of rutile structure with improved photocatalysis. Einollahzadeh-Samadi and Dariani, (2013) also reported on the influence of temperature and deposition rate on the optical and morphological properties of titanium films deposited by dc sputtering. The studies done above show that variation of deposition parameters had a significant influence on the properties of TiO_2 and that only a few researchers have reported on rf magnetron sputtering technique compared to dc magnetron sputtering.

Studies have been done to investigate how the argon flow rate affects the properties of TiO_2. Bhardwaj *et al.*, (2018) reported on how variation of argon flow rate (20-40 sccm) affects the optical and structural properties of TiO_2 films. From the investigation, it was reported that all the

films deposited at different flow rates were amorphous in nature with high optical transmission in the range 400 nm-700 nm. The crystallinity of the annealed films increased with flow rate of Ar. Similar results were confirmed by Khojier *et al.*,(2013) whose further results showed that the surface roughness, hardness and crystallite size increased with argon flow rate. This was attributed to energetic ion bombardment experienced at high flow rates. The study on electrical properties showed that the film resistivity increased with argon flow rate. However, not much has been reported on argon flow rate and sputtering power as deposition parameters.

2.3.4 Annealing TiO_2 in different Ambient/Atmospheres

The crystallinity of TiO_2 thin films can be altered by thermal treatment from the as- deposited amorphous films to crystalline anatase and/ or rutile phases (Ghicov *et al.*, 2006). In addition, annealing under different ambient/atmospheres and surface modifications are the main procedures to achieve high performance of films and improve the film conductivity (Wang *et al.*, 2016). Several researchers have annealed TiO_2 films in different atmospheres and the results have been promising. Tavares *et al.*, (2012) studied the effect of annealing Nb- doped TiO_2 thin films in hydrogen atmosphere on its structural and electrical properties. It was observed that the electrical conductivity increased with more than two orders to 330 $\Omega^{-1}cm^{-1}$ with a small resistivity of 3.0×10^{-3} Ω cm. This was because of the creation of O_2 deficiency during thermal annealing in hydrogen which was subsequently ionized to form free electrons resulting in an increased conductivity.

Tighineanu *et al.*, (2014) reported on the influence of annealing conditions on the conductivity of anodic TiO_2 nanotubes. It was observed that the samples annealed in N_2 and Ar had a lower resistance regardless of the annealing temperature. This was attributed to the of loss of O_2 and formation of Ti^{3+} states in O_2 depleted atmosphere (self doping) (Chen *et al.*, 2011). It was also noted that the phase transition from amorphous to anatase is faster when samples are annealed in O_2 and air (250 °C) compared to when annealed in Ar and N_2 gases and subjected to the same thermal conditions. Samples annealed at higher temperature showed a higher resistance due to several factors including; transition from anatase to rutile phase (Albu *et al.*, 2008), formation of cracks in the film (Albu *et al.*, 2010) and thermal growth of thicker rutile under layer by oxidation of Ti substrate.

Different annealing gases has shown great influence on electrical and structural properties of TiO_2 thin films (Rahim *et al.*, 2017a). Rahim *et al.*, (2017a) observed that, the films annealed in air, Ar and N_2 at 500 °C showed anatase phase with N_2 and air ambient showing a great crystallinity. TiO_2 films annealed in air exhibited a uniform and homogeneous structure compared to the films annealed in Ar and N_2. A lower resistivity (3.12×10^{-4} Ω-cm) was found for TiO_2 films annealed in air. The results contradicted with the findings of Liu *et al.*, (2008b) which showed that the electrical conductivity of TiO_2 nanotube arrays annealed in N_2 was higher than those calcined in Ar and air. According to the latter, the formation of O_2 vacancies was ascribed to explain the improvement in the conductivity of TiO_2 nanotube arrays.

Anwar *et al.*, (2016) investigated on the effect of annealing atmospheres (air, Ar, N_2 and H_2) on crystallite sizes and specific capacity of TiO_2 nanotubes arrays (TNAs) deposited by electrochemical anodization. It was noted that annealing in different atmospheres induced variation in crystallite size. The samples annealed in oxygen deficient environments such as N_2 and H_2 recorded the smallest crystallite size. However, the highest heat capacity of about 190 $mAhg^{-1}$ was realized by the sample annealed in H_2. The SEM images of TNAs annealed in different atmospheres showed no specific morphological changes and this was consistent with the previously reported literature (Jian *et al.*, 2012; Wang *et al.*, 2011). Structural analysis showed that all the films were composed of pure anatase phase.

Hydrogen gas has been confirmed to be a better reducing gas since the films annealed in it achieve better crystallinity and also contain more oxygen vacancies. Huang and Wong, (2011) studied the properties of titanium thin film annealed under different atmosphere: air, vacuum and H_2. The films annealed in H_2 showed a better crystallinity than those annealed air and vacuum. Structural analysis showed that the presence of oxygen vacancies in titanium lowered the temperature of phase transformation from amorphous to anatase and from anatase to rutile. The films annealed in H_2 gas also exhibited the best photocatalytic performance under UV and visible region. Similar results were obtained by Hyam *et al.*,(2012) in his study on how the annealing environments affect the photocatalytic performance of TiO_2 nanotubes.

In a study by Xiao *et al.*, (2008), titanium nanotubes arrays were annealed in air, argon and nitrogen gases and the effect of different annealing atmospheres on their photoelectrical and

electrochemical properties was studied. It was noted that the electrical conductivity of TiO_2 nanotube arrays annealed in N_2 improved significantly compared to the as-deposited and those annealed in air and Ar. In addition, photocurrent response in TiO_2 nanotube arrays annealed in N_2 was enhanced to about 84 $mAcm^{-2}$. Formation of T^{3+} and increased oxygen vacancies were attributed to the improved electrochemical and photoelectric properties of titanium nanotube arrays.

Other researchers who have worked on TiO_2 films annealed in different atmosphere in order to tune its properties include Mazzolini *et al.*, (2015) Sarkar *et al.*, (2012) and Wang *et al.*, (2011) whose studies confirmed that annealing TiO_2 thin films in oxygen deficient atmosphere improved their conductivity, as well as photocatalytic activity of the films.

2.4 Germanium

Germanium was first discovered by a German chemist Clemens Winkler in 1886 in argyrodite mineral (Melcher and Buchholz, 1988). Today, it is extracted from coal and by-products of zinc (Moskalyk, 2004). Germanium has a direct and indirect bandgap of 0.80 and 0.66 eV respectively (Li *et al.*, 2012). Due to its narrow bandgap, Ge absorbs in the infrared region of the solar spectrum and exhibits a good electron transfer. It has been found to be an attractive material for use in optically absorbing and emitting devices. Recently, researchers have fabricated a germanium laser (Liu *et al.*, 2010) and also used germanium as an electro-optic modulator (Liu *et al.*, 2008c). Germanium is also used to make transistors, create alloys, as a phosphor in fluorescent lamps and also as a catalyst to produce plastics (Yellishetty *et al.*, 2017).

2.5 Titanium dioxide: Germanium (TiO_2:Ge) nanocomposite

Germanium ion (Ge^{4+}), has ionic radius of 0.054 nm which is much smaller as compared to titanium, whose ionic radius is 0.0605 nm (Song *et al.*, 2010; Pullar *et al.*, 2009). This means that Ge^{4+} can easily fit in TiO_2 lattice. The incorporation of Germanium in TiO_2 matrix creates an attractive semiconductor with improved properties. The properties of TiO_2:Ge semiconductors are distinct from those of TiO_2. For example, TiO_2 always absorbs in the UV region while TiO_2:Ge absorbs in the visible region. TiO_2:Ge is reported to have a smaller bandgap of 1.86 eV and enhanced transport properties as compared to TiO_2 (Chatterjee and Chatterjee, 2008). The

semiconductor is also stable in air, water and alkalis (Hamad *et al.*, 2005). Introduction of germanium in the TiO_2 matrix has addressed the major challenge of electron-hole recombination resulting to an improved quantum efficiency of the fabricated devices. TiO_2: Ge films have wide applications in photovoltaic, thermo-electric, optoelectronic and also in the degradation of warfare agents (Stengl and Bakardjieva, 2010; Chatterjee, 2008a).

Titanium dioxide: Germanium (TiO_2:Ge) nanocomposite films have been studied on as a good promising material for the next generation thermoelectric, optoelectronic and photovoltaic applications (Chatterjee, 2008b; Chatterjee, 2008a; Chatterjee and Chatterjee, 2008). From the studies, Chatterjee observed that introducing Ge dots in TiO_2 matrix created a supper lattice structure with improved properties. The photoresponse of TiO_2: Ge nanocomposite was observed to rise with increase in Ge concentration up to an optimum value where further increase resulted in a reduction in the photoactivity of the samples. TiO_2:Ge thin films were reported to be photoconductive with a higher conductivity of 1.62×10^{-2} S cm^{-1}. It was also noted that variation of deposition parameters such as sputtering power changed the size, concentration and the morphological phase of the deposited films, which in turn affected the electronic transport of the nanocomposite. This was in agreement with Ahmad *et al.*, (2018) who investigated on the efficiency of solar cells fabricated using TiO_2:Ge as the anode. It was concluded that germanium has the ability to enhance the performance of DSSC.

Titanium: Germanium composite has also been applied in the degradation of toxic substances in several samples. Stengl and Bakardjieva, (2010) evaluated the ability of germanium ion doped TiO_2 in the degradation of venomous agents x, sulphur mustard and soman into non-toxic products. The best degree of degradation was 100% for soman, 99% for venomous agent x and 95% for sulphur was achieved for samples with 2 wt % of Ge. It was therefore concluded that introduction of Ge ions in anatase phase of TiO_2 was efficient in the conversion of toxic to non toxic substances. Stengl and Bakardjieva (2010) study showed that TiO_2:Ge thin films have a wide range of applications and these applications are likely to broaden in future.

Post –deposition heat treatment has shown a strong effect on optical and structural characteristics of TiO_2:Ge films. Khan *et al.*, (2013) studied on how annealing temperature and Ge concentration in TiO_2 affect the properties of nanostructured TiO_2: Ge films. The thickness for TiO_2 was fixed

at 20 nm while that for Ge was varied from 5, 10 and 15 nm. It was observed that the transmittance spectra of the annealed TiO_2: Ge shifted towards the shorter wavelength. This was due to enhanced quantum confinement effect. Absorption spectra showed complete oxidation of Ge layer annealed at 500 °C. There was a reduction in the bandgap for the annealed samples. Rutherford Back Scattering (RBS) study confirmed that annealing of the TiO_2: Ge samples did not destroy the structure layer of TiO_2: Ge. This was attributed to the non wetting property of Ge with TiO_2.

As discussed above, although some work has been done on annealing materials in different ambient, the question is whether a composite would behave similarly when post annealed in different ambient. Besides, would there be a difference if the composite percentage is varied? In the current study, TiO_2: Ge thin films were deposited by rf sputtering method. Prior to final deposition of these films, the sputtering power and argon flow rate was first optimized. The deposited films were then annealed in different atmospheres, that is, air, argon and nitrogen. The optical, structural, and electrical properties of both the as-deposited and the annealed films were investigated using X-ray Diffraction (XRD), SEM, UV-VIS spectrophotometer and the four point probe system respectively.

CHAPTER THREE

THEORETICAL BACKGROUND

3.1 Introduction

The chapter details with the theory on which the current work is based. Working principles of devices, Physics of materials, formulas and calculations as well as vacuum principles have been discussed. SCOUT software models employed during simulation of transmittance data in the current study have also been discussed. The modes of thin film and the process of thin film formation have also been captured.

3.2 Titanium Dioxide Semiconductor

Titanium dioxide semiconductor can be classified in three crystalline phases: Anatase, Rutile, Brookite (Nolan *et al.*, 2009). The three phases can be readily synthesized in the laboratory using both chemical and physical deposition techniques. The anatase phase crystallizes from amorphous solid at temperatures of around 400-500 °C. At high temperatures exceeding 600 °C, the anatase and brookite are irreversibly converted to rutile phase (Campbell *et al.*, 1999). Rutile and anatase phases posses' tetragonal structures but belong to different space groups. Rutile belongs to space group $P4_2/mnm$, density= 4.12 g/cm^3 while anatase belong to space group $I4_1/amd$, density=3.894 g/cm^3. Brookite has got both corners and edges shared resulting in an orthorhombic structure with space group Pbca, density=4.12 g/cm^3 as shown in figure 3.1. The octahedra in anatase are connected by their edges resulting to a (001) plane, in rutile by the vertices forming (110) plane and in brookite by both vertices and edges (Pelaez *et al.*, 2012). Their structures consists of a Ti atom surrounded by six oxygen atoms (TiO_2^{-6}) with a wide indirect bandgap of 3.0, 3.2 and 3.2 eV for rutile, anatase and, brookite respectively (Amtout and Leonelli, 1995).

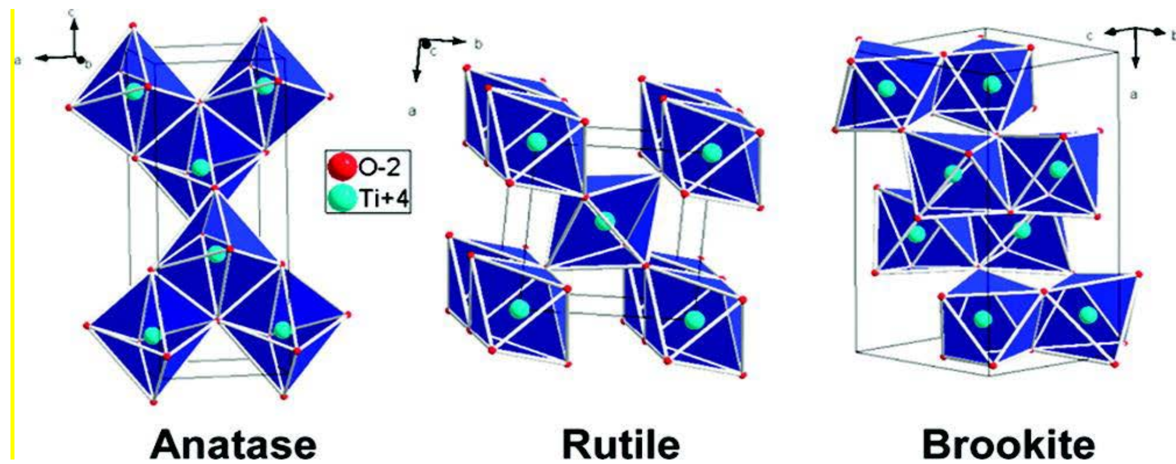

Fig 3. 1 : Crystalline phases of Titanium dioxide (Amtout and Leonelli, 1995)

3.3 Optical Characterization

3.3.1 Transmittance and Reflectance

Transmittance is the relative amount of light that passes through a medium completely whereas reflection is the process whereby the electromagnetic radiations are reverted back at the boundary between two media. Reflection can be categorized into two, which is surface and volume reflection (Went *et al.*, 2008). Volume reflection occurs at the inner part of the medium while surface reflection occurs on the surface of the medium. Transmittance and reflection are usually accompanied by scattering which is the process of rebounding a unidirectional beam in diverse directions. When no diffusion occurs, we have regular transmittance and reflectance that are unidirectional and obey the laws of geometric optics. Usually, the optical properties of materials are not a constant, because they depend on many parameters including the thickness of the film, temperature, angle of incidence, composition of the radiation and many others. Figure 3.2 shows an illustration of how a unidirectional beam of light is transmitted and reflected between the two media.

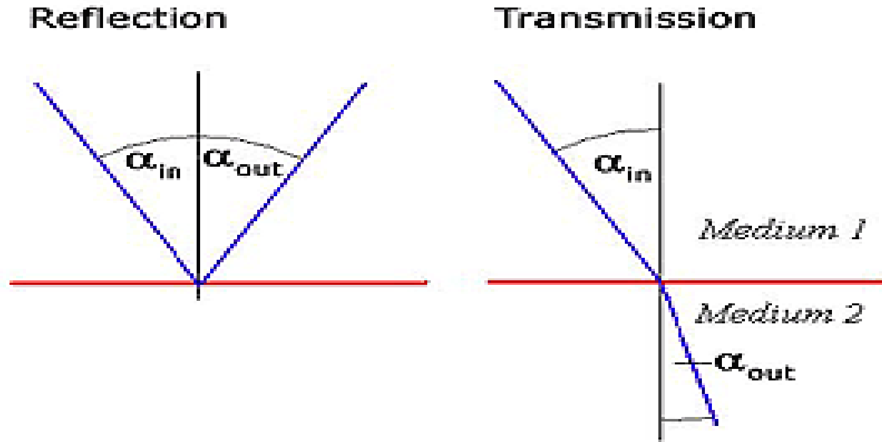

Fig 3. 2: Transmission and reflection of a unidirectional beam of light (Weisstein, 2003).

Transmittance and reflectance are measured using a spectrophotometer at various wavelengths. For thin films transmittance is given by equation 3.1 (Yakuphanoglu *et al.*, 2004).

$$T = (1 - R)^2 e^{-\alpha d} \tag{3.1}$$

Where T is the transmittance, R is the reflectance, α is the absorption coefficient and d is the film thickness.

For shorter wavelength near the bandgap, losses due to scattering are highly experienced and therefore equation 3.2 is preferred (Mardare *et al.*, 2000).

$$\alpha = \frac{1}{d} \ln \frac{1}{T} \tag{3.2}$$

The reflectance R, refractive index n_f, and extinction coefficient k_λ are given by equations 3.3, 3.4 and 3.5 respectively (Aksay and Altıokka, 2007).

$$R = \frac{k^2 + (n-1)^2}{k^2 + (n+1)^2} \tag{3.3}$$

$$n = \frac{1+R}{1-R} + \sqrt{\frac{4R}{(1-R)^2} - k^2} \tag{3.4}$$

$$k = \frac{\alpha\lambda}{4R} \tag{3.5}$$

3.3.2 Absorption

Absorption is the ability of a substance to absorb light of a specified wavelength incident on it and in the process an electron is excited to move from the valence to conduction band. For any material, the band structure can simply be determined by measuring its absorption spectrum. Absorption is usually expressed as a coefficient α and can be described as the rate at which the intensity of light decreases as it passes through a given substance.

3.3.3 The Energy Bandgap

The energy bandgap of a material can be calculated using the following Tauc's method (Dolgonos *et al.*, 2016).

$$\alpha(h\upsilon) = A(h\upsilon - E_g)^n \tag{3.6}$$

$$h\upsilon = \frac{1240}{\lambda}$$

Where, $h\nu$ is the energy of the photon, α is the absorption coefficient, E_g is bandgap, A is a constant which depends on the material used, and n is the transition type. n is 2, $\frac{1}{2}$, 3 and $\frac{2}{3}$ for indirect allowed, direct allowed, indirect forbidden and direct forbidden transitions respectively (Tang *et al.*, 1994). Using a plot of ($(\alpha h\upsilon)^n$ versus $(h\upsilon)$, the extrapolated optical absorption gap gives the approximate energy bandgap of the material.

Semiconductors can have either an indirect or direct bandgap as shown in figure 3.3. In a direct bandgap, the crystal momentum of holes and electrons is similar in both valence and conduction band. In this case a photon is emitted by the electron. In indirect bandgap semiconductors, no photon is emitted since an electron passes through intermediate states to transfer momentum to the crystal. Examples of Indirect bandgap semiconductors are Si, Ge and Ti while the direct bandgap semiconductors are mainly composed of group III-V elements. Figure 3.3 below illustrates the difference between direct and indirect band gaps.

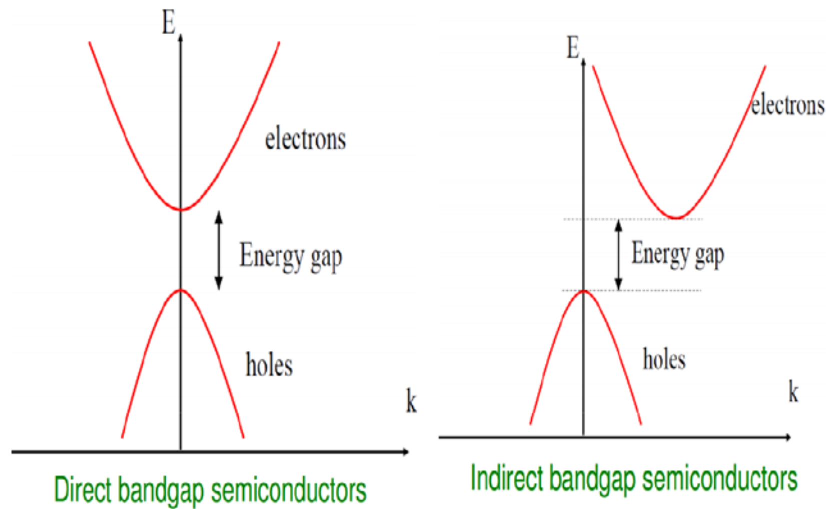

Fig 3. 3: Direct and Indirect Bandgaps (Pankove, 1975)

3.4 SCOUT Software

SCOUT is window NT/2000/XP/vista software which is used to analyze the optical spectra by computer simulation (Theiss, 2012) . It consists of optical constant models that give flexibility when fitting the experimental data. Some of the optical constant models that are used are; dielectric constant, OJL interband transition, Drude model, Kim oscillator, Tauc-Lorentz interband transition model, Brendel model, Campi-Coriasso interband transition and the harmonic oscillator. The first four models mentioned above were employed in the current study and are as discussed below.

3.4.1 Drude Model

Paul Drude first proposed the Drude model in 1900. This model describes how electrons are transported in a material. Drude model is based on the kinetic theory which presumes that molecules of a gas are identical to those of solid spheres and move in straight lines until they collide with one another. Drude model considers electrons as being unbound unlike the Lorentz model which assumes electrons are bound by a spring like force. According to Maghanga and Mwamburi, (2018), Drude model has shown to provide a better explanation of cases when electrons are having an appreciable interaction with each other. This can be used to study the optical properties at energies below the bandgap hence accounting for intraband transition of conducting electrons. Drude model has two adjustable parameters, damping constant γ and plasma frequency Ω_p. These two parameters are useful in computing the resistivity of the material and calculating the Drude dielectric susceptibility χ_{Drude}. The dielectric susceptibility is expressed in terms of frequency by the relation below (Maghanga and Mwamburi, 2018)

$$\chi_{Drude} = \frac{\Omega_p^2}{\omega^2 + i\omega\gamma} \tag{3.7}$$

3.4.2 OJL Model

O'Leary-Johnson-Lim (OJL) model describes the interband transition in semiconductors (O'Leary *et al.*, 1997). In this model, expressions that describe density of states are given in terms of optical transition between the valence and conduction band. The bands are presumed to be parabolic shaped with the tail decaying exponentially into bandgaps as in figure 3.4 below

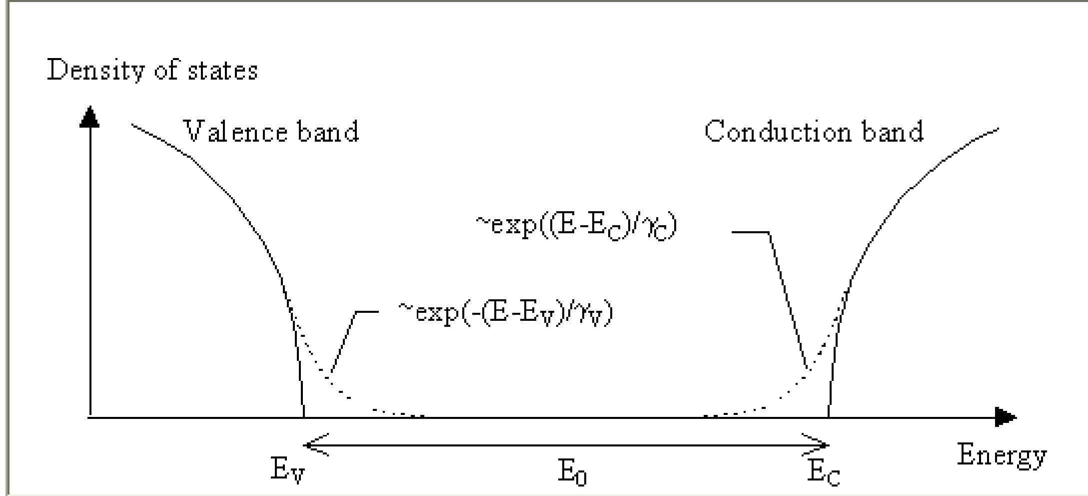

Fig 3. 4: The fit parameters of OJL interband transition (O'Leary *et al.*, 1997)

The OJL model fit parameters are mainly the energy gap E_0, damping constant for the valence and conduction bands (γ_V and γ_C), masses for the valence and conduction bands (MV and MC) which corresponds to the strength of the transition and the decay parameter g which drags the imaginary part towards zero for high frequencies.

3.4.3 KIM Oscillator Model

KIM oscillator was first suggested by Kim *et al.*, (1999). It is an extension of simple harmonic oscillator model which involves vibrations involving motion of atomic nuclei. This model is suitable for work that contains many oscillators. The model gives line shapes that are between Gaussian and Lorentzian and achieved by the following frequency dependence and damping constant (Kim *et al.*, 1999)

$$\chi_{KimOscillator} = \frac{\Omega_p^2}{\Omega_{TO}^2 - v^2 - iv\tau(v)} with \tau(v) = \Omega_\tau \exp(-\frac{1}{1+\sigma^2}(\frac{v-\Omega_{TO}}{\Omega_\tau})) \tag{3.8}$$

Where Ω_p is the oscillator strength, Ω_{TO} is the resonance position and Ω_τ is the damping constant.

3.5 Deposition Techniques of Thin Films

There are two major categories of depositing thin films, physical and chemical methods (Vossen *et al.*, 1991). In the chemical deposition method, the precursor undergoes a chemical reaction at the substrate to form a solid layer. The films deposited by the chemical method tend to be conformal. Examples of chemical deposition techniques include; chemical bath deposition (CBD), spin coating, dip coating, plasma enhanced chemical vapour deposition (PECVD), doctor blade among others. The physical deposition technique employs mechanical, electromechanical and thermodynamic means to deposit thin films. The system is kept under a vacuum to prevent contamination of the resulting film. In the PVD technique, the material to be deposited sublimes in a vacuum and the vapour of molecules or atoms condenses on the substrate surface to form a film. Examples PVD techniques include evaporation, sputtering, pulsed laser deposition (PLD), among others.

3.5.1 Sputtering Technique

Sputtering is one of the commonly applied physical vapour deposition technique. It is one of the best techniques employed in microelectronics industries. There are two types of sputtering; radio frequency (RF) and direct current (DC) sputtering. Direct current sputtering is suitable for conducting targets while rf sputtering is best for semi-conducting or non- conducting. Generally, sputtering is a plasma based deposition process in which energetic particles such as electrons, photons, ions and neutrons are accelerated towards the target, strike it causing ejection of atoms from the surface (Chapman, 1980). This technique is carried out in a vacuum to allow the material to travel freely and condense on the substrate without reacting with other particles that might be in the chamber. Argon is normally utilized as an inert gas to prevent reactions. Compared to other deposition techniques, sputtering has got the following advantages (Chopra *et al.*, 2004):

- Several samples can be coated at the same time and therefore it saves time
- It offers better morphological control of the resulting thin film
- There is no or minimal contamination of the resulting film since the process is carried out in a vacuum.
- It is a simple and a cheap method of thin film deposition.

On the contrary, sputtering has been criticized for poor utilization of the target (Mattox, 2002). Usually, the target is damaged as a result of collision with the ions, neutrons and photons in the chamber. In addition, the deposition rate of some materials is quite low.

3.5.2 Reactive DC Magnetron Sputtering

This technique utilizes magnetic and electric fields to speed up the sputter rate in a reactive environment. Magnetic fields of strength B are channeled in the sputter chamber, and then are superimposed on the electric fields E between the substrate and the target. As a result, the electrons in the plasma experience a Lorentz force given in equation 3.9.

$$F = -q\,(E+V\times B) \qquad (3.9)$$

Where q and v are the charge and the velocity of the electron respectively

For instance, an electron that escapes the target at a velocity v and at an angle Θ to the magnetic field will experience a force $qvB\sin\Theta$ which is in the direction perpendicular to that of the magnetic field. The electrons then assume a helical path around the magnetic field. This enables them to undergo ionizing collisions with the gaseous neutrals near the cathode creating extra argon ions which leads to higher deposition rate. The magnetic field therefore enhances the ionization of electrons by increasing the path length of the electrons thus creating more chances for ionization (Ohring, 1992).

Reactive sputtering involves the use of an inert gas such as argon and a reactive gas such as nitrogen or oxygen. The reactive gas reacts with the target to form a nitrite or an oxide.

3.5.3 RF Magnetron Sputtering Technique

Radio frequency sputtering technique is mostly utilized when the target to be sputtered is an insulator or a semiconductor. Radio frequency sputtering solves the problem of charge building up when an insulating target is used. It yields high deposition rate at a relatively low pressure. Radio frequency power supply is connected to the sputter gun generating an electric field in the chamber. Electrons between the substrate and the target move and collide with the argon ions to form plasma. RF plasma diffuses throughout the chamber rather than concentrating near the target as with dc

sputtering. The argon ions bombard with the target knocking off atoms from its surface in vapour form. The vapour then condenses on the substrate surface forming a coating. By alternating the electrical potential, the target is frequently cleaned up of charge build-up which accumulates on the target surface.

3.6 Thin Film Formation Process

The process of thin film formation consists of the following major steps (Kern, 2012).

- The creation and ejection of materials to be deposited in the form of atoms or molecules
- Transportation of the atoms/molecules to the substrate in the form of vapour, spray or solid
- Deposition and adsorption of the material on the substrate to form a film through nucleation.

The above mentioned steps are influenced by the geometry of the deposition apparatus, pressure and substrate temperature. Figure 3.5 represents the mentioned steps

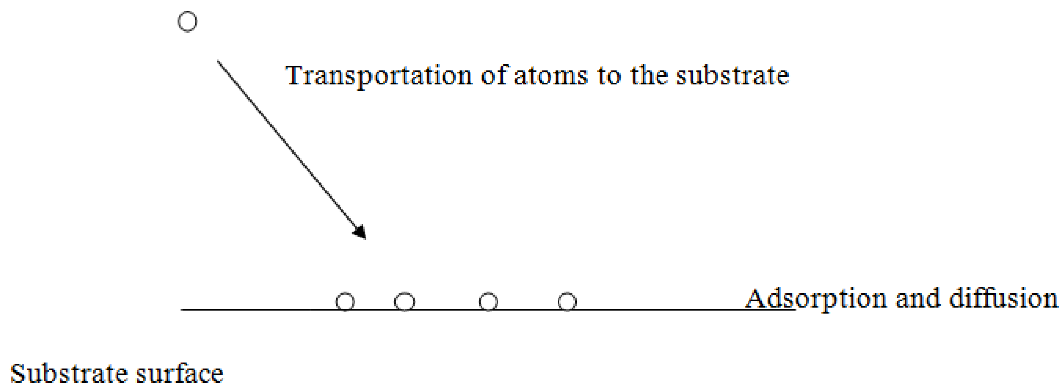

Fig 3. 5: Film formation process

3.6.1 Film Growth Models

Materials deposited onto a substrate exhibit three main modes of growth (Eaglesham and Cerullo, 1990):

i. Frank-van der Merwe (layer by layer) – In this mode, the force between adsorbate-adsorbate and the adsorbate-surface are balanced. The film is firmly bound to the substrate to form a uniform thickness. A good example is the growth of a metal on another metal or a semiconductor on another semiconductor.
ii. Volmer- Weber (Islands) - In this case, the film is firmly bound to each other than they are to the substrate, resulting in the nucleation of the coating species and formation of islands. A good example is the growth of metals on insulators.
iii. Stranski-Krastinov (layer plus lsland) - This is a combination of both layer and island growth modes. After the formation of several layers, the layer formation becomes unfavourable and therefore islands begin to form. An example is the growth of a metal on a semiconductor.

Figure 3.6 illustrates the three basic growth modes

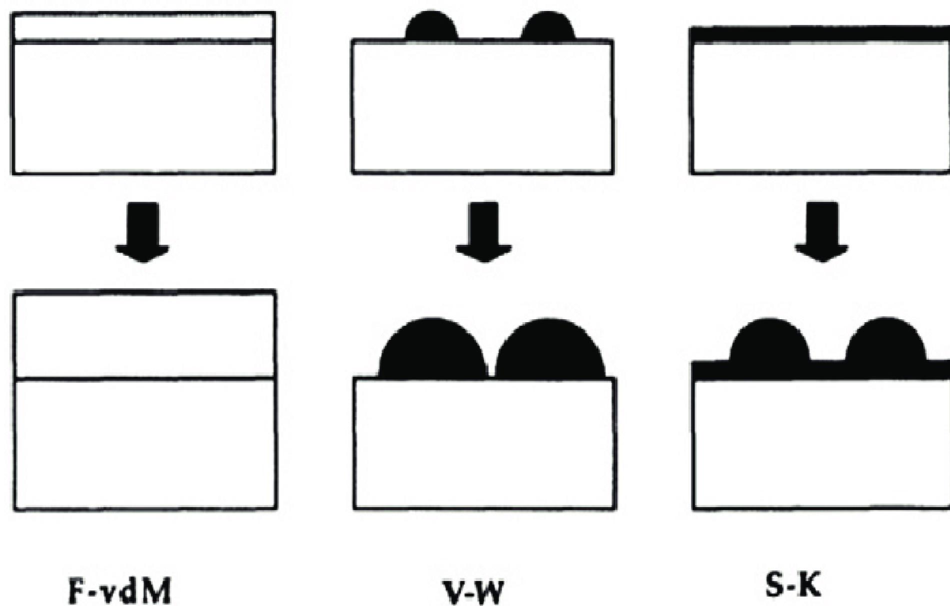

Fig 3. 6: The three growth modes of thin films (Eaglesham and Cerullo, 1990).

CHAPTER FOUR

MATERIAL AND METHODS

4.1 Introduction

This chapter highlights the experimental methods and material that have been used in the current study. It describes how TiO_2:Ge thin films were deposited and characterized using different techniques. All the films were deposited by rf sputtering followed by thermal annealing in air, argon and nitrogen. Optimization of the deposition parameters (argon flow rate and sputtering power) was done before the deposition of different ratios of TiO_2:Ge thin films.

4.2 Acquisition of Materials and Purity Levels

Pure TiO_2 and TiO_2: Ge composites disks which were used as targets were sourced from Kurt J Lesker, United States of America. The purity of the targets was 99.99%. The percentage ratios of TiO_2: Ge targets were 95:5, 90:10 and, 85:15 respectively. The diameter of all the targets was × 125” thick. The substrates used were Fluorine Doped Tin Oxide (FTO) (Hartford glass company USA) and plain glass substrates (20 mm × 20 mm × 20 mm) (from Kobian limited, Nairobi, Kenya).

4.3 Substrate Cleaning

The substrates were first soaked in a beaker containing a mixture of sodium hydroxide and liquid detergent for about 30 minutes to etch dirt from their surfaces. After that, they were cleaned by scrubbing gently using a piece of cotton wool and rinsed in de-ionized water. Thereafter, the substrates were ultrasonically cleaned in ethanol, acetone and de-ionized water each for 15 minutes successively. The cleaned substrates were dried in ambient air ready for deposition. The substrate cleaning procedure was as depicted in figure 4.1.

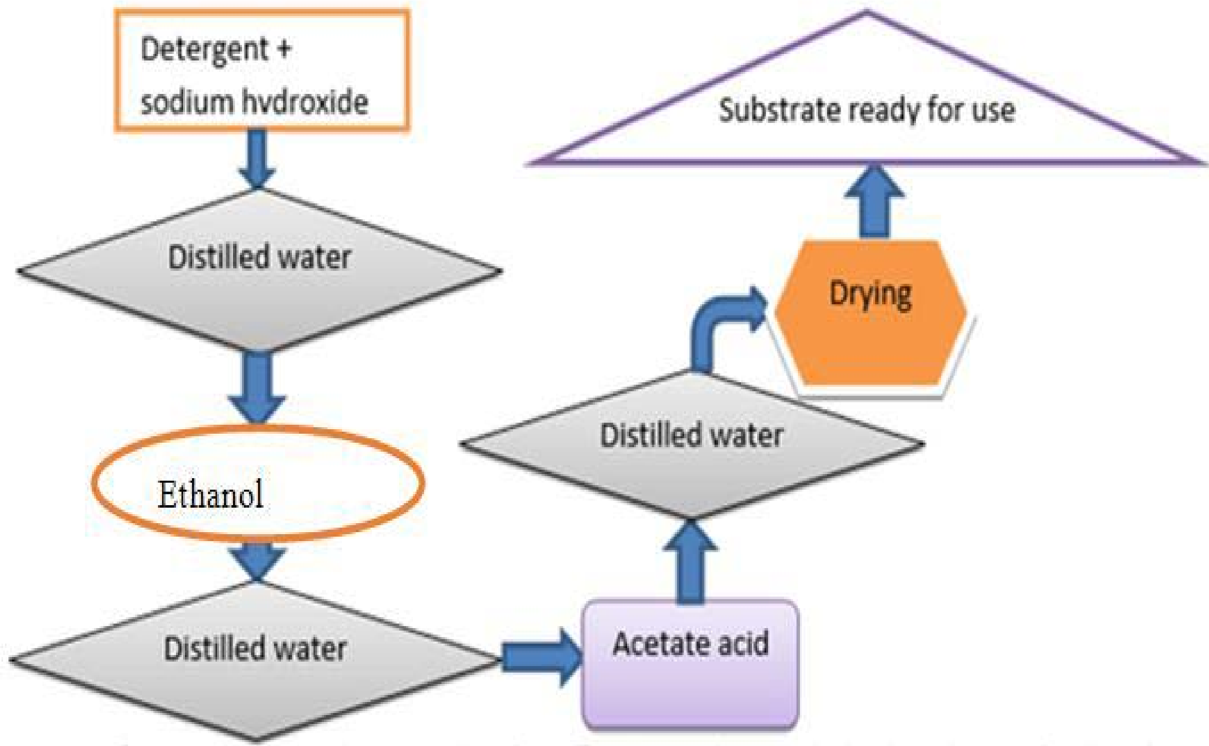

Fig 4. 1: The standard substrate cleaning procedure

4.4 Deposition of TiO_2:Ge Thin Films

TiO_2:Ge thin films were deposited by rf magnetron sputtering using an Edwards Auto 306 deposition system. Pure TiO_2 and TiO_2:Ge (99.99% pure) composites disks were used as targets. Prior to the sputtering process, the system was pumped down to a base pressure of 4.4×10^{-5} mbar (0.033 mtoe) using a turbo molecular pump to create a vacuum. TiO_2:Ge target was used as the cathode and was connected to the power supply while the substrate was used as the anode. The distance between the target and the substrate was maintained at about 15 cm for all the depositions. Pre- sputtering was done for about 10 minutes in pure argon to remove the surface contaminants from the target. The process/sputtering pressure was maintained at 6.0×10^{-3} mbar (4.5 mtoe). The deposition process was maintained at ambient (23.0-25.0 °C). The substrate holder was rotated at about 10 rounds per minute during the deposition to enhance uniformity of the film. Figure 4.2 below shows the auto 306 sputtering system chamber in the process of deposition.

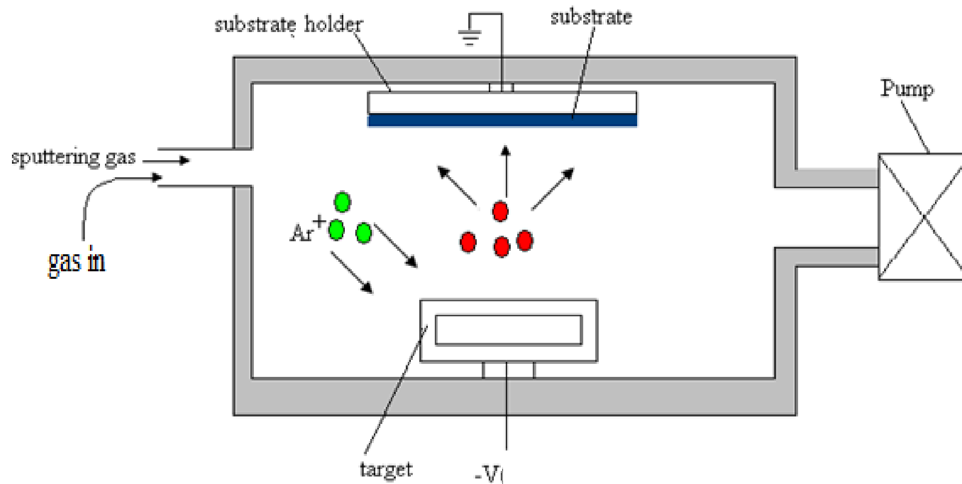

Fig 4. 2: Auto 306 sputtering chamber during deposition

The sputtering power and the argon flow rate were first optimized for preparation for TiO_2: Ge thin films. The optimum values for the sputtering power and the argon flow rate were then used in the deposition of TiO_2: Ge with varying compositional ratios (95:5, 90:10 and 85:15). The sputtering process was done for about $1\frac{1}{2}$ hours for all sets of TiO_2: Ge films. Table 4.1 below shows the sputtering conditions for deposition of TiO_2: Ge thin film.

Table 4. 1: Deposition parameters for TiO_2:Ge thin films.

Target	TiO_2:Ge
Pre-sputtering time	10 minutes
Sputtering time	$1\frac{1}{2}$ hours
Initial pressure	4.4×10^{-5} mbar
Sputtering pressure	6.0×10^{-3} mbar
Argon flow rate	35 sccm
Deposition temperature	Ambient (23.0-25.0 °C)
Sputtering power	220 W

4.5 Optimization of Argon Flow Rate and Sputtering Power

Titanium: Germanium composite (99.99% pure) in percentage ratio 95:5, was used as the target in the optimization process. In order to determine the optimal deposition power, the deposition process was performed for about 1 hour by varying the rf power from 75 W, 120 W, 150 W to 220 W while the argon flow rate was maintained at 80 sccm for all the depositions. Other parameters were maintained as stated in table 4.1 above. Similarly, in order to determine the optimal argon flow rate, the flow rate was also varied from 30 sccm, 35 sccm, 40 sccm to 60 sccm respectively while power was maintained at 150 W for all depositions. The films were later characterized optically and electrically and the optimum sputtering power and argon flow rate were determined.

To investigate the influence of annealing atmosphere on the films, the deposited thin films of TiO_2: Ge was annealed in three different environments: air, argon and nitrogen at 450 °C for about 1 hour for each sample. Figure 4.3 below shows a two dimensional tube furnace that was used for annealing the films. The respective gas was allowed into the tube furnace at a flow rate of about 20 ml/min during the annealing process. The annealed films were thereafter subjected to structural, optical and electrical characterization.

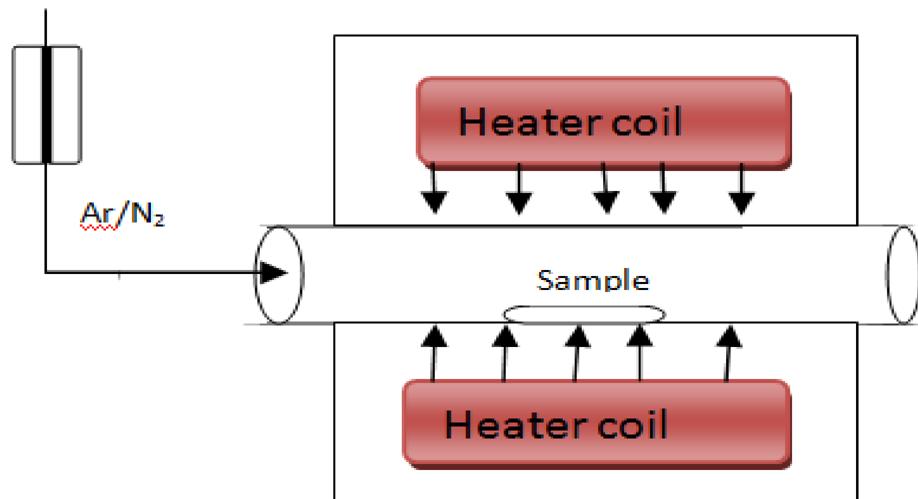

Fig 4. 3: The tube furnace set up for annealing samples

4.6 Optical Characterization

The absorbance and transmittance measurements were done using UV-VIS 3700 double beam Shimadzu spectrophotometer ranging between 300-1100 nm. Photons of certain wavelength and intensity (I_o) were channeled at the samples, and their respective transmittance and absorbance values recorded. Using the experimentally obtained data of optical transmittance in SCOUT 4.06 software (Theiss, 2012), other optical constants such as absorption coefficient, dielectric constant, and thickness of the film were determined. KIM oscillator, OJL model, Drude model and dielectric constants were used as the fitting parameters for the optical spectra of TiO_2:Ge semiconductor. The optical bandgap of the films was obtained from the extinction coefficient (k) extracted from the data simulated in SCOUT software using the Tauc's relation discussed in Chapter 3 subsection 3.3.3.

4.7 Electrical Characterization

The electrical resistivity was done using Jandel RM3-AR four-point probe. Figure 4.4 below is a sketch of a four-point probe system used in the measurement of resistivity. From the figure, a current was applied through the outer probes which in turn induced a voltage in the inner voltage probes.

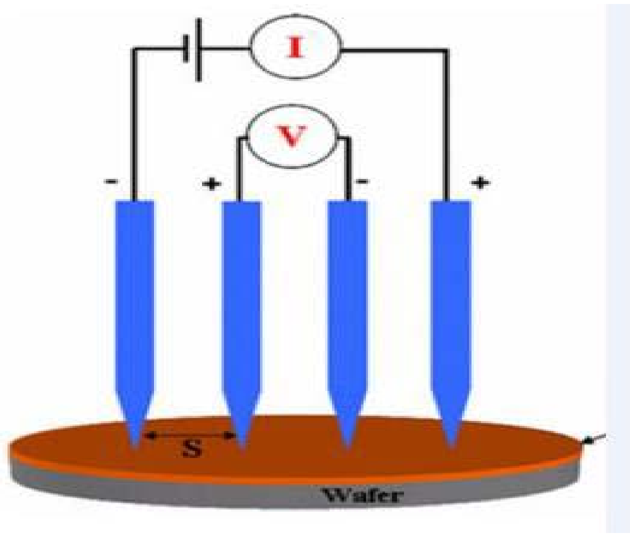

Fig 4. 4: The four point probe system (Ru *et al.*, 2011)

Using the voltage and current readings, the sheet and bulk resistivity (ρ_s) of the semiconductor was determined using equation 4.1 and 4.3 respectively (Ru *et al.*, 2011).

$$\rho_s = \frac{\pi}{\ln(2)} \frac{V}{I} \qquad (4.1)$$

But $\frac{\pi}{\ln(2)} = 4.53$

$$\rho_s = 4.53 \frac{V}{I} \qquad (4.2)$$

The bulk resistivity (ρ_b) of the semiconductor samples was determined using the film thickness and is given by

$$\rho_b = \frac{\pi}{In\ (2)} d(\frac{V}{I}) = 4.53d\ (\frac{V}{I}) \qquad (4.3)$$

Where d, is the film thickness

To confirm the resistivity values measured by the four point probe, SCOUT software was also helpful in analyzing electrical resistivity of the films using Drude model. The model consists of two adjustable parameters; dumping constant (Ω_{τ}) and plasma frequency (Ω_{p}). Using the plasma frequency and dumping constant, the electrical resistivity was given by equation 4.4 (Theiss, 2012).

$$\rho = \frac{\Omega_{\tau}}{2\pi c_0 \varepsilon_0 \Omega^2_{p}} = 59.9 \frac{\Omega_{\tau}}{\Omega^2_{p}} \tag{4.4}$$

4.8 Morphological and Structural Characterization

The morphological characteristics of TiO_2 and TiO_2:Ge thin films was studied using the scanning electron microscope (SEM) operating at 5 kV electron source model TM Gemini ZEISS ULTRA PLUS FEG SEM-Microscopes at Pretoria University, South Africa. The SEM micrographs images were taken using a charged coupled device camera interfaced to a computer. Various images of TiO_2:Ge films were taken with a magnification of $\times$50,000 for top view images.

X-ray diffraction (XRD) was performed to identify the crystal structure and the preferred orientation growth of the thin films. This was carried out using the Bruker D2 PHASER diffractometer with CuK_{α}. X-ray radiation (1.5418 Å) and readings were taken over the $10° < 2\theta < 80°$ range at a scan speed of 0.6 °/s and steps of 0.01 °.

4.9 Raman Spectroscopy

Raman spectroscopy was performed to determine the phases of TiO_2:Ge present in the films. The set up consisted of a confocal microscope with 50$\times$objective and a laser operation wavelength 532 nm. The TiO_2:Ge films were characterized under an exposure time of 10 seconds, accumulation of 7 and numerical aperture of 0.5. A laser beam in the visible range was used to illuminate the film. The scattered light was then collected using a lens, sent through a filter to obtain Raman spectra of the films. The Raman shift provides the information about the vibration, rotational and phases of the sample.

4.10 Elemental Analysis-EDXRF

The elemental analysis of TiO_2:Ge films was done using the Energy Dispersive X-ray Fluorescence (EDXRF) spectroscopy, Shimadzu series EDX-800HS model CE (212-23701-36). The spectroscopy is widely used for elemental analysis because it is non-destructive, simple, and rapid and has highly reproducible features. The machine works in the following steps (Geraki *et al.*, 2003):

- The sample is irradiated with high energy X-rays from a controlled X-ray tube
- The x-ray energy causes an electron to be excited from a lower to a higher energy state
- For the atom to regain stability, an electron drops back to the lower energy state to fill the vacancy left releasing x-ray fluorescent
- Each of the elements present in the sample produces a set of characteristics x-ray fluorescent that is unique for that specific element.
- X-ray fluorescent peaks with varying intensities are created. The peak intensity indicates the concentration, while the peak energy identifies the specific element.

Figure 4.5 shows the energy dispersive x-ray fluorescent set up used for the elemental analysis of the thin film samples.

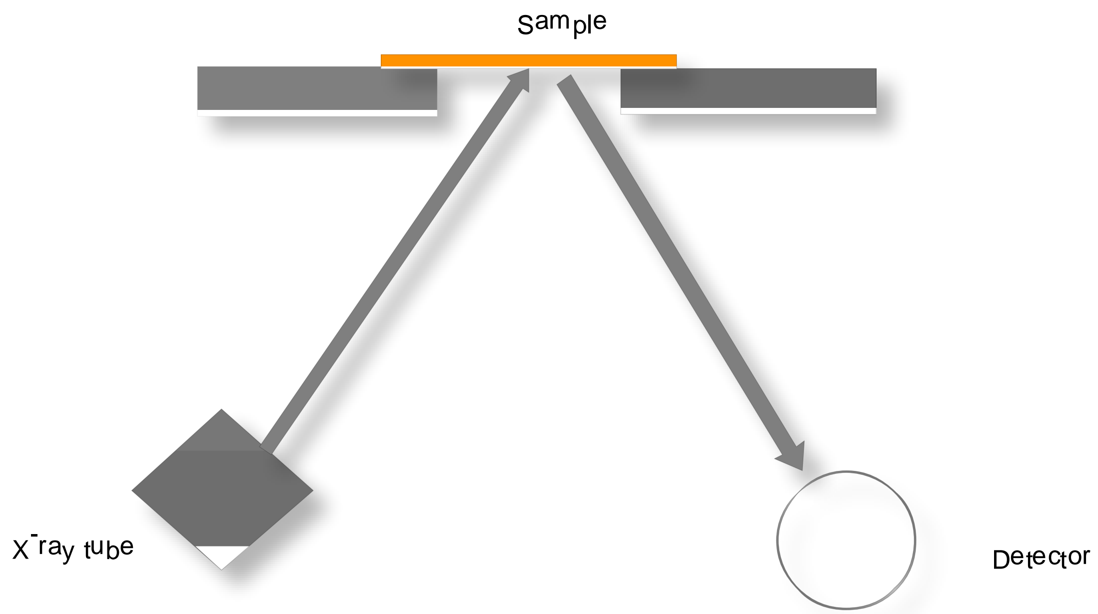

Fig 4. 5: X-ray Fluorescent set up

CHAPTER FIVE

RESULTS AND DISCUSSION

5.1 Introduction

The chapter focuses on results and analysis of the properties of TiO_2:Ge thin films annealed in different ambient. The electrical and optical properties of TiO_2:Ge films deposited with different concentration of Ge are analyzed and discussed. Structural and morphological characteristics of the films are also discussed using XRD pattern and SEM micrographs images respectively.

5.2 Raman Spectroscopy

The molecular species of the films was determined using Raman spectroscopy. Figure 5.1 shows a representative spectrum for the annealed (450 °C for 1 hour) TiO_2:Ge thin films sputtered at different powers. A peak with a strong signal appeared at 142 cm^{-1} followed by peaks with low-intensity at 192, 392, 516, and 639 cm^{-1}, respectively. All the films deposited at different rf powers correspond to the vibration mode of pure anatase phase of TiO_2, an observation also made by Castrejón-Sánchez *et al.*, (2014). From figure 5.1, deposition power did not have any effect on the film spectra output in contrary to the findings by Lu *et al.*, (2001) who found that as power increases, the intensity in peaks also increases. This implies that in this study, the vibration mode of the film and thus the phase did not depend on the power applied.

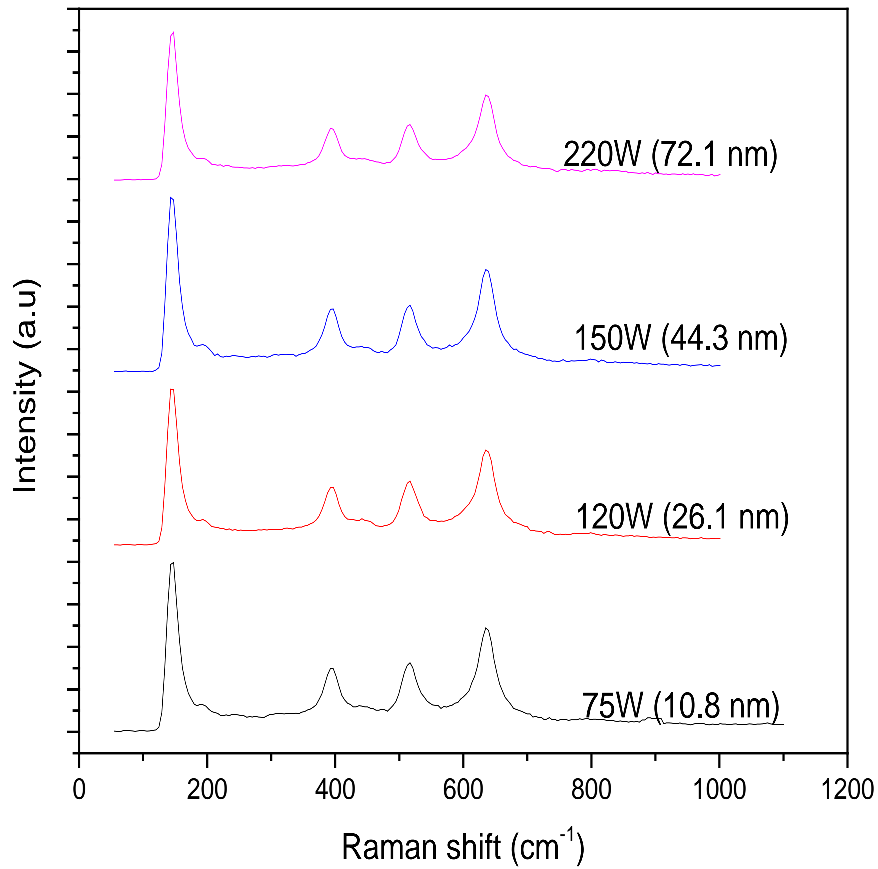

Fig 5. 1: Raman spectra for annealed TiO_2:Ge (95:5) thin films deposited at various sputtering powers.

5.3 Energy Dispersive X-Ray Fluorescence for TiO_2:Ge Thin films

Figure 5.2 below is a survey scan for TiO_2:Ge thin films (95:5) using the energy- dispersive X-ray fluorescence. The peaks detected in the scan correspond to the difference in the energy spectra between the upper and the lower energy states for the different elements, as shown below. It is clear that titanium and germanium elements were present in the films. The K-alpha for titanium and germanium is 4.512 and 9.886 KeV respectively. The graph shows that the intensity of titanium in the film was higher compared to that of Germanium. This is because, according to the specification of the target, titanium had a higher percentage in terms of composition than

germanium. Apart from Ti and Ge, other elements such as Sn, Ca and Cu are present since they are elements present in a glass.

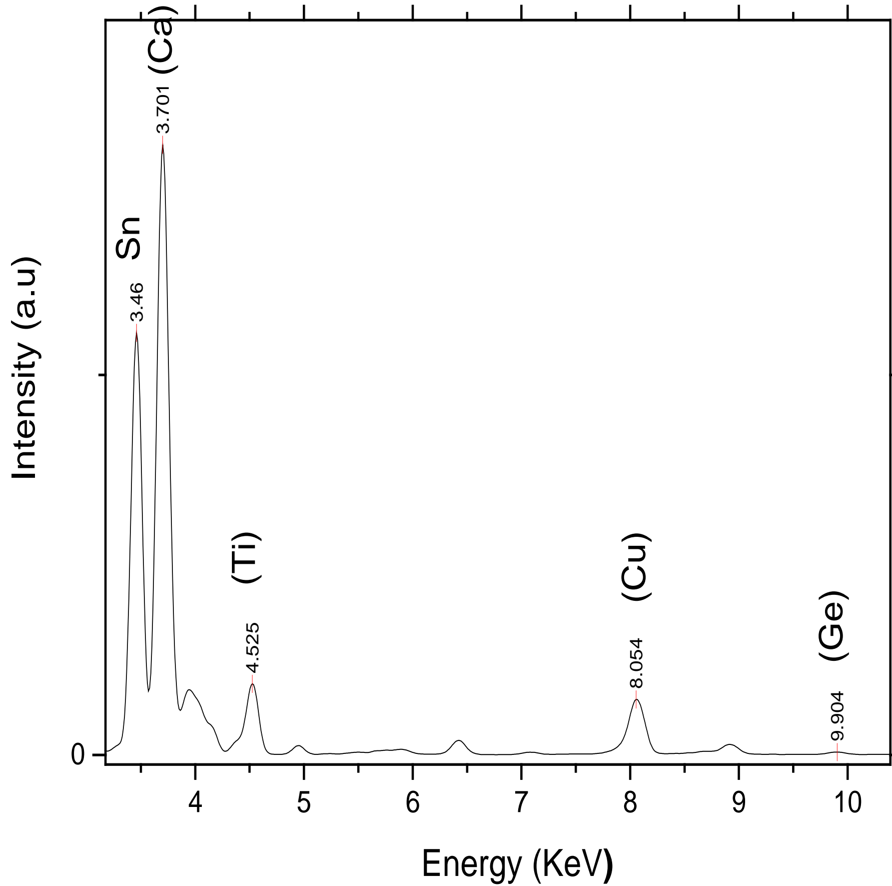

Fig 5. 2: EDXRF energy spectrum for TiO_2:Ge (95:5) thin films

5.4 Effect of Annealing and Sputtering Power on Optical Properties for TiO_2:Ge Thin Films

The transmittance data was obtained from UV_VIS spectrophotometer (Shimadzu single beam) and plotted using origin version pro 9.1 64 Bits. The optical transmittance (T), the energy bandgap (E_g), refractive index (n_f), and the extinction coefficient (k_λ) of TiO_2:Ge (95:5) thin films sputtered under various sputtering powers, and argon flow rates as a function of annealing are discussed.

In terms of physical appearance, TiO_2:Ge thin films without thermal treatment were opaque but after thermal treatment at 450 °C for 1 hour in air, they became transparent. Annealing treatment improved the surface quality, caused nucleation to occur, resulting in enhanced grain size. This caused an increase in transmission spectra in the visible range (Hasan *et al.*, 2008). However, the films annealed in nitrogen and argon atmospheres turned dark brown. This colour change may be attributed to the oxygen loss from titanium to form oxygen vacancy defects, which intensified as the argon and nitrogen concentration increased (Ghicov *et al.*, 2006). A similar colour change effect was also reported by Gamboa and Pasquevich, (1992) in his study on the effect of chlorine atmosphere on TiO_2 anatase- rutile phase. The darker colour also indicates more light absorption in the visible region (Folger *et al.*, 2017).

5.4.1 Transmittance

Figure 5.3 below displays the UV-VIS transmittance spectra for the as-deposited and annealed (450 °C) TiO_2:Ge thin films deposited with sputtering powers of 75 W, 120 W, 150 W and 220 W. The optical transmittance for both the as-deposited and the annealed films showed a gradual increase in transmittance between the wavelength 300 nm-600 nm. Within the visible range (400-700 nm), the average transmittance for the as-deposited films was as follows: about 86% (75 W (22.3 nm)), 79% (120 W (41.6 nm)), 72% (150 W (61 nm)) and 67% (220 W (78.1 nm)). The annealed films recorded a higher transmittance than the as-deposited films averaging about 89% (75 W (10.8nm)), 87% (120 W (26.1 nm)), 82% (150 W (44.3 nm) and 76% (220 W (72.1nm). There was an increase in transmittance of between 3-10 % on annealing the films depending on the film thickness. An increase in steepness was also noted for the annealed films and this implied higher transmittance. The higher transmittance for the annealed films could be attributed to improved crystallinity and better homogeneity of the films (Zhu *et al.*, 2010), and also may be due to less film thickness recorded by the annealed films. Below 400 nm, there was a decrease in transmission which could be due to a number of factors including; light absorption by the films which could result in electrons being excited from the valence to the conduction band, absorption by the glass and multiple reflections by glass (El-Raheem and Al-Baradi, 2013). Thin film deposited at 75W exhibited the highest transmittance in the visible range. This was related to the less thickness it recorded of about 22.3 nm. The thickness of TiO_2:Ge thin films increased with sputtering power, and therefore the films deposited at 220 W showed the lowest transmittance.

More power implies more sputter material being generated and hence for the same deposition time, the films deposited at the highest power tend to exhibit more thickness.

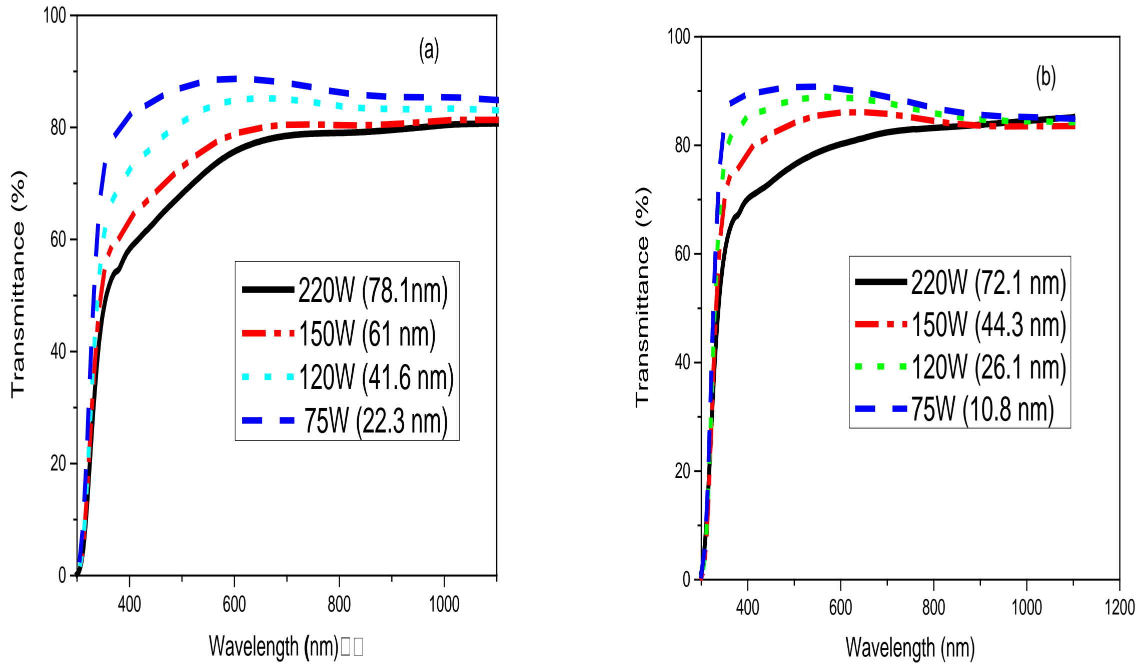

Fig 5. 3: Optical transmittance for as-deposited (a) and annealed (b) TiO_2:Ge (95:5) thin films deposited at different sputtering powers

The thickness of both the as-deposited and the annealed films (450 °C) of TiO_2:Ge thin films deposited at different sputtering powers was estimated by simulating the transmittance data in scout software. This was done by obtaining a spectra fit using the dielectric constant, Drude model, KIM model and OJL model (Theiss, 2012). The extinction coefficient, absorption coefficient, and refractive index of the films were then extracted from the simulated data. Figure 5.4 displays the simulated and the experimental graphs using scout software for annealed films deposited at 75 W and 150 W. It is clear that the simulated curves agree well with the experimental data and therefore, the material property could be described accurately.

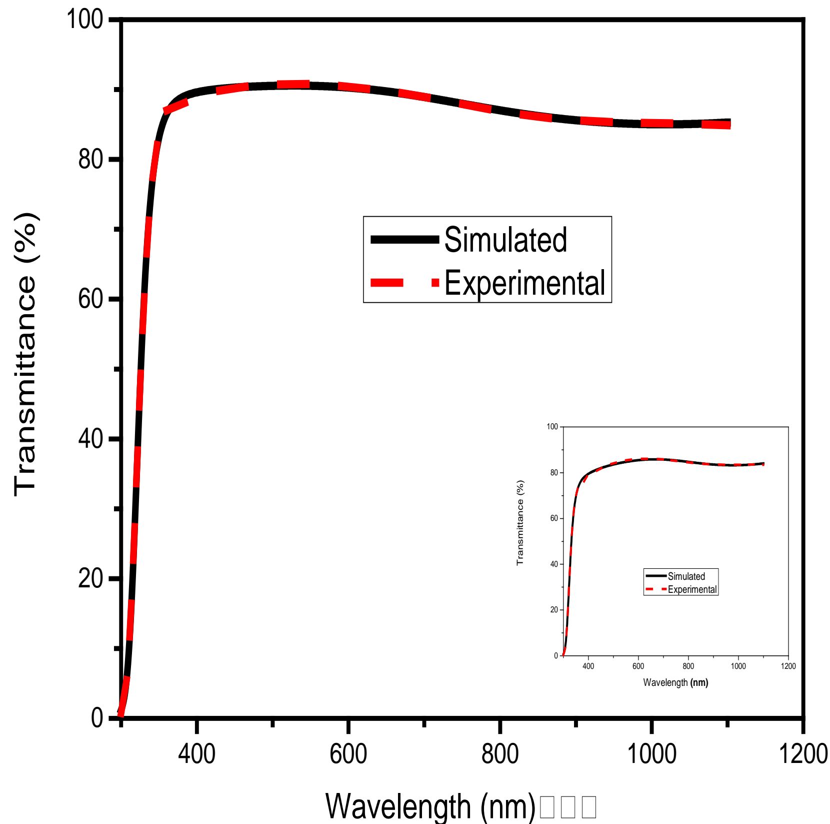

Fig 5. 4: SCOUT fitting for transmittance spectra for annealed TiO_2:Ge thin films deposited with sputtering power of 150 W (44.3 nm): Inset is SCOUT fitting transmittance graph for annealed TiO_2:Ge films deposited at 75 W (10.8 nm)

The annealed TiO_2:Ge thin films deposited at 220 W,150 W, 120 W, and 75 W exhibited a thickness of 72.1 nm, 44.3 nm, 26.1 nm, and 10.8 nm respectively. An increase in sputtering power contributed to an increase in atom mobility and deposition rate resulting in the growth of crystallite sizes as well as surface roughness hence an increase in thickness (Chen *et al.*, 2005). It is expected that low sputtering power exhibits low deposition rate due to less energetic argon flow rate. Similar results were obtained by Muslim *et al.*, (2015).

Table 5.1 summarizes variation of thickness and sputtering yield with sputtering power for both the as-deposited and the annealed films of TiO_2:Ge thin films

Table 5. 1: Thickness and yield rate for as-deposited and annealed TiO_2:Ge films deposited at different powers

Power (W) (± 0.1)	**Thickness (nm) (as-deposited) (±0.1)**	**Thickness (nm) (annealed) (±0.1)**	**Sputtering Yield (nm/min) (as-deposited) (±0.01)**
75.0	22.3	10.8	0.37
120.0	41.6	26.1	0.69
150.0	61.0	44.3	1.02
220.0	78.1	72.1	1.30

Figure 5.5 shows the qualitative dependence of thickness as well as yield rate for TiO_2:Ge thin films as a function of sputtering power. It was observed that, thickness and yield rate for TiO_2:Ge films increased with increasing power linearly. This is because more power ejects more sputter material from the target.

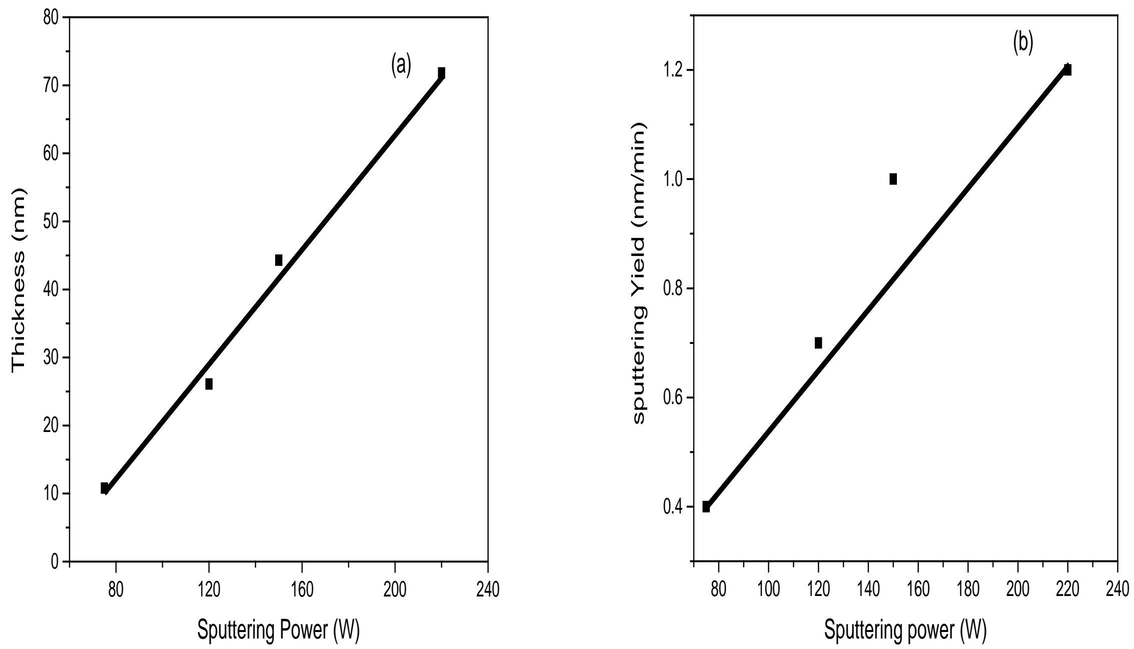

Fig 5. 5: Variation of film thickness (a) and sputtering yield (b) with sputtering power for TiO_2:Ge films.

5.4.2 Absorbance

Figure 5.6 displays the absorbance versus wavelength spectra for TiO_2:Ge thin films sputtered at various powers.

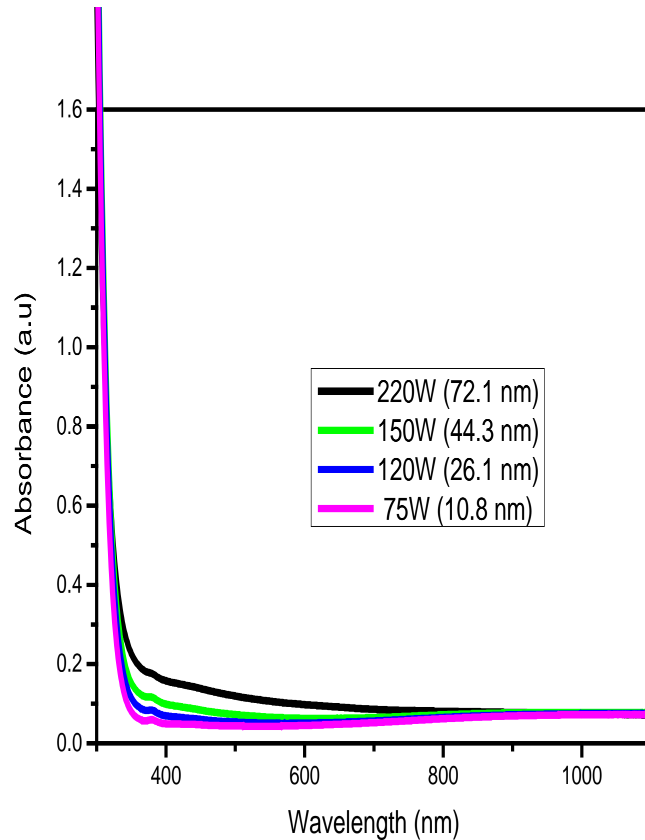

Fig 5. 6: Variation of absorbance with sputtering power for TiO_2:Ge (95:5) films

The spectra show an increasing absorbance with increase in sputtering power. This was due to change in the film density. The thickest of the films deposited at 220 W (72.1 nm) recorded the highest absorbance. The enhancement of absorption of light in the visible region indicates an increase in the light harvesting capability. However, studies have established that TiO_2 films of a thickness of about 10 µm have optimal light absorption ability (Huang and Wong, 2011). This explains the reason why the absorption rate is still low in this study since the thickness of the films was quite small.

5.4.3 Optical Energy Bandgap

The energy bandgap (E_g) of TiO_2:Ge films sputtered at different powers was determined using Tauc extrapolation method by plotting $h\upsilon$ on the horizontal axis against $(\alpha h\upsilon)^{\frac{1}{2}}$ on the vertical

axis as shown in figure 5.7. The bandgaps of 3.31 eV, 3.52 eV, 3.58 eV, and 3.59 eV were obtained for powers 220 W, 150 W, 120 W, and 75 W respectively.

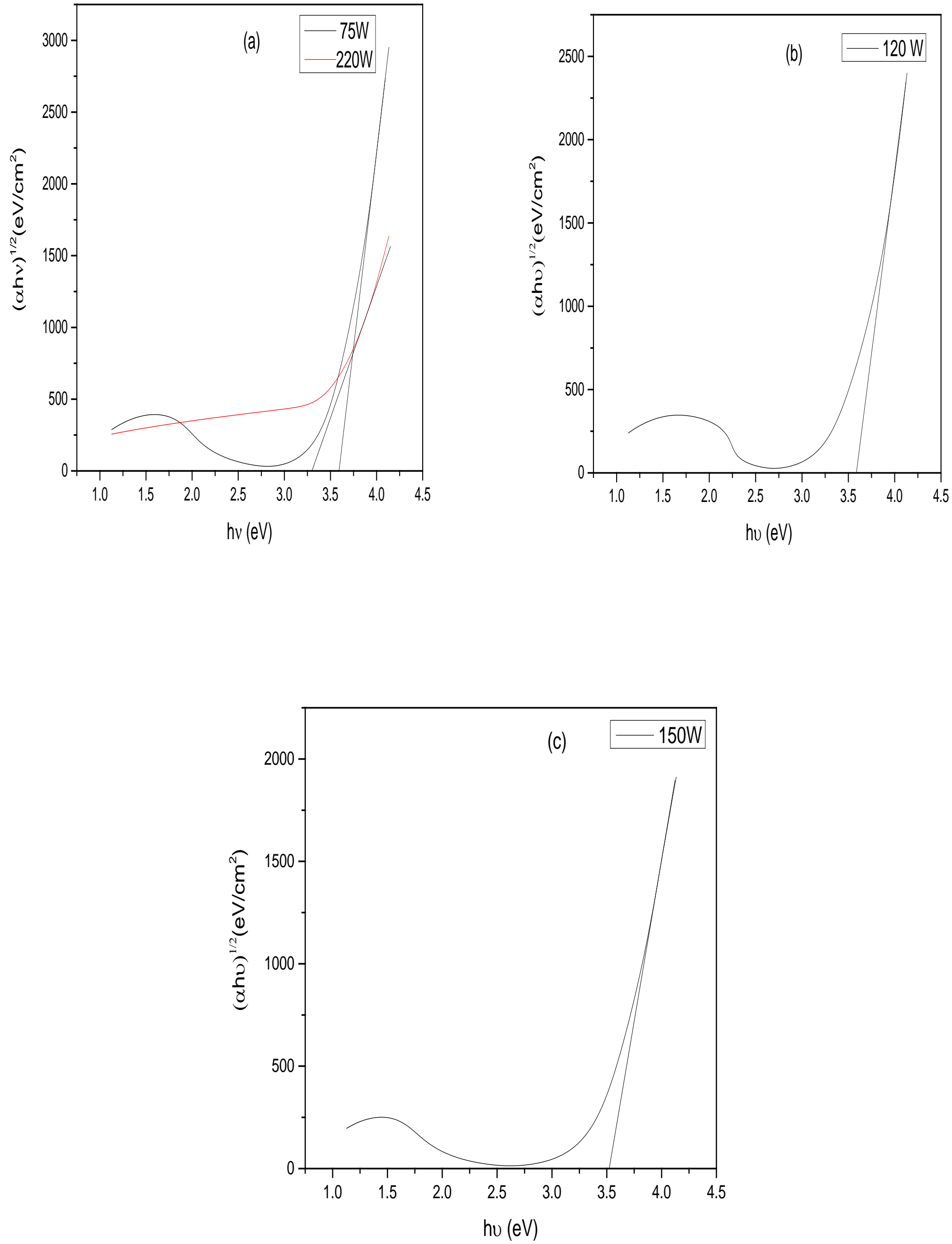

Fig 5. 7: The energy bandgaps for the annealed TiO_2:Ge (95:5) films deposited at 75 W and 220 W (a), 120 W (b) and 150 W (c)

The optical bandgap decreased with increase in sputtering power, in agreement with other authors. Aly and Akl, (2015) explained the observation as an increase in sputtering power results in increased film thickness which gives more enhancements of order and localized states and therefore reducing the defects. In amorphous TiO_2:Ge films deposited at 75W, the number of defects are expected to be higher due to unsaturated bonds thereby resulting in higher optical bandgap. Nair *et al.*, (2011) argued that the decrease in optical bandgap (3.59 eV- 3.31 eV) with increasing power (75 W-220 W) could also be an indication of phase transformation from amorphous to anatase. This implies that films deposited at higher sputtering power are more crystalline compared to the films deposited at lower sputtering power. The crystallinity of a film improves with increase in thickness (Jeyachandran *et al.*, 2007). Others have developed an inverse relationship between the bandgap and the film thickness as shown in equation 5.1 below (Goh *et al.*, 2010).

$$\Delta E_g \sim \frac{\hbar^2}{2md^2} \tag{5.1}$$

Where d is the thickness and m are the effective mass carrier of the films.

Figure 5.8 shows how energy bandgap varies with sputtering power for TiO_2:Ge (95:5) thin films.

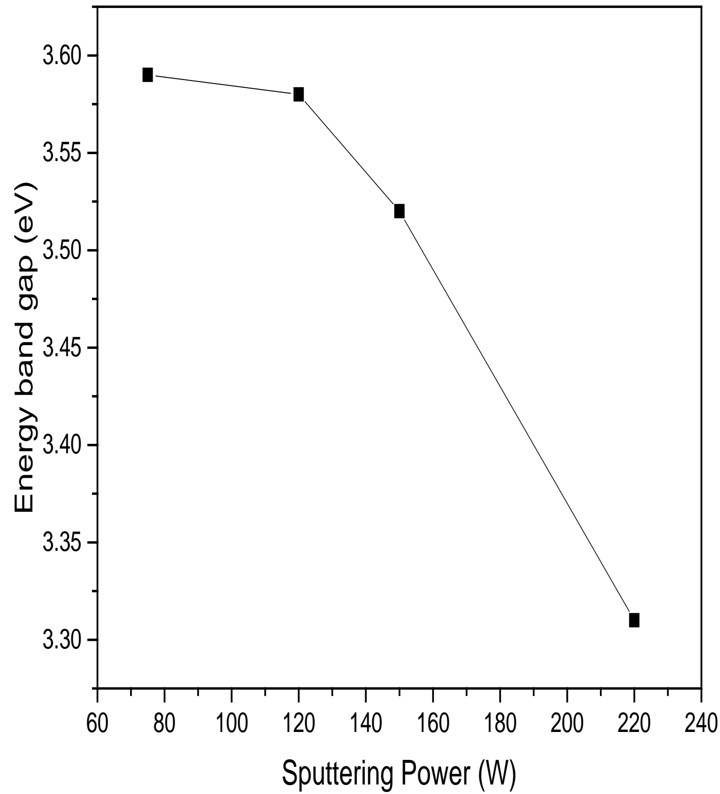

Fig 5. 8: Energy bandgap versus sputtering power for TiO_2:Ge (95:5) thin films.

5.4.4 Refractive Index (n_f)

Figure 5.9 shows a plot of refractive index (n_f) against wavelength for films deposited at various rf sputtering powers. From the graph, the refractive index of the films increased with increasing sputtering power. This was attributed to several factors including; densification of layers as a result of the increase in the film thickness, improved crystallinity of the films, and oxygen deficiency that occurs at high sputtering powers (Suhail *et al.*, 1992).

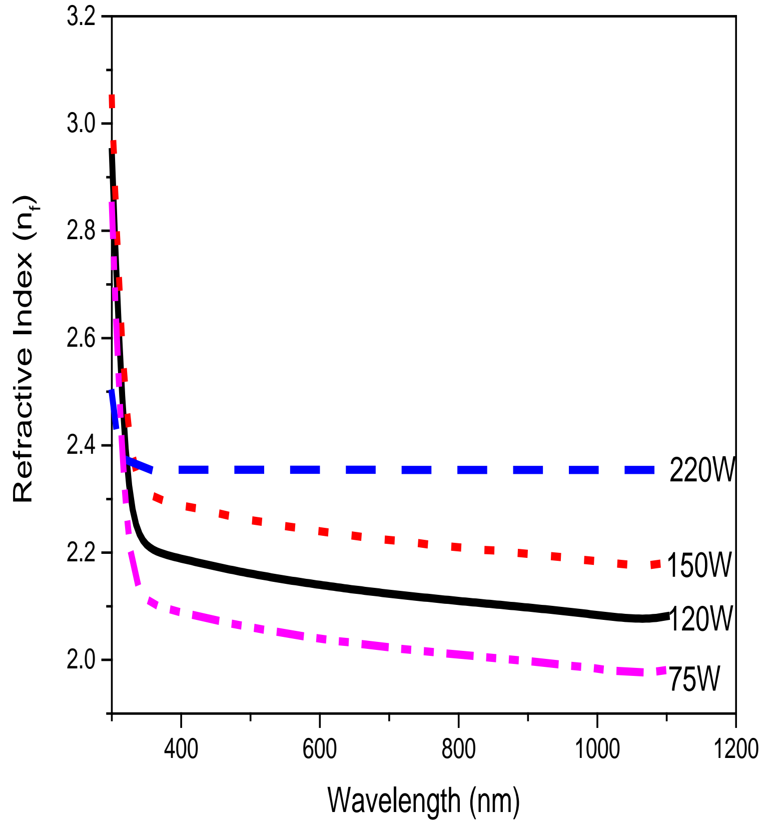

Fig 5. 9: Refractive index versus wavelength for TiO_2:Ge (95:5) films deposited at various sputtering powers

The dependence of refractive index on the film porosity could be explained using the Lorentz-Lorenz relation which is defined as the ratio of average film density to bulk density (Waita *et al.*, 2007; Pulker, 1979).

$$P = \frac{\rho_{TiO_2:Ge}}{\rho_{TiO_2}} = \left(1 - \frac{n^2_{TiO_2:Ge} - 1}{n^2_{TiO_2:Ge} + 2} \cdot \frac{n^2_{TiO_2} + 2}{n^2_{TiO_2} - 1}\right) \tag{5.2}$$

Where n_{TiO_2} and $n_{TiO_2:Ge}$ are the refractive indices of dense TiO_2 anatase phase (2.46) and that of the deposited films (TiO_2:Ge), respectively. Using the relation above the porosity for the films deposited at 75 W, 120 W, 150 W, and 220 W at wavelength 550 nm were 17.7%, 11.4%, 8.3%, and 4.2% respectively.

Figure 5.10 shows a graph of the refractive index against wavelength for as-deposited and annealed (450 °C) TiO_2:Ge thin films deposited at 150 W. The refractive index was high for the annealed films compared to the as-deposited films. This could be explained by the fact that annealing the films resulted to a decrease in porosity and also transformed the films from amorphous to crystalline anatase, leading to an increase in the refractive index of the film. The dense material has a high refractive index since more electric dipoles are activated when the material is exposed to electric field of the incoming light (Aksay and Altıokka, 2007).

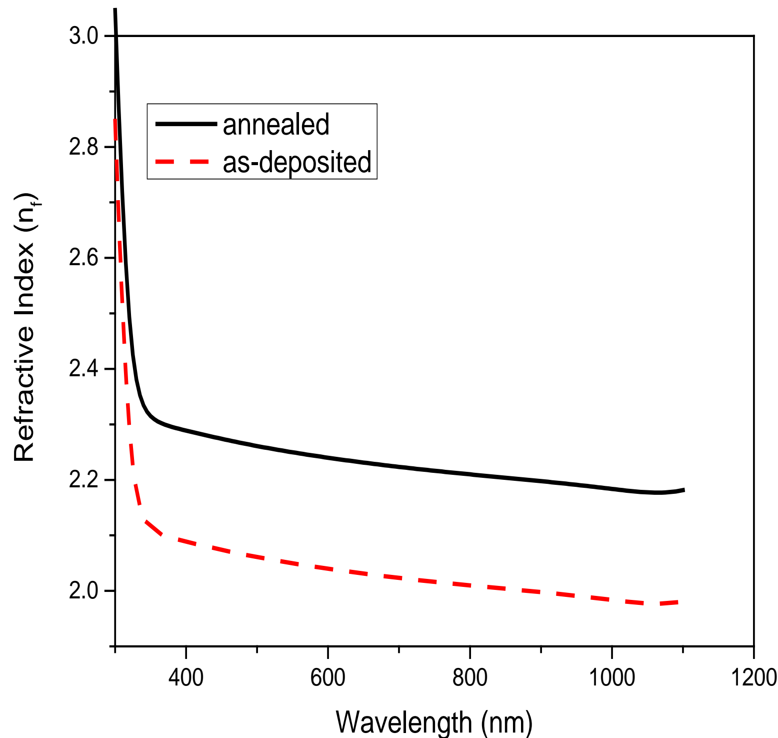

Fig 5. 10: Refractive index versus wavelength for as-deposited and annealed TiO_2:Ge (95:5) films deposited at 150 W

5.4.5 Extinction Coefficient (k_λ)

Figure 5.11 displays the extinction coefficient (k_λ) against wavelength curves for TiO_2:Ge (95:5) thin films deposited at various rf powers at room temperature (23-25 °C). It was noted that there was a decrease in the extinction coefficient with the increase in sputtering power.

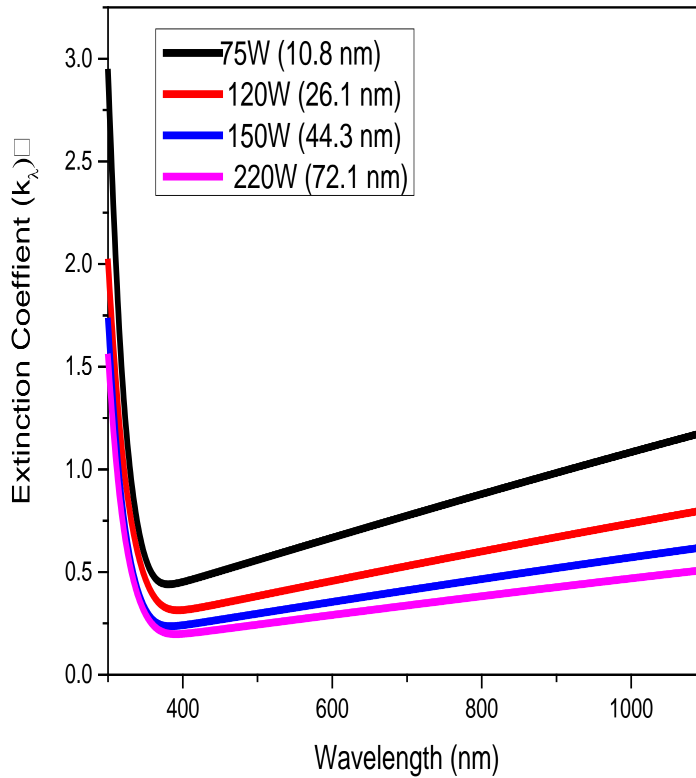

Fig 5. 11: Extinction coefficient versus wavelength for annealed TiO_2:Ge (95:5) films deposited at various sputtering powers

The extinction coefficient can be obtained from the relation (Ilican *et al.*, 2007).

$$k_\lambda = \frac{\lambda a}{4\pi d} \tag{5.3}$$

where, d, λ, and α refer to the film thickness, the wavelength and its absorption coefficient respectively. It is expected that the extinction coefficient (k_{λ}), increases with a decreasing film thickness (Ilican *et al.*, 2007)

Figure 5.12 displays a graph of the extinction coefficient against wavelength for as-deposited and annealed (450 °C) TiO_2:Ge films deposited at room temperature. It was observed that the extinction coefficient for the annealed films was higher than for as-deposited films. The increase in the extinction coefficient was attributed to a decrease in the bandgap energy for the annealed films (Eiamchai *et al.*, 2009).

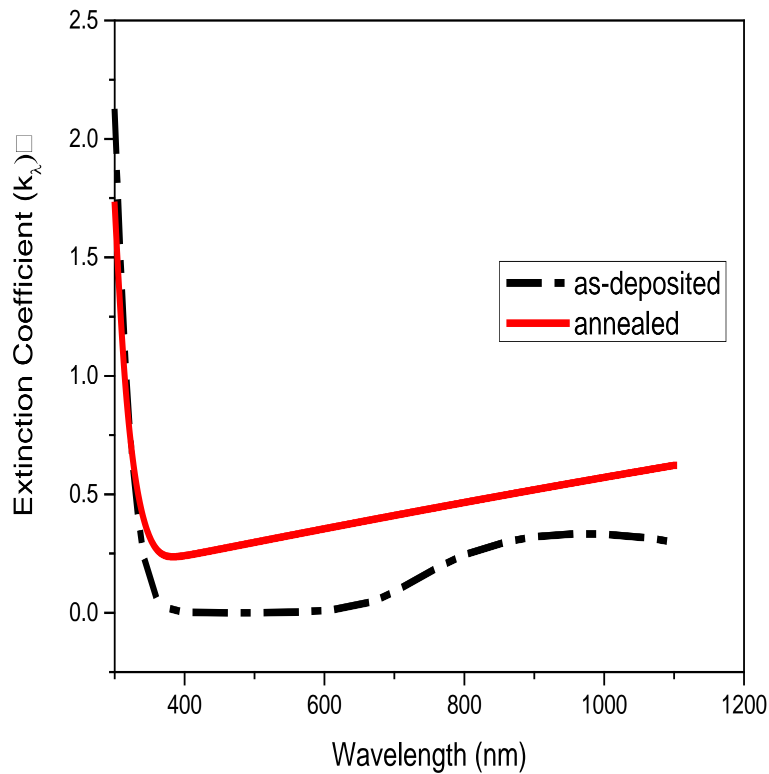

Fig 5. 12: Extinction coefficient against wavelength for as-deposited and annealed TiO_2:Ge (95:5) film deposited at 150 W

5.5 Influence of Sputtering Power on Electrical Resistivity for TiO_2:Ge Thin Films

Table 5.2 and figure 5.13 show the dependence of resistivity and conductivity on the sputtering power for both the as-deposited and annealed TiO_2:Ge thin films. It was observed that the room temperature resistivity decreased after the annealing process. This was because thermal treatment improved the crystallinity of the films which made it easier for electrons to pass through one grain to another in the TiO_2:Ge lattice (Senain *et al.*, 2010). It was also noted that resistivity decreased with increasing sputtering power. This implies that as power increases, the atoms gain larger driving force to move to the appropriate lattice sites resulting to a more perfect and crystalline thin films hence lowering the resistivity (Lu *et al.*, 2001).

Table 5. 2: Resistivity and conductivity for as-deposited and annealed TiO_2:Ge thin films deposited at different powers.

Power (W) (±0.1)	**Resistivity from 4-point probe (10^{-2} Ω-cm) (as-deposited) (±0.01)**	**Resistivity from 4-point probe (10^{-2}Ω-cm) (annealed) (±0.01)**	**Percentage Change in Resistivity (%) (±0.01)**	**Resistivity from SCOUT (10^{-2}Ω-cm) (annealed) (±0.01)**	**Conductivity (Siemen'scm^{-1}) (annealed) (±0.01)**
75.0	10.34	9.51	8.03	9.60	10.52
120.0	6.71	6.49	3.28	6.52	15.41
150.0	3.97	3.77	5.04	3.83	26.53
220.0	1.95	1.61	17.44	1.62	62.11

The behavior observed in this study was similar to the observations made by Muslim *et al.*, (2015) in their study on the influence of sputtering power on TiO_2 properties. Contrary to these findings, several researchers had earlier on reported an increase in the resistivity for TiO_2 films as they become thicker (Domtau *et al.*, 2016; O'regan and Grätzel, 1991). However, the thickness of their films was more than 1µm whereas in the present study, the thickness ranged between 10.8 nm – 72.1 nm. Also, the presence of Ge in TiO_2 could have contributed to the differences.

The electrical conductivity was obtained using the following relation;

$$\sigma = \frac{1}{\rho} \tag{5.4}$$

From the relation, resistivity and conductivity are reciprocal of each other. The conductivity for TiO_2:Ge films increased with increase in sputtering power (thickness). A decrease in resistivity upon annealing of the films was also as a result of increase in the grain size which leads to a decrease in grain boundaries for the films (Biju and Jain, 2008). The values for the resistivity for the films are represented in figure 5.13.

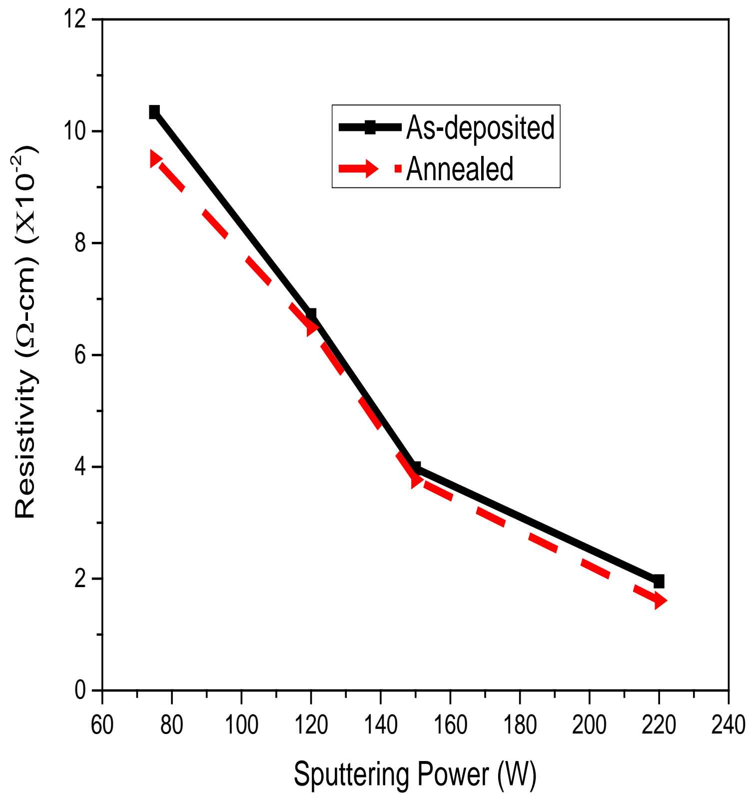

Fig 5. 13: Resistivity for the as-deposited and annealed TiO_2:Ge (95:5) films deposited at different sputtering powers

5.6 Influence of Argon Flow Rate on Optical Properties for TiO_2:Ge Thin Films

5.6.1 Transmittance

Figure 5.14 shows the transmittance spectra for TiO_2:Ge thin films deposited at various argon flow rates (30-60 sccm). The transmittance of all the films were almost equal since the line graphs are concentrated at the same level. The annealed films showed the highest average transmittance of > 80% between the wavelengths 400 – 700 nm. The as-deposited films showed a lower transmittance averaging 70% in the visible range. The lower transparency associated with the as-deposited thin films may be due to its short range of particles which may not allow light to pass through easily like in crystalline films. From figure 5.14 (b), the transparency of annealed films increased with increasing argon flow rate. The film deposited at 60 sccm showed the highest transparency while the one deposited at 30 sccm showed the lowest. Higher flow rates could lead to stronger collision between the argon atoms and the sputtered target atoms, which in turn reduce the kinetic energy of the sputtered atoms and limit their migration capability towards the substrate resulting in small grain size of the film. Secondly, increase in argon flow rate introduces more argon atoms in the film resulting to structural defects. These two factors explains why the TiO_2:Ge film deposited at 60 sccm had the highest transparency (Lu *et al.*, 2001).

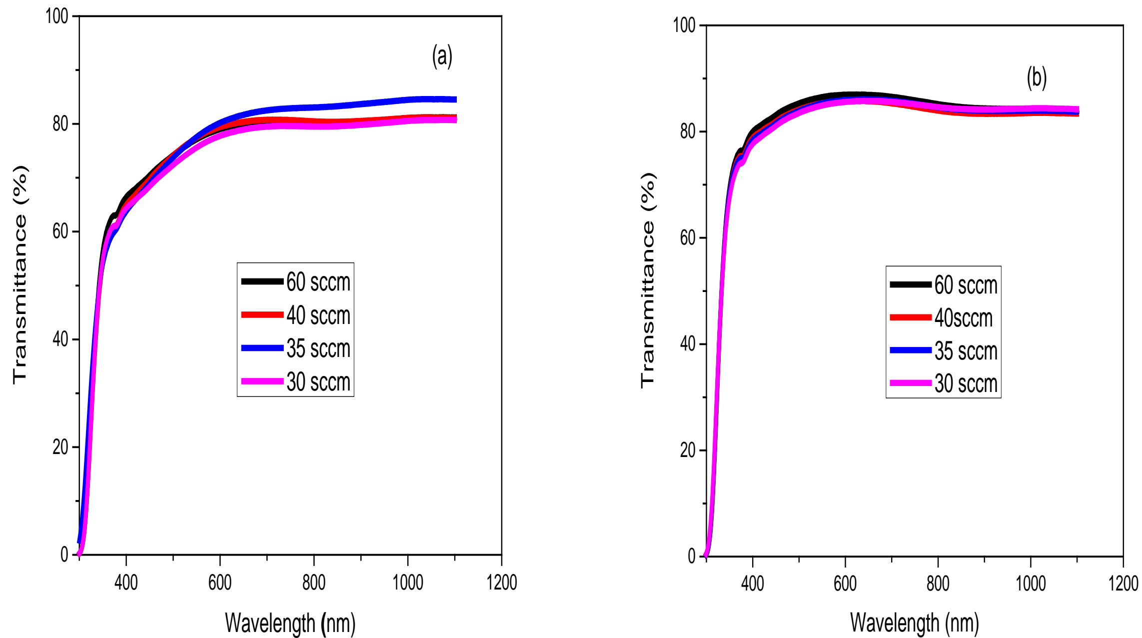

Fig 5. 14: Transmittance spectra for TiO_2:Ge (95:5) films with variation in argon flow rate for as-deposited (a) and annealed films (b)

This results contradicts with those of Bhardwaj *et al.*, (2018b), in which the film deposited at a higher argon flow rate recorded the lowest transparency. This was attributed to energetic ion bombardment experienced at high flow rates with eject more sputter material from the target resulting in a thicker film.

The films thickness was found by simulating experimental values for the transmittance using SCOUT software. It was noticed that there was minimal change in the thickness of the TiO_2:Ge films deposited at different argon flow rates. Table 5.3 below shows how the film thickness varied with argon flow rate for both as-deposited and annealed films as well as the yield rate for the as-grown films. It was noticed that the annealed films recorded less thickness compared to the as-deposited films. This could be attributed to improved crystallinity as discussed in section 5.4 subsection 5.4.1

Table 5. 3: Thickness and sputtering yield variation with argon flow rate for TiO_2:Ge (95:5) films

Argon flow rate (sccm) (±0.1)	**Thickness (nm) (as-deposited) (±0.1)**	**Thickness (nm) (annealed) (±0.1)**	**Sputtering Yield (nm/min) (as-deposited) (±0.1)**
30.0	63.7	38.2	1.1
35.0	61.8	36.4	1.0
40.0	59.3	34.3	1.0
60.0	57.5	28.7	1.0

Figures 5.15 (a) and (b) show the variation of thickness and sputtering yield with the argon flow rates. The change in the film thickness was almost insignificant as the argon flow rate was varied from 30-60 sccm. It was also observed that the sputtering yield remained almost constant for different argon flow rates. This suggests that variation of argon flow rate as a deposition parameter may have little or no significant change on the optical properties. Studies done by Martin *et al.*, (2001) showed that argon flow rate did not have specific influence on the optical and electrical properties of the deposited TiO_2 thin films.

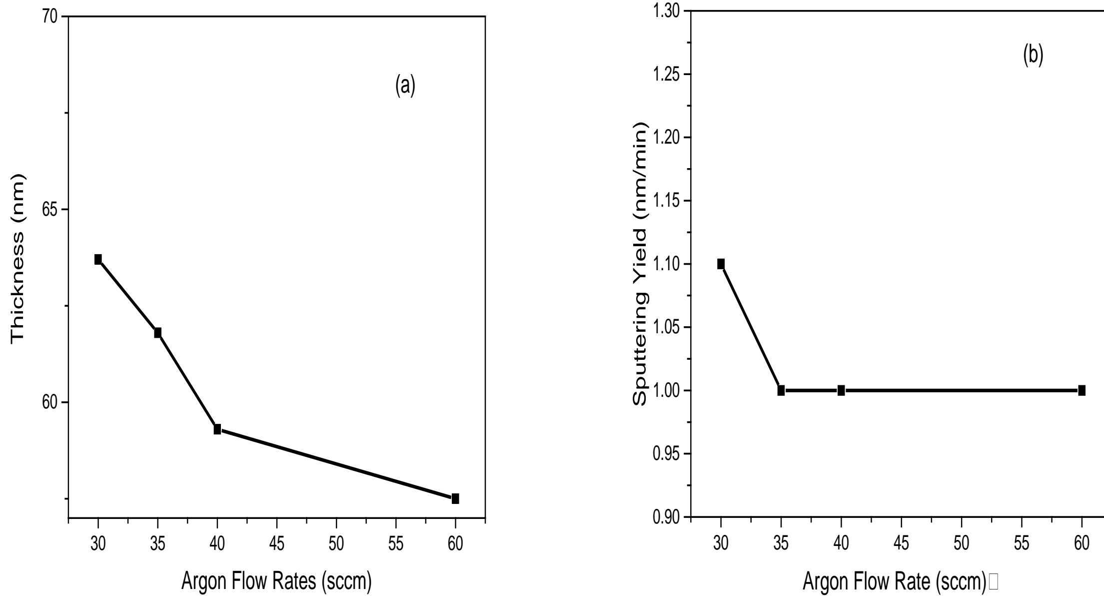

Fig 5. 15: Variation of thickness (a), and sputtering yield (b), with of argon flow rates for TiO_2:Ge (95:5) thin films.

5.6.2 Energy Bandgap

Figure 5.16 and table 5.4 show the energy bandgaps for as-deposited and annealed TiO_2:Ge thin films calculated using Tauc's equation. It was noticed that there was no significant change in the bandgap with variation of argon flow rate. However, annealing led to a decrease in the energy bandgap for the films. This was due to improved crystallinity for the films and possibly due to change from amorphous to anatase phase. The film deposited at 60 sccm showed the lowest bandgap (3.30 eV) while that deposited at 30 sccm recorded the highest (3.44 eV). Similar trend of results were reported by Bhardwaj *et al.*, (2018b).

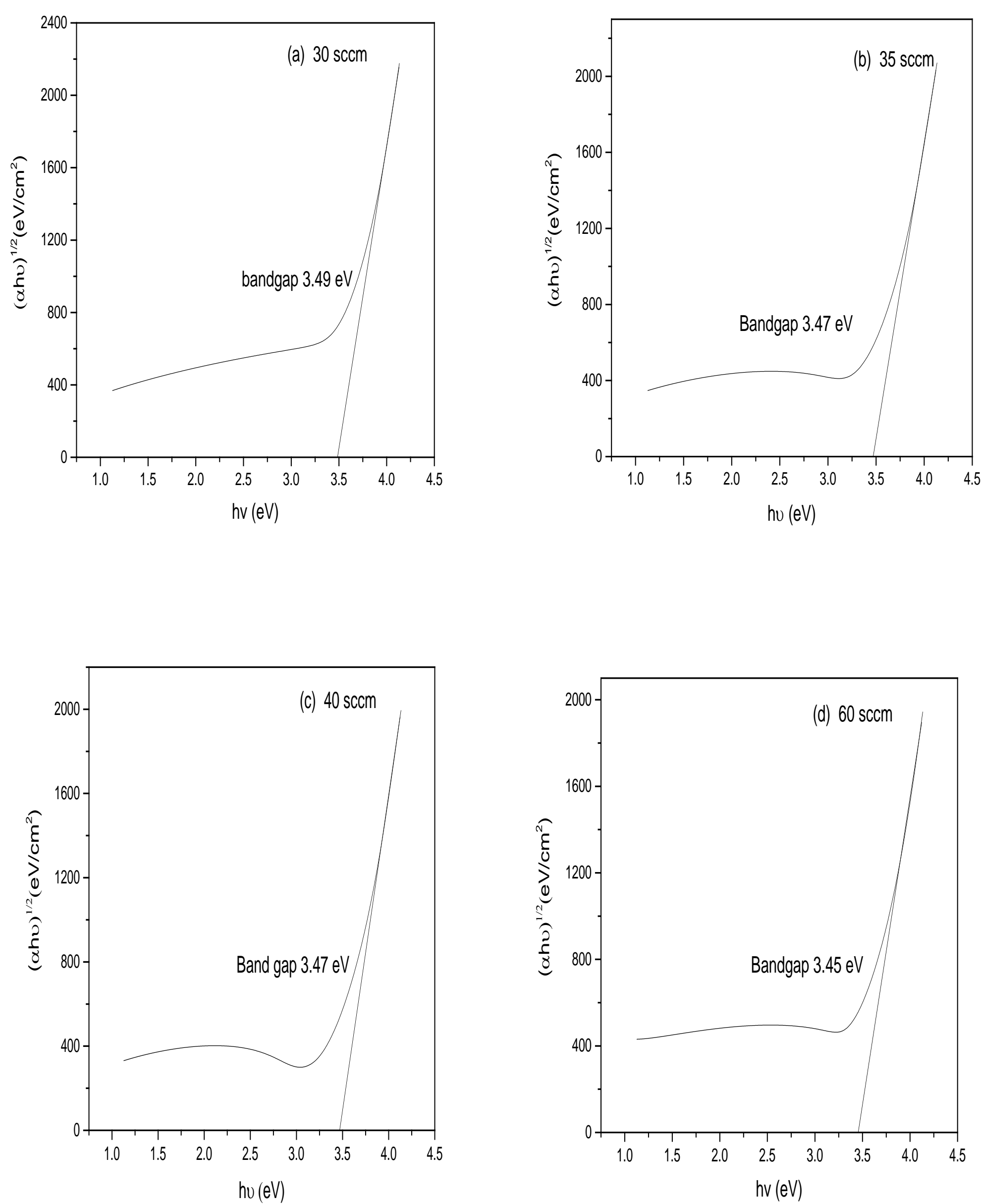

Fig 5. 16: The energy bandgap for as-deposited TiO_2:Ge (95:5) thin films deposited at 30 sccm (a), 35 sccm (b), 40 sccm (c) and 60 sccm (d).

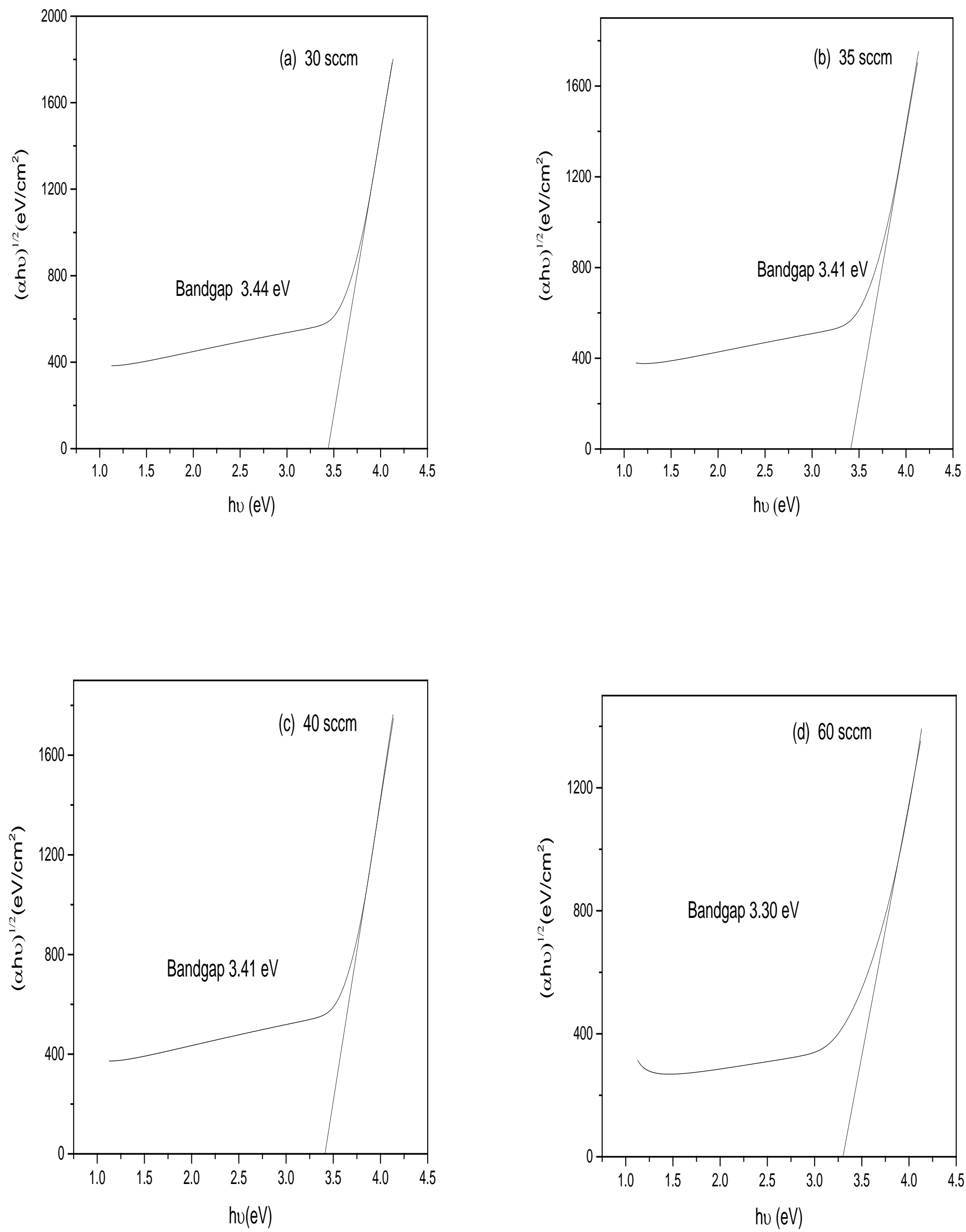

Fig 5. 17: Energy bandgap variation for annealed TiO_2;Ge films deposited at 30 sccm (a), 35 sccm (b), 40 sccm (c), and 60 sccm (d).

Table 5.4 shows a summary of the bandgap for as-deposited and annealed films for TiO_2:Ge thin films deposited at different argon flow rates.

Table 5. 4: The energy bandgap for the as-deposited and annealed TiO_2:Ge films deposited at various argon flow rates (30 sccm-60 sccm).

Argon flow rate (sccm) (±0.1)	**Bandgap (eV) (as-deposited) (±0.01)**	**Bandgap (eV) (annealed) (±0.01)**
30.0	3.49	3.44
35.0	3.47	3.41
40.0	3.47	3.41
60.0	3.45	3.30

5.6.3 Refractive Index

The refractive index of a thin film often differs from that of bulk material whereby, thin films show lower values whereas the refractive index of thicker films approaches the bulk value (Poruba *et al.*, 2000). The refractive index for TiO_2:Ge films deposited at various argon flow rates were as presented in figure 5.18. The results showed films of high refractive index in the visible region which tend to decrease with rise in wavelength. The high refractive index in the visible range (400 nm-700 nm) could be an indication that the films are absorbing in these regions. The lower energy associated with long wavelengths led to a decrease in refractive index. Similar trend was observed by Aksay and Altıokka,(2007). Refractive index increased with a decrease in argon flow rate. This could be attributed to high density associated with thicker films deposited at lower argon flow rates. A thicker layer is more compact and denser resulting to a higher refractive index.

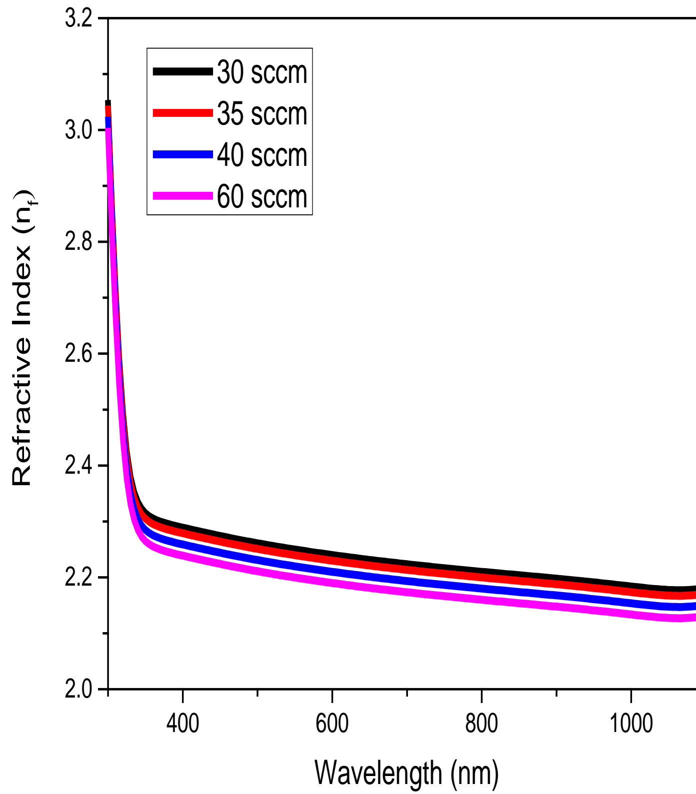

Fig 5. 18: Refractive index versus wavelength for TiO_2: Ge (95:5) thin films deposited at different argon flow rates.

5.7 Effect of Argon Flow Rate on Electrical Resistivity for TiO_2: Ge Thin Films

The measured values for resistivity and their corresponding conductivity for the as-deposited and annealed TiO_2: Ge thin films deposited at various argon flow rates were presented in table 5.5 and displayed in figure 5.19.

Table 5. 5: Resistivity and conductivity for as-deposited and annealed TiO_2: Ge films deposited at various argon flow rate.

Flow rates (sccm) (±0.1)	**Resistivity (10^{-2}) (Ω-cm) (as-deposited) (±0.01)**	**Resistivity (10^{-2}) (Ω-cm) (annealed) (±0.01)**	**Conductivity (siemen's cm^{-2}) (annealed) (±0.01)**
30.0	3.63	3.56	28.09
35.0	3.13	3.05	32.79
40.0	3.94	3.88	25.77
60.0	3.97	3.91	25.58

The results in table 5.5 shows that the resistivity for TiO_2: Ge thin films deposited at various argon flow rates have the same order of 10^{-2}. However, the films deposited at 60 sccm and 40 sccm showed a higher resistivity. This could be attributed to several factors including; stronger collision between the sputtered target atoms and argon atoms at high flow rate which may reduce the kinetic energy of the sputtered atoms limiting their deposition rate at the substrate. The resulting films may contain lots of grain boundaries which could also reduce the electron mobility in the crystal. Secondly, the increased argon flow rate introduces more argon atoms in the films which may result in structural defects in TiO_2: Ge film. These defects limit the electron mobility in the films. The film prepared at 35 sccm recorded the lowest resistivity and highest conductivity of 3.05×10^{-2} Ω-cm and 32.79 siemen's cm^{-2} respectively. Figure 5.19 below displays how resistivity varied with change in argon flow rates.

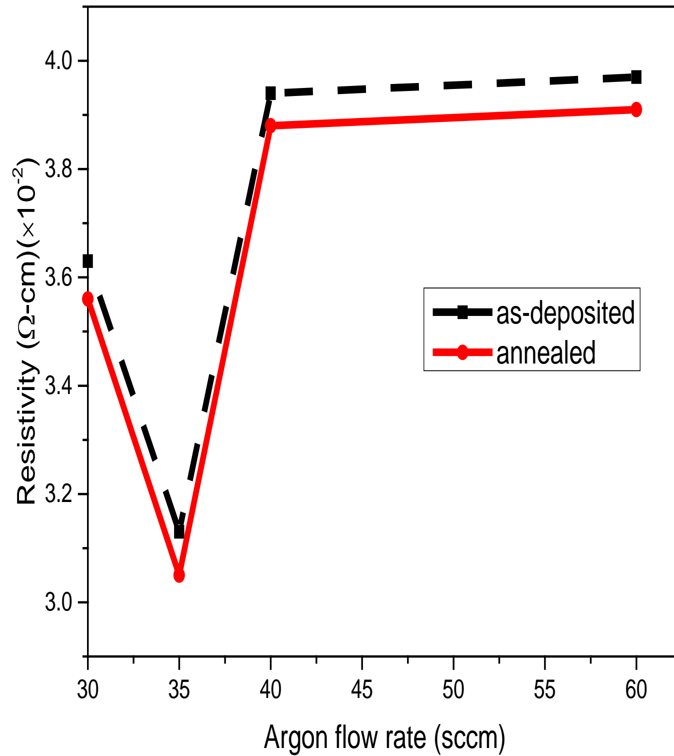

Fig 5. 19: Variation of resistivity for as-deposited and annealed TiO_2:Ge (95:5) thin films with argon flow rate.

Based on the discussion above, it can be concluded that the film deposited at sputtering power of 220 W gave a film with a better thickness (72.6 nm) compared to other powers. The film showed a good transmittance in the visible region and hence could be applied as a photoanode in DSSC. In addition the small bandgap (3.32 eV), a small resistivity (1.61×10^{-2} Ω-cm) and a good refractive index of 2.3 recorded by the film showed that the sputtering power of 220 W can be used as our optimum sputtering power in the deposition of different concentration TiO_2:Ge thin films.

Variation of argon flow rate had little influence on electrical and optical properties of TiO_2:Ge thin films. However, the film prepared at 35 sccm showed a better optical transmittance of >80% with a better film thickness (63.7 nm) compared to the films deposited at 30, 40, and 60 sccm. The

film also recorded a lower resistivity of 3.05×10^{-2} Ω-cm. Therefore, sputtering power of 220 W and the argon flow rate of 35 sccm were used as the optimum values for depositing different ratios of TiO_2: Ge thin films as discussed in the next section.

5.8 Elemental Analysis for Pure TiO_2 and TiO_2: Ge Thin Films

5.8.1 Energy Dispersive X-ray Fluorescence (EDXRF) for Pure TiO_2 and TiO_2: Ge Thin Films

EDXRF was conducted to confirm the elemental composition of pure TiO_2 and TiO_2: Ge films deposited on FTO glass substrates and annealed in air, Ar and N_2. Table 5.6 below shows the contents of Ti and Ge in parts per million obtained from EDXRF measurements.

Table 5. 6: Different percentages of TiO_2: Ge films annealed in air, Ar and N_2 and their contents in PPM.

TARGET (Ge % in TiO_2)	**Ti CONTENT IN PPM**			**Ge CONTENT IN PPM**		
	Air	**Ar**	**N_2**	**Air**	**Ar**	**N_2**
0%	43500	34000	42200	ND	ND	ND
5%	33600	30300	34700	15100	14900	19700
10%	24400	24000	27200	17100	21100	20400
15%	28500	21900	21000	21400	26900	24000

It is observed that the content of Ti in all the targets was higher than those of Ge. This was as expected since Ge was incorporated in small percentages in TiO_2 matrix. For pure TiO_2 film, Ge element was not detected (ND) indicating its absence. The content of Ge in PPM was observed to increase as its concentration in TiO_2 matrix increased from 5-15%.

Figure 5.20 shows the spectral analysis for pure TiO_2 and TiO_2: Ge (95:5) films annealed in air. From the figure 5.20 (a) a peak of interest was identified at 4.525 which correspond to Ti element. Other peaks also emerged at 3.4, 3.7 and 6.4 which correspond to Tin (Sn), Calcium (Ca) and Iron (Fe). These other elements are composed of chemical compounds of glass (Matjie *et al.*, 2008).

From figure 5.20 (b), a minor peak corresponding to Ge was identified at 9.8 confirming its presence.

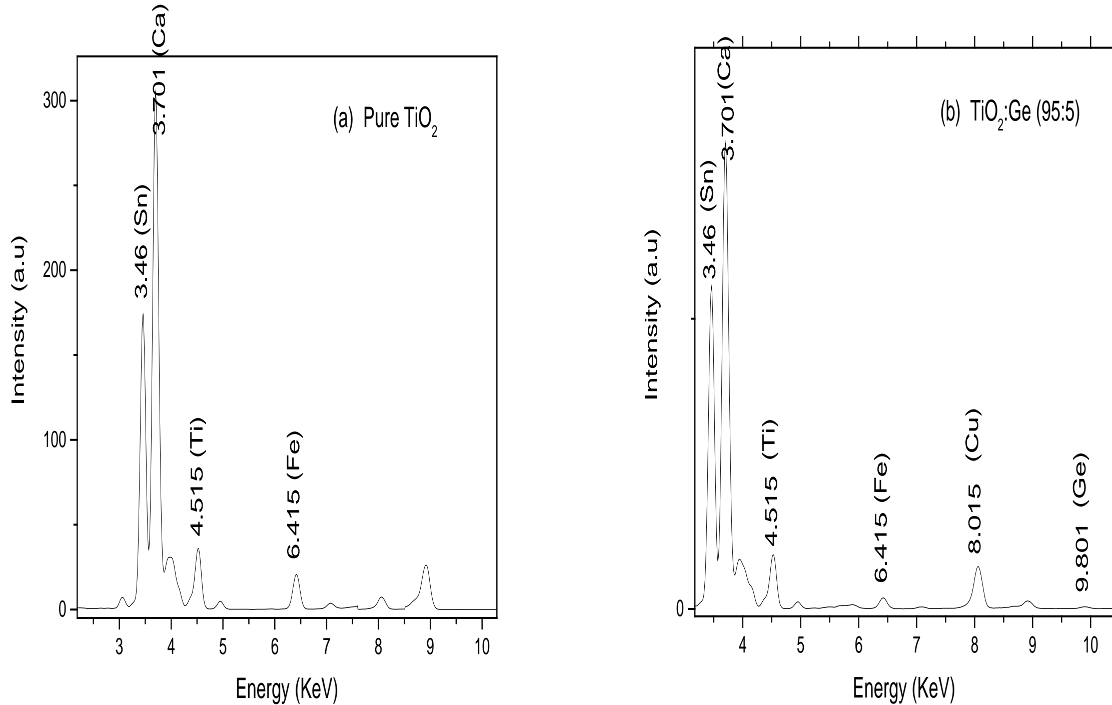

Fig 5. 20: EDXRF spectra for pure TiO_2 (a) and TiO_2:Ge (95:5) (b) thin films. The other composites films with Ge have a similar spectrum an in (b) above

5.9 Structural Analysis of TiO_2:Ge Thin Films

Figure 5.21 shows the X-Ray Diffraction patterns for pure TiO_2 and TiO_2:Ge composite thin films deposited on conducting glass substrates (FTO) at room temperature (23-25 °C). The films were then annealed in different ambient: nitrogen (N_2), argon (Ar) and air at 450 °C. The XRD patterns were compared with the Joint Committee on Powder Diffraction Standards (JCPDS) database card No.21-1272 for anatase and 21-1276 for rutile (Waita *et al.*, 2007). It was observed that all the films were crystalline and composed of a mixture of anatase and rutile phases irrespective of the annealing atmosphere. The rutile phase was observed at 27 ^{o} (110) plane in all films. Besides, a strong intensity peak corresponding to 38 ^{o} (004) planes is also found in all films and was attributed to the anatase phase. A smaller peak corresponding to anatase was also observed at 62 ^{o} (204). A

peak corresponding to Ge was observed at 24 º (111) in all TiO_2:Ge thin films. The presence of TiO_2 and Ge peaks confirmed that TiO_2:Ge film was indeed a composite. Similar observations were made by Chatterjee, (2008a) in his study on TiO_2:Ge nanocomposite material for photovoltaic application.

It was also observed that the peak along the 38 º (004) plane showed an increase in intensity with increase in Ge content. This could be due to increase in the crystallite sizes as shown in table 5.7. Also, the intensity for (110) plane for the rutile phase is higher for N_2 and Ar annealed films than those annealed in air. This suggests that oxygen reducing environment may facilitate the formation of rutile phase in TiO_2 films. Studies have confirmed that anatase phase has a good electron transport compared to rutile and brookite phases making it suitable for optoelectronic applications (Takahashi *et al.*, 2003). However, a mixture of anatase and rutile phases of TiO_2 exhibit an excellent photocatalytic activity (Castrejón-Sánchez *et al.*, 2014).

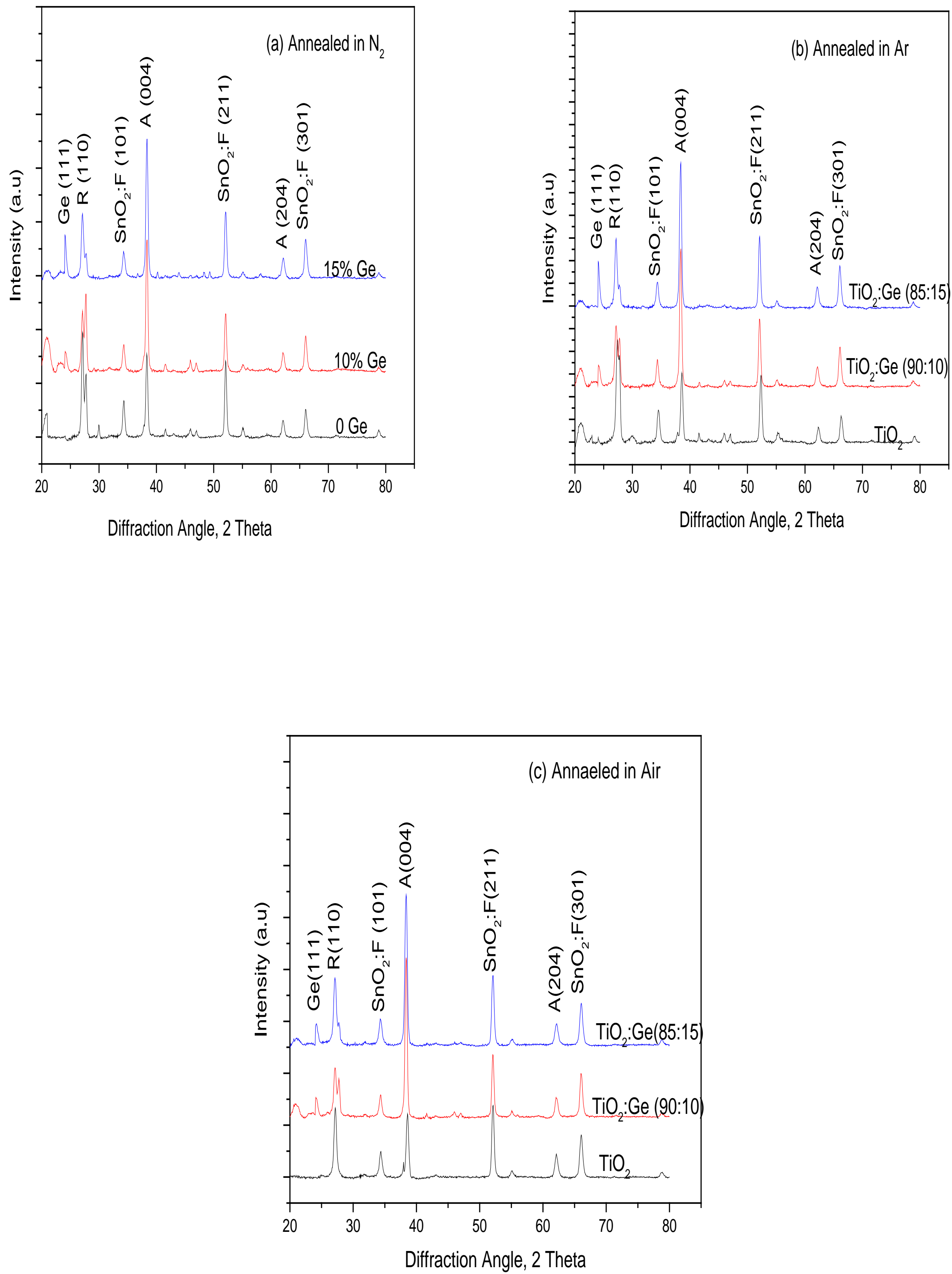

Fig 5. 21: XRD patterns for pure TiO_2 and TiO_2:Ge films annealed in (a) N_2, (b) Ar and (c) air

The XRD study showed that the intensities of the peaks for the films annealed in nitrogen and argon were higher compared to the films annealed in air. This suggested that these films were more crystalline. The findings in the current study agrees with those of Rahim *et al.*, (2017) who studied the effect of annealing gas on properties of TiO_2. The XRD analysis revealed that there could be a lot of structural changes associated with a specific heating atmosphere. However, the results contradicted with the observations made by Guillén and Herrero, (2007) who concluded that annealing atmosphere has no effect on the structural property of ITO films.

The XRD data was used to estimate the crystallite sizes for pure TiO_2 and TiO_2:Ge thin films using the Debye-Scherre's formula shown in equation 5.5 (Arunachalam *et al.*, 2015). The Full Width at Half Maximum (FWHM) values for the most pronounced peak (38° (004)) was calculated using equation 5.5.

$$D = \frac{K\lambda}{\beta COS\theta} \tag{5.5}$$

Where K=0.9 is the shape factor, λ is the wavelength used (0.15405), β is the full width at half maximum (FWHM) value and θ is the Braggs angle in radians.

Figure 5.22 shows the Gaussian fit on the experimental data along the 38° (004) orientation plane. The fit converged well, and the FWHM values for different compositional ratios of TiO_2:Ge thin films were obtained.

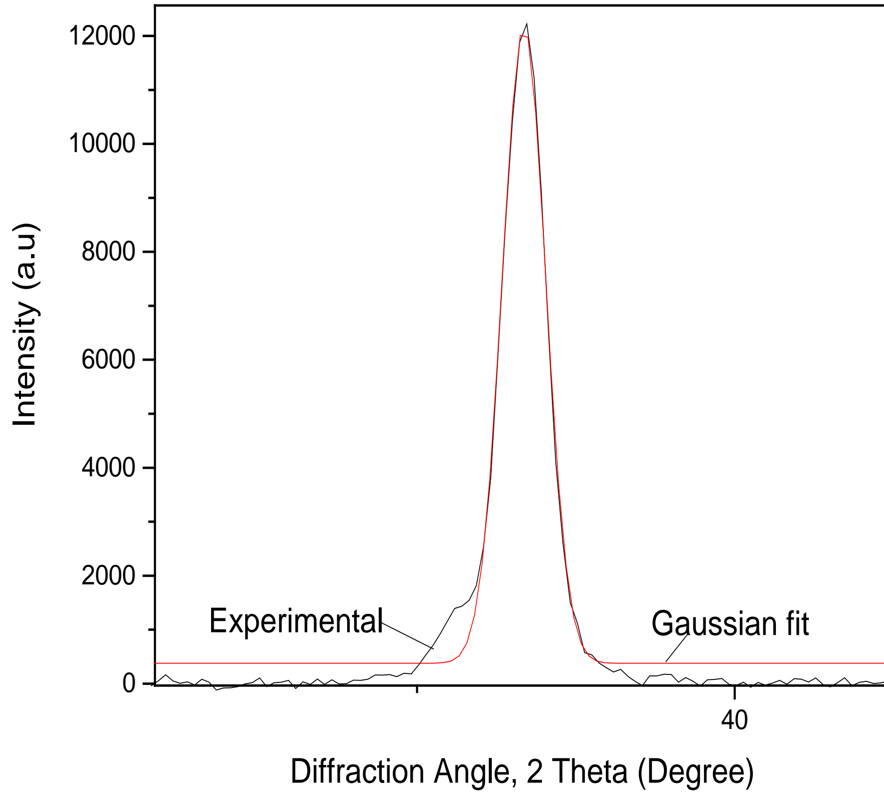

Fig 5. 22: Determination of FWHM for TiO_2:Ge (90:10) thin films using 38 º (004) peak

The crystallite sizes obtained using equation 5.5 were summarized as follows in table 5.7

Table 5. 7 : Crystallite sizes for the 38 º (004) peak of TiO_2: Ge films using Scherrer's formula

FILM	**Annealed in N_2 Crystallite size (nm) (±0.01)**	**Annealed Ar Crystallite size (nm) (±0.01)**	**Annealed in Air Crystallite size (nm) (±0.01)**
0% TiO_2: Ge	19.43	19.20	19.11
10% TiO_2: Ge	20.68	19.84	19.24
15% TiO_2: Ge	21.49	20.87	20.11

The crystallite sizes of the films increased with an increase in Ge concentration for all samples annealed in different atmosphere. The films annealed in N_2 showed bigger crystallite sizes than those annealed in air and Ar.

The density of defect in the crystal structure was also estimated using equation 5.6 (Arunachalam *et al.*, 2015).

$$\delta = \frac{1}{D^2} \tag{5.6}$$

The estimated values of dislocation defect levels in pure TiO_2 and TiO_2: Ge composites films with different concentrations of Ge and calcined in different atmospheres were summarized in table 5.8 below

Table 5. 8: The dislocation defect density for TiO_2: Ge films

Sample Ge concentration in TiO_2	**Annealed in N_2 Defect density (10^{-3}) (Å^{-2}) (±0.01)**	**Annealed in Air Defect density (10^{-3}) (Å^{-2}) (±0.01)**	**Annealed in Ar Defect density (10^{-3}) (Å^{-2}) (±0.01)**
0% Ge	2.71	2.74	2.65
10% Ge	2.34	2.70	2.54
15% Ge	2.17	2.47	2.30

It was observed that increase in the Ge concentration in TiO_2 resulted to a decrease in the defect density. This suggested improved crystallinity of the films (Arunachalam *et al.*, 2015).

5.10 Morphological Analysis for TiO_2: Ge Thin Films Annealed in Different Atmospheres

Figure 5.23 shows the SEM micrograph images of pure TiO_2 and TiO_2: Ge (85:15) films annealed in different atmospheres.

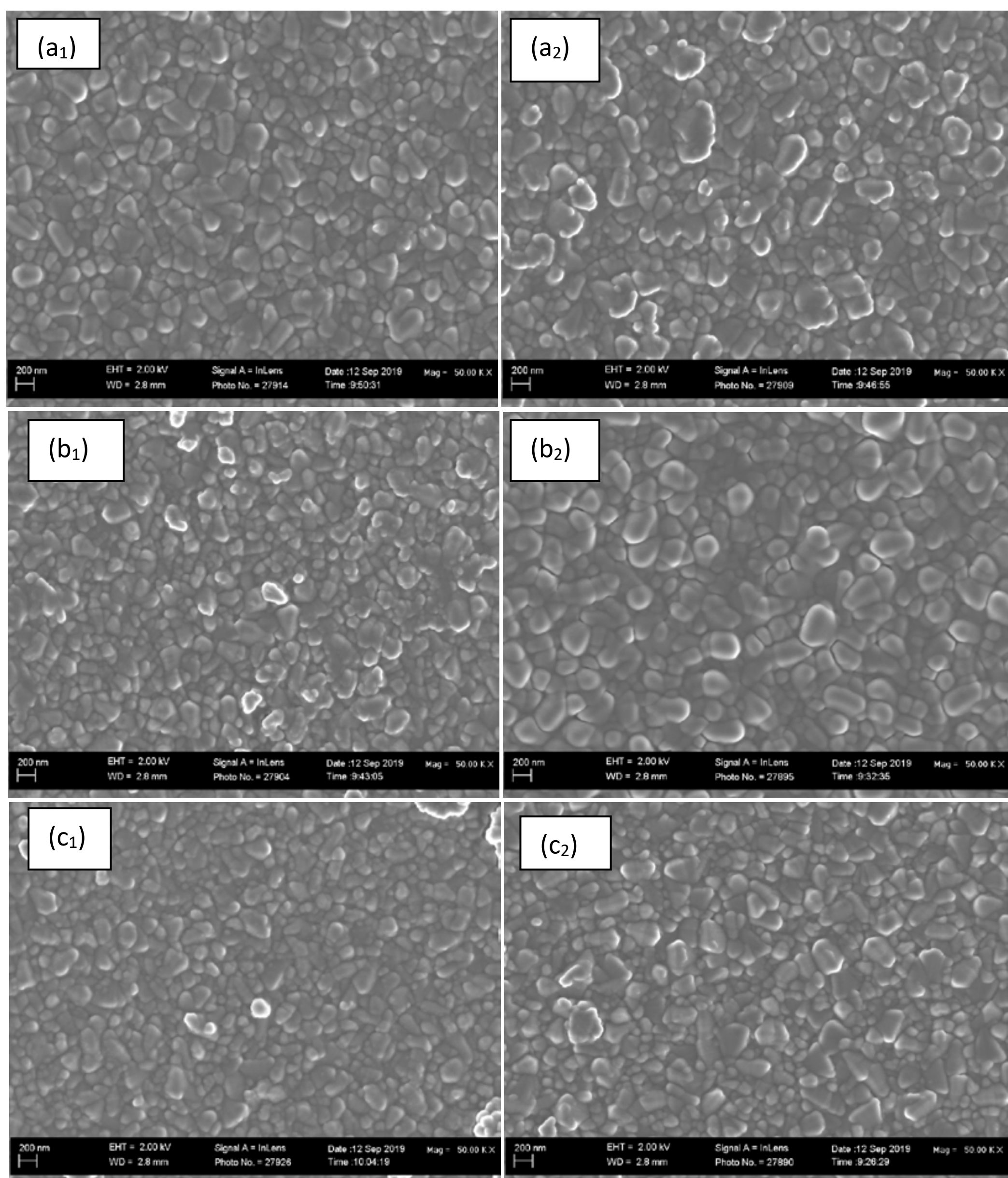

Fig 5. 23: The SEM micrographs images for pure TiO_2 and TiO_2: Ge (85:15) annealed in different atmospheres. Images a_1, b_1 and c_1 are for pure TiO_2 annealed in nitrogen, argon and air respectively while a_2, b_2 and c_2 are films for TiO_2:Ge annealed in nitrogen, argon and air respectively.

All the films showed a uniform structure without cracks or pinholes and well covered to the substrate. The homogenous property made the films suitable for use as a compact TiO_2 blocking layer in the fabrication of DSSC. Pure TiO_2 films annealed air, argon and nitrogen were mainly

composed of small spherical homogenous structure surfaces. The particle sizes of the films were approximated using image j software (Abràmoff *et al.*, 2004). It was observed that TiO_2: Ge (85:15) films (a_2, b_2, c_2) were composed of bigger particles compared to pure TiO_2 (a_1, b_1, c_1) in all samples. The films annealed in N_2 showed bigger particle sizes than those annealed in air and Ar. Table 5.9 summarizes the particle size of the films as approximated by image j software.

Table 5. 9: Particle sizes of pure TiO_2 and TiO_2: Ge (85:15) annealed in N_2, Ar and air

Film	**Annealed in N_2** Particle Size (nm) (±0.01)	**Annealed in Ar** Particle Size (nm) (±0.01)	**Annealed in Air** Particle Size (nm) (±0.01)
Pure TiO_2	33.69	32.10	30.83
TiO_2: Ge (85:15)	38.26	36.85	31.85

5.11 Effect of Ge Concentration and Annealing Ambient on Optical Properties for TiO_2: Ge thin Films

5.11.1 Transmittance

The measured transmittance of pure TiO_2 and TiO_2: Ge films with different concentration of Ge, and annealed in different atmospheres (air, nitrogen, and argon) were as shown in figure 5.24. Generally, all the films were transparent in the visible region. The transmission in the visible range decreased substantially at shorter wavelength (< 400 nm) near the ultraviolet region in all the films. This could be due to multiple reflections by the glass and films and also because of light absorption by the films and the glass (El-Raheem and Al-Baradi, 2013). Pure TiO_2 films showed the highest transmittance in all the films averaging about 78%, 88%, 80%, and 70% for as-grown films, those annealed in air, argon, and nitrogen respectively in wavelength 400-700 nm. An increase in Ge (from 5-15 %) concentration caused the transmittance to decrease by about 5-8%. This could be due to increase in the film surface roughness which promoted surface scattering (Yousif *et al.*, 2016). The SEM images in figure 5. 22 showed a mixture of big and small particle sizes of the films, an indication of increased surface roughness in the films. In addition, the variation in the film thicknesses also contributed to the difference in transmittances.

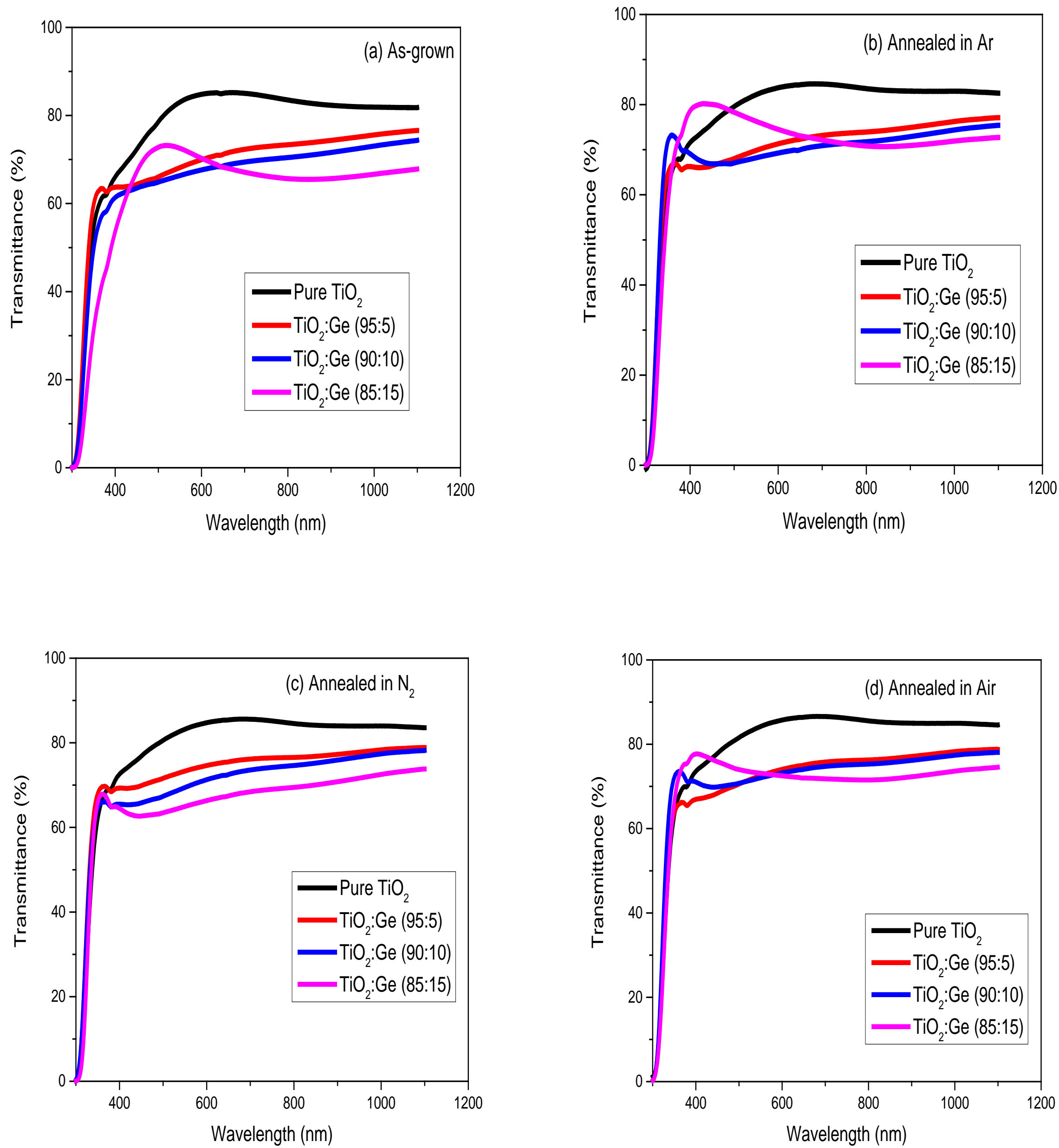

Fig 5. 24: Optical transmittance for TiO_2: Ge thin films for (a) as-deposited (b) annealed in Ar, (c) annealed N_2 and (d) annealed in air with different concentration of the Ge (from 0-15 %)

Figure 5.25 shows the transmittance in the UV-Vis region for pure TiO_2 and TiO_2: Ge films after annealing in air, N_2, and Ar atmospheres. There was not only a general increase in transmission in

visible region, but also an increase in the steepness for annealed films irrespective of the annealing atmosphere. The films annealed in air showed the highest transmittance averaging between 86%-72% for pure TiO_2 to TiO_2: Ge (85:15). The films annealed in nitrogen recorded the lowest transmittances averaging about 84%, 70% 68% and 67% for 0, 5, 10 and 15 % Ge concentration respectively. The lowest transmittance was associated with films colour change, which turned dark brown upon annealing in N_2. The dark brown colour suggests a higher absorption in visible region (Folger *et al.*, 2017). In addition, the films annealed in N_2 recorded the highest film thickness. This can be confirmed from the calculated crystallite sizes from XRD analysis which showed that the films annealed in N_2 were composed of bigger crystallite sizes suggesting large grain sizes.

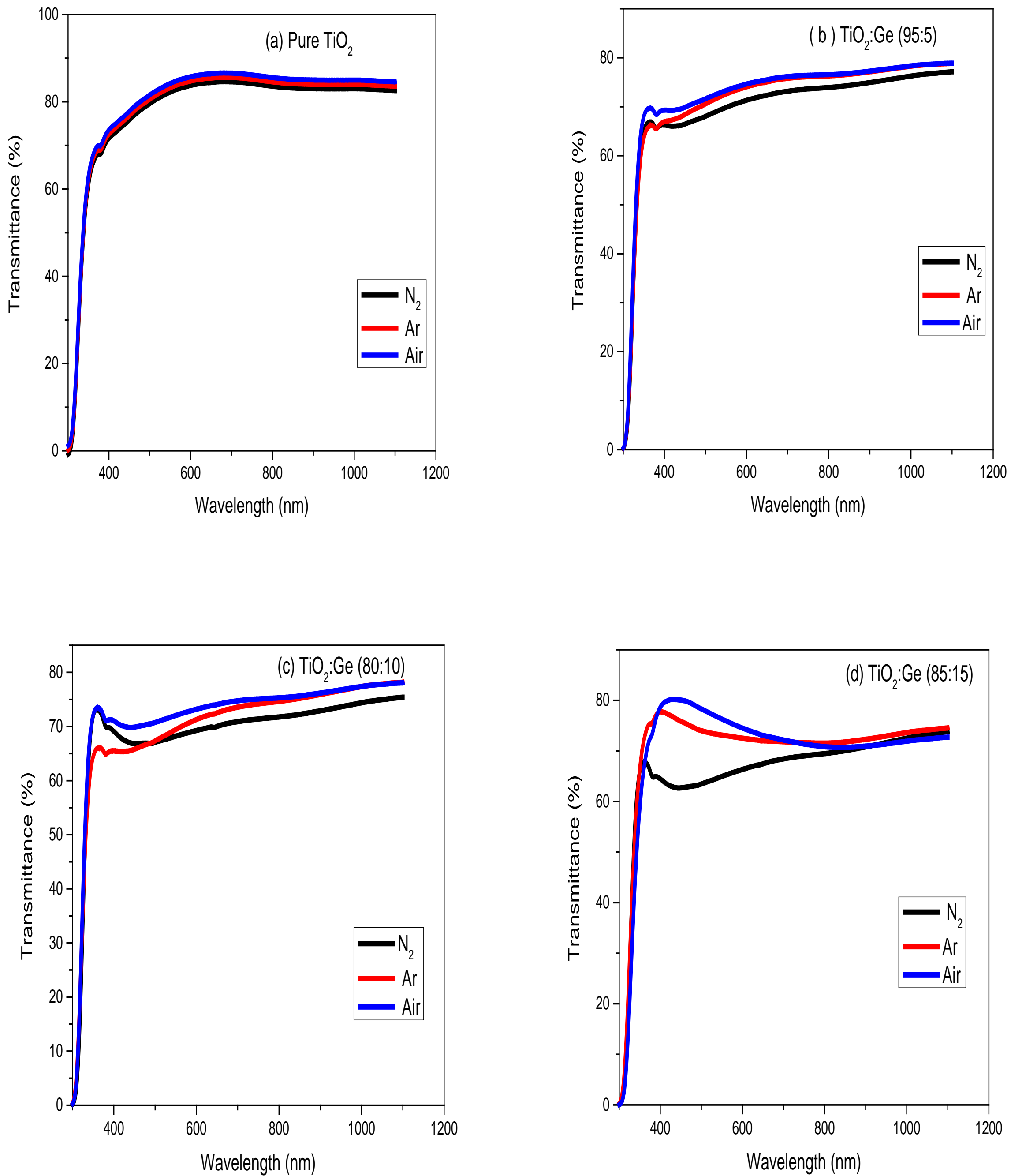

Fig 5. 25: Optical transmittance for pure TiO_2 (a), TiO_2:Ge (95:5) (b), TiO_2:Ge (90:10) (c), and TiO_2:Ge (85:15) (d) films annealed in different atmosphere (air, Ar, and N_2) at 450 ^{0}C.

The obtained film thicknesses from SCOUT showed that air annealed films were thinner than those calcined in argon and nitrogen. Table 5.10 below shows the variation of thickness of TiO_2: Ge films with the annealing atmosphere.

Table 5. 10 : Variation of thickness with Ge concentration in TiO_2: Ge films annealed in air, Ar, and N_2 gases.

Film	**Annealed in Air Thickness (nm)) ±0.1**	**Annealed in N_2 Thickness (nm) (±0.1)**	**Annealed in Ar Thickness (nm) ±0.1**
Pure TiO_2	84.6	101.4	87.3
TiO_2: Ge (95:5)	109.8	138.2	118.7
TiO_2: Ge (90:10)	140.2	174.2	151.8
TiO_2: Ge (85:15)	178.6	207.7	183.5

5.11.2 Energy Bandgap

Figure 5.26 below shows the relationship between $(\alpha h\nu)^{1/2}$ and hν (photon energy) for TiO_2: Ge films after annealing in air, nitrogen, and argon. It was observed that the energy bandgap estimated from the absorption coefficient varied depending on the concentration of Ge and annealing atmosphere. From the figure, pure TiO_2 films recorded the highest bandgap ranging between 3.62-3.66 eV for the films annealed in N_2, Ar, and air atmospheres. The bandgap values of TiO_2 films decreased with increase in Ge concentrations for all the films. The bandgap (E_g) decreased from 3.62-3.49, 3.60-3.45, and 3.64-3.57 eV for films annealed in argon, nitrogen, and air respectively, as Ge concentration increased from 0 to 15%. The reduction in energy bandgap could be due to the introduction of Ge impurity in either valence or conduction band of pure TiO_2 which created a tail energy levels that reduced bandgaps (Ayieko *et al.*, 2012). Also, this could be explained by large crystallite sizes recorded by TiO_2: Ge films as observed in the XRD results discussed above. The energy bandgap has an inverse relation to the size of the crystallite and therefore this implies that the decreasing bandgap was due to increase in Ge-TiO_2 crystallite sizes. Similar observations were made by Liu *et al.*, (2008a) in his study on the effect of doping nitrogen in the TiO_2 by radio

frequency sputtering. A reduction in the bandgap was also noted with increase in Ge concentration up to TiO_2:Ge (90:10), and thereafter decreased. This showed that 10% was the optimum content that could be added to TiO_2 to form a composite with the best properties.

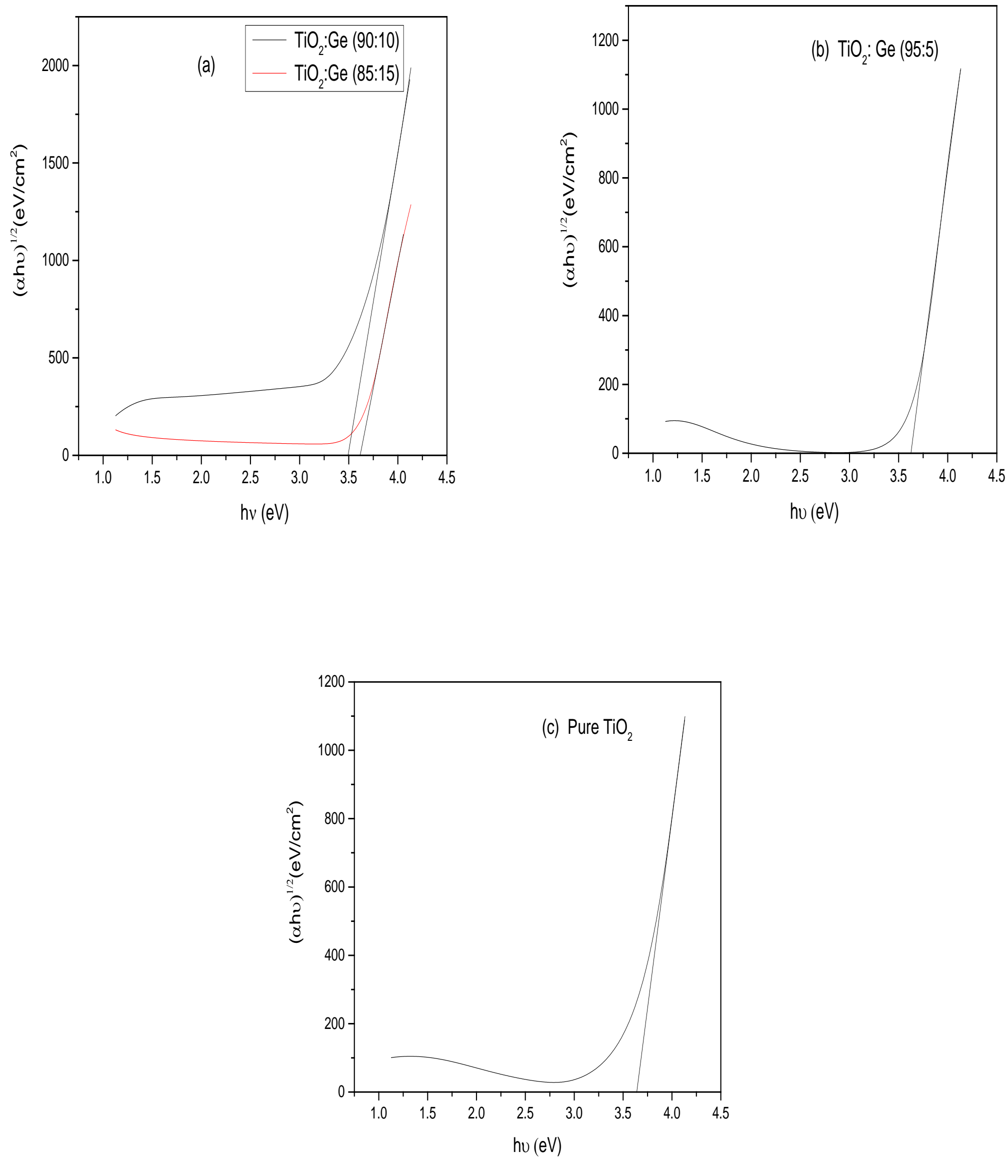

Fig 5. 26: Bandgap variation with Ge Concentration for TiO_2: Ge 85:15 and 90:10 (a), 95:5 (b) and pure TiO_2 (c) thin films annealed in argon.

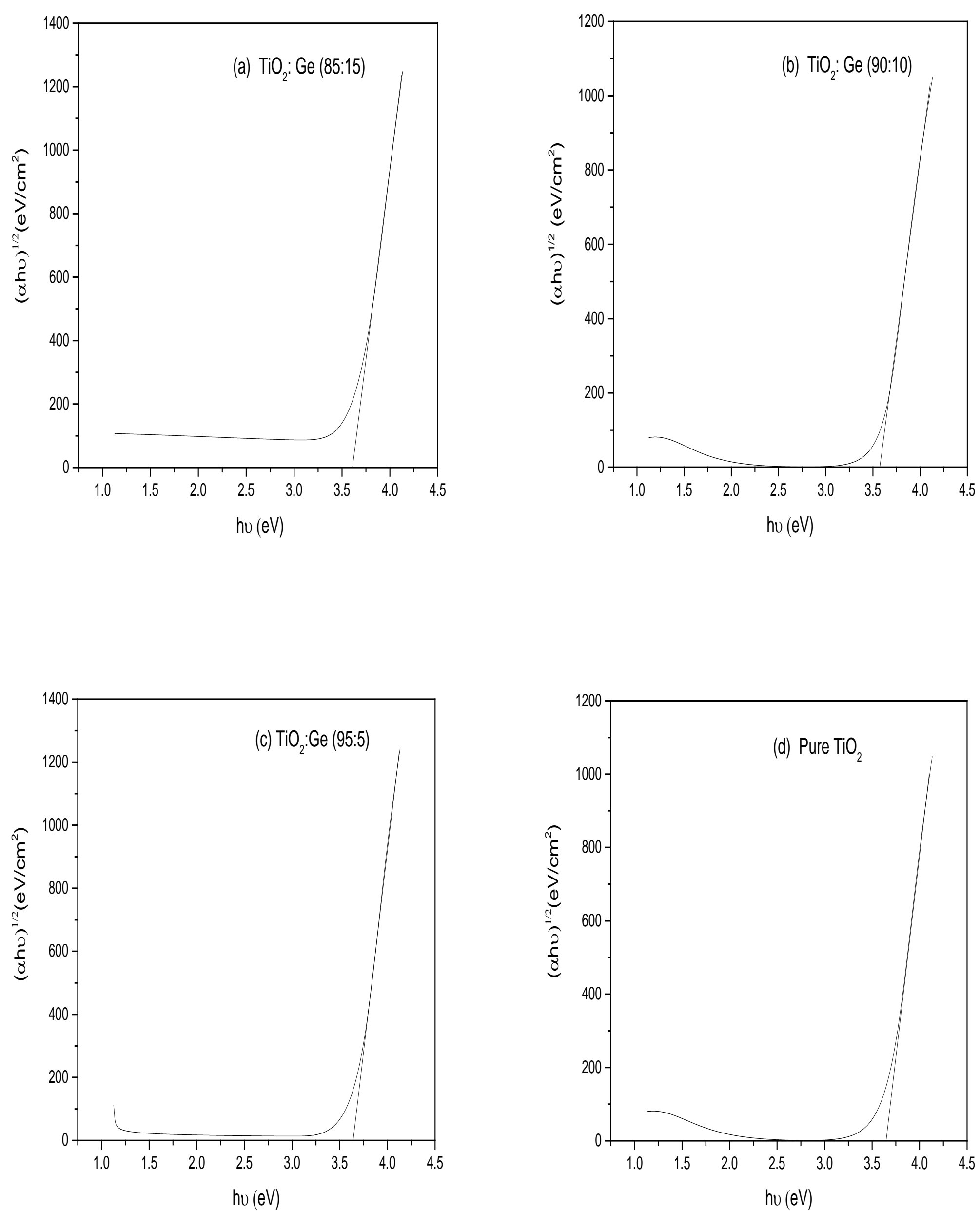

Fig 5. 27: Bandgap variation with Ge concentration for TiO_2: Ge films 85:15 (a), 90:10 (b), 95:5 (c) and pure TiO_2 (d) annealed in air

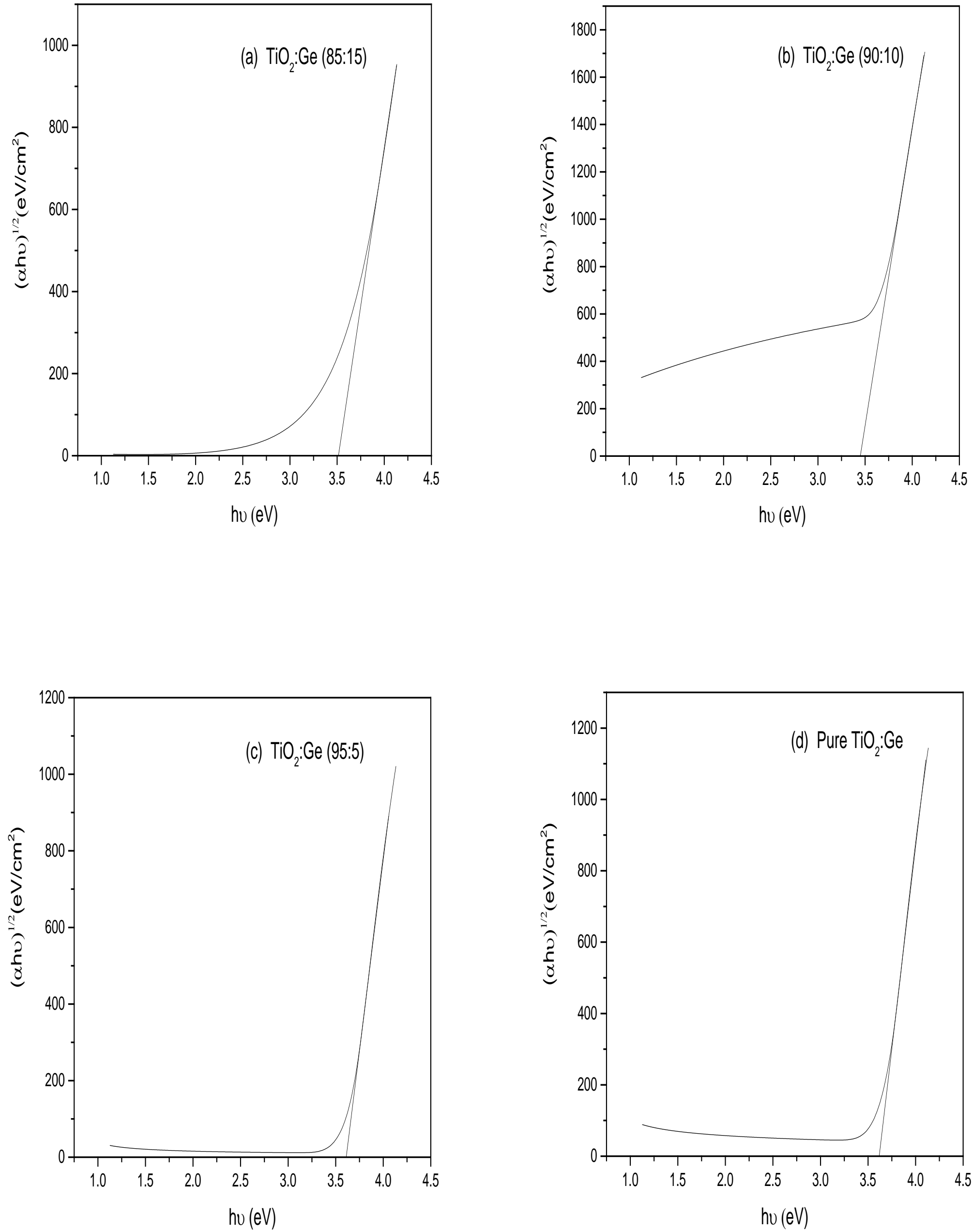

Fig 5. 28: Bandgap variation with Ge concentration for TiO_2: Ge films 85:15 (a), 90:10 (b), 95:5 (c) and pure TiO_2 (d) annealed in nitrogen

Table 5.11 and figure 5.31 below show how the bandgap varied with Ge concentration in TiO_2 for the as-grown films and those annealed in N_2, Ar and air. Comparing the different annealing

atmospheres, air annealed films recorded higher bandgap values averaging about 3.62 eV in comparison with Ar and N_2 annealed films which recorded a bandgap averaging about 3.59 eV and 3.55 eV respectively. Nitrogen annealed films showed the lowest bandgap values and this was attributed to improved crystallinity in the films during the annealing process and also associated with the development of oxygen vacancies in the TiO_2: Ge lattice. Oxygen vacancies created by annealing TiO_2: Ge films in argon and nitrogen lowered the bandgap and also facilitated phase transformation of TiO_2: Ge films. Air atmosphere was composed mainly of O_2 and therefore, the oxygen vacancies remained almost constant when the films were annealed in air hence a higher bandgap (Albetran *et al.*, 2016).

Table 5. 11 : Variation of the bandgap values with Ge concentration for films annealed in air, nitrogen, and argon atmosphere

Sample	**Annealed in Air** **Bandgap (eV) (±0.01)**	**Annealed in N_2** **Bandgap (eV) (±0.01)**	**Annealed in Ar** **Bandgap (eV) (±0.01)**
TiO_2: Ge (85:15)	3.60	3.51	3.60
TiO_2: Ge (90:10)	3.57	3.45	3.49
TiO_2: Ge (95:5)	3.64	3.60	3.62
Pure TiO_2	3.66	3.62	3.65

Figure 5.29 below shows the variation of pure TiO_2 and TiO_2: Ge bandgap with annealing atmosphere

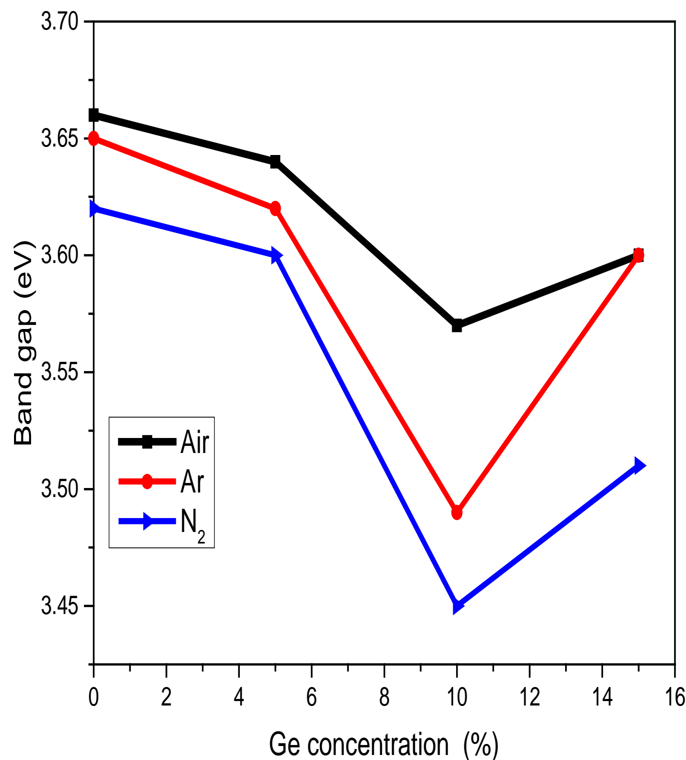

Fig 5. 29: Energy bandgap versus different ratios of TiO_2:Ge thin films annealed in N_2, Ar and air

5.11.3 Refractive Index

Figure 5.28 shows the refractive index for pure TiO_2 thin films annealed in air, N_2, and Ar atmospheres. From the line graphs, there was a generally high refractive index in the range 400-700 nm which is the visible region in all the films. However, the refractive index decreased with increase in the wavelength towards the infrared region of the solar spectrum, and this could be due to lower energy associated with longer wavelengths. The films annealed in N_2 gas showed the highest refractive index, followed by those annealed in Ar and air respectively. This variation could be attributed to the difference in the film density. TiO_2 films annealed in N_2 were denser than those annealed in Ar and air. A thick layer is more compact and denser hence an increase in refractive index.

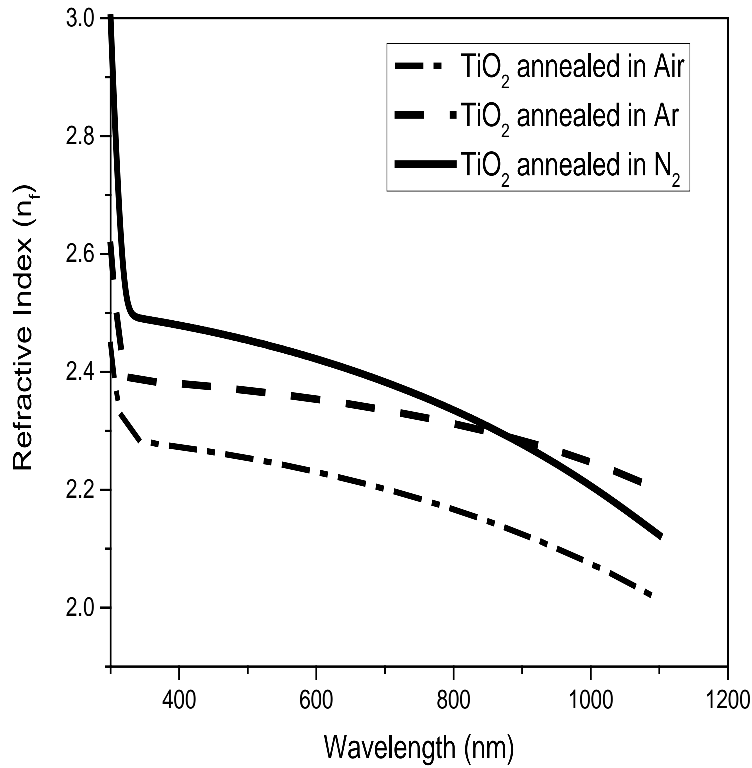

Fig 5. 30: Dependence of Refractive Index on annealing atmosphere for pure TiO_2 thin films

5.12 Effect of Ge Concentration in TiO_2 and Annealing Atmosphere on Electrical Resistivity of TiO_2: Ge Thin Films

The resistivity of pure TiO_2 and TiO_2: Ge thin films annealed in different atmospheres: air, N_2, and Ar was measured using a four-point probe method. Table 5.4 below summarizes the films resistivity for as-deposited and those annealed in ambient.

Table 5. 12: Resistivity variation for TiO_2: Ge annealed in a different atmosphere

Sample	**As-deposited** **Resistivity (Ω-cm) 10^{-2}**	**Annealed in Air** **Resistivity (Ω-cm) 10^{-2}**	**Annealed in Ar** **Resistivity (Ω-cm) 10^{-2}**	**Annealed in N_2** **Resistivity (Ω-cm) 10^{-2}**
Pure TiO_2	13.03	9.69	10.41	9.47
TiO_2: Ge (95:5)	6.99	6.80	6.91	5.05
TiO_2: Ge (90:10)	5.91	3.61	3.47	2.24
TiO_2:Ge (85:15)	6.11	5.92	4.67	4.15

From table 5.11 and figure 5.31, it was confirmed that there was a decrease in resistivity after annealing irrespective of the annealing atmosphere. It was also noted that the resistivity of the films decreased with increase in Ge concentrations. This could be due to the improvement of the films crystallinity (Tong *et al.*, 2011). The XRD results confirmed that indeed, there was an increase in crystallite sizes of the films after incorporating Ge in TiO_2 matrix. Increase in grain size resulted to a decrease in the grain boundaries which increased the flow of electrons hence a reduction in resistivity (Biju and Jain, 2008). The films annealed in nitrogen recorded the least resistivity compared to those annealed in air and argon. This could be attributed to the formation of additional oxygen vacancies upon annealing the films in N_2. These O_2 vacancies acted as donor centers for electrons hence resulting to a lower resistivity (Tong *et al.*, 2011).

Figure 5.31 below shows how the resistivity of different ratios for TiO_2: Ge thin films varies with annealing atmosphere.

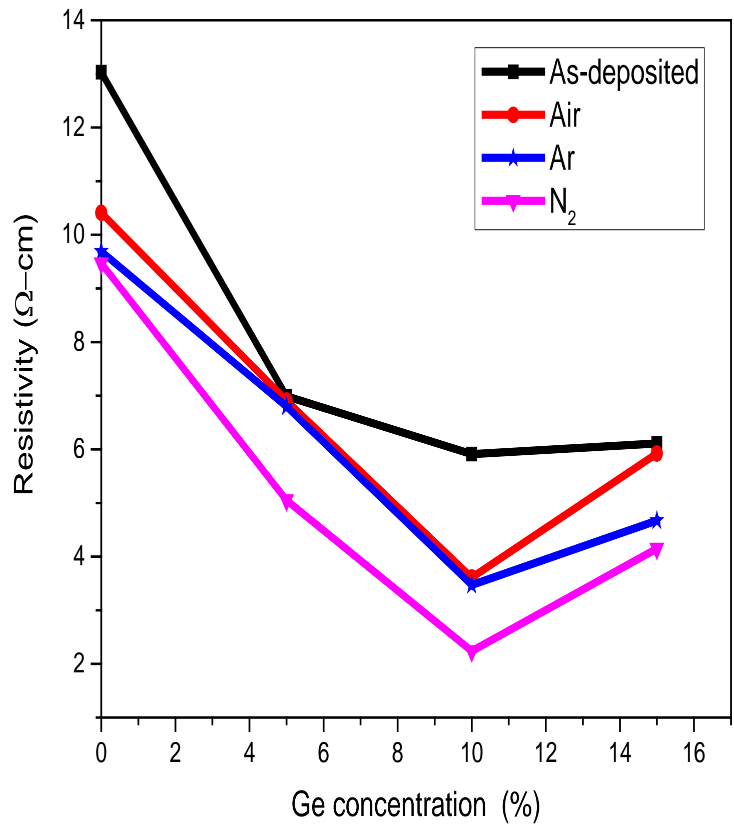

Fig 5. 31: Resistivity versus Ge concentration in TiO_2 for different annealing atmospheres

CHAPTER SIX

CONCLUSION AND RECOMMENDATION

6.1 Conclusion

Pure Titanium dioxide (TiO_2) and Titanium-Germanium (TiO_2: Ge) composite thin films were successfully prepared by rf magnetron sputtering technique. The sputtering power of 220 W and the argon flow rate of 35 sccm were used as the optimum deposition parameters for depositing different ratios of TiO_2: Ge films, which were later annealed in three different atmospheres; air, Ar, and N_2. Structural analysis from XRD confirmed that TiO_2:Ge films were a mixture of anatase and rutile phases irrespective of the annealing atmosphere. The rutile peaks were more pronounced in the films annealed in Ar and N_2 compared to those annealed in air. This suggested that oxygen reducing environment may facilitate the formation of rutile phase in TiO_2. The calculated crystallite sizes ranged between 19-21 nm. The SEM images revealed that films were crack-free and without pin-holes, with the films annealed in N_2 showing bigger particle sizes. Annealing the films in oxygen deficient atmosphere improved the structural and the morphological properties.

Different annealing atmospheres had a significant effect on the electrical and optical properties of TiO_2:Ge thin films. The films annealed in nitrogen recorded the best properties unlike those annealed in air and argon. Nitrogen annealed films recorded a lower bandgap and resistivity averaging about 3.55 eV and 5.23×10^{-2} Ω-cm respectively. This was attributed to formation of oxygen vacancies. Additionally, nitrogen annealed films showed the highest refractive index compared to air and argon annealed films. Generally, the films annealed in oxygen deficient environment (N_2) gave the best optical and electrical properties.

Introduction of Germanium element in TiO_2 lattice had a significant effect on the optical, electrical and structural properties for films. TiO_2 and TiO_2: Ge composite thin films were found to be generally transparent in the visible region. It was found that an increase in Ge content in TiO_2 matrix decreased both electrical and optical properties of TiO_2: Ge films. TiO_2: Ge ratio of 85:15 recorded the lowest transmittance average of 70% in wavelengths 400-700 nm. The bandgap decreased from 3.64 eV to 3.57 eV while the electrical resistivity decreased from 11.01×10^{-2} Ω-

cm to 2.24×10^{-2} Ω-cm. Structurally, from the XRD analysis, introduction of Ge in TiO_2 improved the crystallinity of the films. Generally, incorporation of Ge into TiO_2 matrix up to 10% improved the optical, electrical and structural properties of the films. It was confirmed that optimum percentage of Ge concentration that could be added to TiO_2 to give a film with the best properties was 10%.

Based on the properties of TiO_2:Ge thin films in this study, it was therefore recommended that TiO_2:Ge thin films with 10% Ge concentration and annealed in nitrogen atmosphere could be considered as a potential photoanode in Dye Sensitized Solar Cells applications.

6.2 Recommendation for Further work

- The effect of different annealing atmospheres (air, argon and nitrogen) on optical, electrical and structural properties for TiO_2:Ge thin films have been successfully studied in this work. Annealing the films in oxygen deficient atmospheres seem to have positively tuned the properties of the films. It is important to consider annealing the films in other oxygen deficient environments such as vacuum and hydrogen atmospheres and evaluate their properties.
- Introduction of Ge in TiO_2 lattice to form a composite led to a reduction in the film's resistivity. However there is need to study and understand the charge transport in TiO_2:Ge thin films it its photovoltaic application.
- The SEM study confirmed that all the annealed films were homogenous and well covered to the substrate. However, detailed analysis on how different annealing atmospheres affected the film roughness as well as the porosity was not done. Visual assessment of the images could not give adequate information on this. It is therefore important that AFM study is conducted on the films for better understanding.

References

Abràmoff, M. D., Magalhães, P. J., and Ram, S. J. (2004). Image processing with ImageJ. *Biophotonics international* **11**, 36–42.

Ahmad, M. S., Pandey, A., and Rahim, N. A. (2018). Effect of Germanium on the TiO_2 Photoanode for Dye Sensitized Solar Cell Applications. A Potential Sintering Aid. *IOP Conference Series: Materials Science and Engineering* **358**, 012015.

Aksay, S. and Altıokka, B. (2007). Effect of substrate temperature on some of the optical parameters of $CuInS_2$ films. *physica status solidi c* **4**, 585–588.

Albetran, H., O'Connor, B. H., and Low, I. M. (2016). Effect of calcination on band gaps for electrospun titania nanofibers heated in air–argon mixtures. *Materials & Design* **92**, 480–485.

Albu, S. P., Ghicov, A., Aldabergenova, S., Drechsel, P., LeClere, D., Thompson, G. E., Macak, J. M., and Schmuki, P. (2008). Formation of double-walled TiO_2 nanotubes and robust anatase membranes. *Advanced Materials* **20**, 4135–4139.

Albu, S. P., Tsuchiya, H., Fujimoto, S., and Schmuki, P. (2010). TiO_2 nanotubes–Annealing effects on detailed morphology and structure. *European Journal of Inorganic Chemistry* **2010**, 4351–4356.

Al-Sayyed, G., D'Oliveira, J.-C., and Pichat, P. (1991). Semiconductor-sensitized photodegradation of 4-chlorophenol in water. *Journal of Photochemistry and Photobiology A: Chemistry* **58**, 99–114.

Aly, S. A. and Akl, A. A. (2015). Influence of film thickness on optical absorption and energy gap of thermally evaporated CdS0. 1Se0. 9 thin films. *Chalcogenide Letters* **12**, 489–496.

Amtout, A. and Leonelli, R. (1995). Optical properties of rutile near its fundamental band gap. *Physical Review B* **51**, 6842.

Anwar, T., Li, W., Hussain, N., Chen, W., Sagar, R. U. R., and Tongxiang, L. (2016). Effect of annealing atmosphere induced crystallite size changes on the electrochemical properties of TiO_2 nanotubes arrays. *Journal of Electrical Engineering* **4**, 43–51.

Aourag, H., Hammadi, M., and Khelifa, B. (1993). Correlation between substitution and interstitial doping in ZnxHg1- xTe. *Materials chemistry and physics* **33**, 197–203.

Arunachalam, A., Dhanapandian, S., Manoharan, C., and Sivakumar, G. (2015). Physical properties of Zn doped TiO_2 thin films with spray pyrolysis technique and its effects in antibacterial activity. *Spectrochimica Acta Part A: Molecular and Biomolecular Spectroscopy* **138**, 105–112.

Ayieko, C. O., Musembi, R. J., Waita, S. M., Aduda, B. O., and Jain, P. K. (2012). Structural and optical characterization of nitrogen-doped TiO_2 thin films deposited by spray pyrolysis on fluorine doped tin oxide (FTO) coated glass slides. *International Journal of Energy Engineering* **2**, 67–72.

Bhardwaj, S., Basumatary, P., and Agarwal, P. (2018). Influence of argon flow rate on structural and optical properties of TiO_2 thin films deposited by RF sputtering. *In* "AIP Conference Proceedings," Vol. 1953, pp100043. AIP Publishing LLC.

Biju, K. P. and Jain, M. K. (2008). Effect of crystallization on humidity sensing properties of sol–gel derived nanocrystalline TiO_2 thin films. *Thin Solid Films* **516**, 2175–2180.

Boccuzzi, F., Chiorino, A., Manzoli, M., Lu, P., Akita, T., Ichikawa, S., and Haruta, M. (2001). Au/TiO_2 nanosized samples: A catalytic, TEM, and FTIR study of the effect of calcination temperature on the CO oxidation. *Journal of Catalysis* **202**, 256–267.

Brennan, K. F. (1999). "The physics of semiconductors: with applications to optoelectronic devices." Cambridge university press.

Campbell, S. A., Kim, H.-S., Gilmer, D. C., He, B., Ma, T., and Gladfelter, W. L. (1999). Titanium dioxide (TiO_2)-based gate insulators. *IBM journal of research and development* **43**, 383–392.

Carmichael, P., Hazafy, D., Bhachu, D. S., Mills, A., Darr, J. A., and Parkin, I. P. (2013). Atmospheric pressure chemical vapour deposition of boron doped titanium dioxide for photocatalytic water reduction and oxidation. *Physical Chemistry Chemical Physics* **15**, 16788–16794.

Carneiro, J. O., Teixeira, V., Portinha, A., Dupak, L., Magalhaes, A., and Coutinho, P. (2005). Study of the deposition parameters and Fe-dopant effect in the photocatalytic activity of TiO_2 films prepared by dc reactive magnetron sputtering. *Vacuum* **78**, 37–46.

Carp, O., Huisman, C. L., and Reller, A. (2004). Photoinduced reactivity of titanium dioxide. *Progress in solid state chemistry* **32**, 33–177.

Castrejón-Sánchez, V. H., Camps, E., and Camacho-López, M. (2014). Quantification of phase content in TiO_2 thin films by Raman spectroscopy. *Superficies y vacío* **27**, 88–92.

Chapman, B. N. (1980). "Glow discharge processes: sputtering and plasma etching." Wiley.

Chatterjee, S. (2008a). Titania–germanium nanocomposite as a photovoltaic material. *Solar energy* **82**, 95–99.

Chatterjee, S. (2008b). Titania–germanium nanocomposite as a thermoelectric material. *Materials Letters* **62**, 707–710.

Chatterjee, S. and Chatterjee, A. (2008). Optoelectronic properties of Ge-doped TiO_2 nanoparticles. *Japanese Journal of Applied Physics* **47**, 1136.

Chatterjee, S., Goyal, A., and Shah, S. I. (2006). Inorganic nanocomposites for the next generation photovoltaics. *Materials Letters* **60**, 3541–3543.

Chen, H.-L., Lu, Y.-M., and Hwang, W.-S. (2005). Characterization of sputtered NiO thin films. *Surface and Coatings Technology* **198**, 138–142.

Chen, X., Liu, L., Peter, Y. Y., and Mao, S. S. (2011). Increasing solar absorption for photocatalysis with black hydrogenated titanium dioxide nanocrystals. *Science* **331**, 746–750.

Choi, W., Termin, A., and Hoffmann, M. R. (1994a). The role of metal ion dopants in quantum-sized TiO_2: correlation between photoreactivity and charge carrier recombination dynamics. *The Journal of Physical Chemistry* **98**, 13669–13679.

Choi, W., Termin, A., and Hoffmann, M. R. (1994b). The role of metal ion dopants in quantum-sized TiO_2: correlation between photoreactivity and charge carrier recombination dynamics. *The Journal of Physical Chemistry* **98**, 13669–13679.

Choi, W., Termin, A., and Hoffmann, M. R. (1994c). Effects of metal-ion dopants on the photocatalytic reactivity of quantum-sized TiO_2 particles. *Angewandte Chemie International Edition in English* **33**, 1091–1092.

Chopra, K. L., Paulson, P. D., and Dutta, V. (2004). Thin-film solar cells: an overview. *Progress in Photovoltaics: Research and applications* **12**, 69–92.

DeLoach, J. D., Scarel, G., and Aita, C. R. (1999). Correlation between titania film structure and near ultraviolet optical absorption. *Journal of applied physics* **85**, 2377–2384.

Devi, L. G. and Kumar, S. G. (2011). Strategies developed on the modification of titania for visible light response with enhanced interfacial charge transfer process: an overview. *Open Chemistry* **9**, 959–961.

Dholam, R., Patel, N., Adami, M., and Miotello, A. (2009). Hydrogen production by photocatalytic water-splitting using Cr-or Fe-doped TiO_2 composite thin films photocatalyst. *International Journal of Hydrogen Energy* **34**, 5337–5346.

Diaz-Angulo, J., Arce-Sarria, A., Mueses, M., Hernandez-Ramirez, A., and Machuca-Martinez, F. (2019). Analysis of two dye-sensitized methods for improving the sunlight absorption of TiO_2 using CPC photoreactor at pilot scale. *Materials Science in Semiconductor Processing* **103**, 104640.

Dolgonos, A., Mason, T. O., and Poeppelmeier, K. R. (2016). Direct optical band gap measurement in polycrystalline semiconductors: A critical look at the Tauc method. *Journal of solid state chemistry* **240**, 43–48.

Domtau, D. L., Simiyu, J., Ayieta, E. O., Muthoka, B., and Mwabora, J. M. (2016). Optical and electrical properties dependence on thickness of screen-Printed TiO_2 thin films. *journal of Materials Physics and Chemistry* **4**, 1–3.

Eaglesham, D. J. and Cerullo, M. (1990). Dislocation-free stranski-krastanow growth of Ge on Si (100). *Physical review letters* **64**, 1943.

Eckortova, L. (1977). Physics of Thin Films Plenum Press. *New York and London*.

Eiamchai, P., Chindaudom, P., Pokaipisit, A., and Limsuwan, P. (2009). A spectroscopic ellipsometry study of TiO_2 thin films prepared by ion-assisted electron-beam evaporation. *Current Applied Physics* **9**, 707–712.

Einollahzadeh-Samadi, M. and Dariani, R. S. (2013). Effect of substrate temperature and deposition rate on the morphology and optical properties of Ti films. *Applied Surface Science* **280**, 263–267.

El-Raheem, M. A. and Al-Baradi, A. M. (2013). Optical properties of as-deposited TiO_2 thin films prepared by DC sputtering technique. *International Journal of Physical Sciences* **8**, 1570–1580.

Folger, A., Kalb, J., Schmidt-Mende, L., and Scheu, C. (2017). Tuning the Electronic Conductivity in Hydrothermally Grown Rutile TiO_2 Nanowires: Effect of Heat Treatment in Different Environments. *Nanomaterials* **7**, 289.

Gamboa, J. A. and Pasquevich, D. M. (1992). Effect of Chlorine Atmosphere on the Anatase-Rutile Transformation. *J American Ceramic Society* **75**, 2934–2938.

Geraki, K., Farquharson, M. J., and Bradley, D. A. (2003). X-ray fluorescence and energy dispersive x-ray diffraction for the quantification of elemental concentrations in breast tissue. *Phys. Med. Biol.* **49**, 99–110.

Ghicov, A., Tsuchiya, H., Macak, J. M., and Schmuki, P. (2006). Annealing effects on the photoresponse of TiO_2 nanotubes. *physica status solidi (a)* **203**, R28–R30.

Goh, E. S., Chen, T. P., Sun, C. Q., and Liu, Y. C. (2010). Thickness effect on the band gap and optical properties of germanium thin films. *Journal of Applied Physics* **107**, 024305.

Green, M. A. (2002). Third generation photovoltaics: solar cells for 2020 and beyond. *Physica E: Low-dimensional Systems and Nanostructures* **14**, 65–70.

Guillén, C. and Herrero, J. (2007). Structure, optical, and electrical properties of indium tin oxide thin films prepared by sputtering at room temperature and annealed in air or nitrogen. *Journal of Applied Physics* **101**, 073514.

Hamad, S., Catlow, C. R. A., Woodley, S. M., Lago, S., and Mejías, J. A. (2005). Structure and Stability of Small TiO_2 Nanoparticles. *J. Phys. Chem. B* **109**, 15741–15748.

Hasan, M. M., Haseeb, A., Saidur, R., and Masjuki, H. H. (2008). Effects of annealing treatment on optical properties of anatase TiO_2 thin films. *International Journal of Chemical and Biological Engineering* **1**, 92–96.

Huang, J.-H. and Wong, M.-S. (2011). Structures and properties of titania thin films annealed under different atmosphere. *Thin Solid Films* **520**, 1379–1384.

Hyam, R. S., Lee, J., Cho, E., Khim, J., and Lee, H. (2012). Effect of annealing environments on self-organized TiO_2 nanotubes for efficient photocatalytic applications. *Journal of nanoscience and nanotechnology* **12**, 8908–8912.

Ilican, S., Caglar, M., and Caglar, Y. (2007). Determination of the thickness and optical constants of transparent indium-doped ZnO thin films by the envelope method. *Materials Science-Poland* **25**, 709–718.

Irie, H., Watanabe, Y., and Hashimoto, K. (2003). Carbon-doped anatase TiO_2 powders as a visible-light sensitive photocatalyst. *Chemistry Letters* **32**, 772–773.

Jagadale, T. C., Takale, S. P., Sonawane, R. S., Joshi, H. M., Patil, S. I., Kale, B. B., and Ogale, S. B. (2008). N-doped TiO_2 nanoparticle based visible light photocatalyst by modified peroxide sol- gel method. *The Journal of Physical Chemistry C* **112**, 14595–14602.

Jang, S.-R., Vittal, R., and Kim, K.-J. (2004). Incorporation of Functionalized Single-Wall Carbon Nanotubes in Dye-Sensitized TiO_2 Solar Cells. *Langmuir* **20**, 9807–9810.

Jeyachandran, Y. L., Karunagaran, B., Narayandass, S. K., Mangalaraj, D., Jenkins, T. E., and Martin, P. J. (2006). Properties of titanium thin films deposited by dc magnetron sputtering. *Materials Science and Engineering: A* **431**, 277–284.

Jeyachandran, Y. L., Narayandass, S. K., Mangalaraj, D., Areva, S., and Mielczarski, J. A. (2007). Properties of titanium nitride films prepared by direct current magnetron sputtering. *Materials Science and Engineering: A* **445**, 223–236.

Jian, X., Jiang, M., Zhou, Z., Zeng, Q., Lu, J., Wang, D., Zhu, J., Gou, J., Wang, Y., and Hui, D. (2012). Gas-induced formation of Cu nanoparticle as catalyst for high-purity straight and helical carbon nanofibers. *Acs Nano* **6**, 8611–8619.

Kang, T.-S., Smith, A. P., Taylor, B. E., and Durstock, M. F. (2009). Fabrication of highly-ordered TiO_2 nanotube arrays and their use in dye-sensitized solar cells. *Nano letters* **9**, 601–606.

Kern, W. (2012). “Thin film processes II.” Elsevier.

Khan, A. F., Mehmood, M., Ali, T., and Fayaz, H. (2013). Structural and optical studies of nanostructured TiO_2–Ge multi-layer thin films. *Thin Solid Films* **536**, 220–228.

Khojier, K., Savaloni, H., Shokrai, E., Dehghani, Z., and Dehnavi, N. (2013). Influence of argon gas flow on mechanical and electrical properties of sputtered titanium nitride thin films. *J Theor Appl Phys* **7**, 37.

Kim, H., Gilmore, C. M., Piqué, A., Horwitz, J. S., Mattoussi, H., Murata, H., Kafafi, Z. H., and Chrisey, D. B. (1999). Electrical, optical, and structural properties of indium–tin–oxide thin films for organic light-emitting devices. *Journal of Applied Physics* **86**, 6451–6461.

Kirner, U., Schierbaum, K. D., Göpel, W., Leibold, B., Nicoloso, N., Weppner, W., Fischer, D., and Chu, W. F. (1990). Low and high temperature TiO_2 oxygen sensors. *Sensors and Actuators B: Chemical* **1**, 103–107.

Kosyachenko, L. A. (2011). “Solar cells: thin-film technologies.” BoD–Books on Demand.

Li, X., He, F., Liu, G., Huang, Y., Pan, C., and Guo, C. (2012). Fabrication of Ge quantum dots doped TiO_2 films with high optical absorption properties via layer-by-layer ion-beam sputtering. *Materials Letters* **67**, 369–372.

Lindgren, T., Mwabora, J. M., Avendaño, E., Jonsson, J., Hoel, A., Granqvist, C.-G., and Lindquist, S.-E. (2003). Photoelectrochemical and optical properties of nitrogen doped titanium dioxide films prepared by reactive DC magnetron sputtering. *The Journal of Physical Chemistry B* **107**, 5709–5716.

Liu, B., Wen, L., and Zhao, X. (2008a). The structure and photocatalytic studies of N-doped TiO_2 films prepared by radio frequency reactive magnetron sputtering. *Solar Energy Materials and Solar Cells* **92**, 1–10.

Liu, D., Xiao, P., Zhang, Y., Garcia, B. B., Zhang, Q., Guo, Q., Champion, R., and Cao, G. (2008b). TiO_2 nanotube arrays annealed in N_2 for efficient lithium-ion intercalation. *The Journal of Physical Chemistry C* **112**, 11175–11180.

Liu, J., Beals, M., Pomerene, A., Bernardis, S., Sun, R., Cheng, J., Kimerling, L. C., and Michel, J. (2008c). Waveguide-integrated, ultralow-energy GeSi electro-absorption modulators. *Nature Photonics* **2**, 433.

Liu, J., Sun, X., Camacho-Aguilera, R., Kimerling, L. C., and Michel, J. (2010). Ge-on-Si laser operating at room temperature. *Optics letters* **35**, 679–681.

Lu, Y.-M., Hwang, W.-S., Liu, W. Y., and Yang, J. S. (2001). Effect of RF power on optical and electrical properties of ZnO thin film by magnetron sputtering. *Materials chemistry and physics* **72**, 269–272.

Luo, Z. H., Leng, J. F., He, W. S., and Hu, D. J. (2015). Effect of Sputtering Power on Photocatalytic Activity of Thin TiO_2 Films. *In* “Materials Science Forum,” Vol. 814, pp173–177. Trans Tech Publ.

Lynch, J., Giannini, C., Cooper, J. K., Loiudice, A., Sharp, I. D., and Buonsanti, R. (2015). Substitutional or interstitial site-selective nitrogen doping in TiO_2 nanostructures. *The Journal of Physical Chemistry C* **119**, 7443–7452.

Maghanga, C. M. and Mwamburi, M. M. (2018). Contribution of Drude and Brendel Model Terms to the Dielectric Function; A case of TiO_2: Nb Thin Films. *Journal of Modeling and Simulation of Materials* **1**, 3–7.

Mardare, D., Tasca, M., Delibas, M., and Rusu, G. I. (2000). On the structural properties and optical transmittance of TiO_2 rf sputtered thin films. *Applied Surface Science* **156**, 200–206.

Martin, N., Santo, A. M. E., Sanjines, R., and Levy, F. (2001). Energy distribution of ions bombarding TiO_2 thin films during sputter deposition. *Surface and Coatings Technology* **138**, 77–83.

Matjie, R. H., Li, Z., Ward, C. R., and French, D. (2008). Chemical composition of glass and crystalline phases in coarse coal gasification ash. *Fuel* **87**, 857–869.

Mattox, D. M. (2002). Physical vapor deposition (PVD) processes. *Metal Finishing* **100**, 394–408.

Mazzolini, P., Gondoni, P., Russo, V., Chrastina, D., Casari, C. S., and Li Bassi, A. (2015). Tuning of electrical and optical properties of highly conducting and transparent Ta-doped TiO_2 polycrystalline films. *The Journal of Physical Chemistry C* **119**, 6988–6997.

Melcher, F. and Buchholz, P. (1988). 8. Germanium. *Critical metals handbook*, 177.

Mohamed, A. E. R. and Rohani, S. (2011). Modified TiO_2 nanotube arrays (TNTAs): progressive strategies towards visible light responsive photoanode, a review. *Energy & Environmental Science* **4**, 1065–1086.

Moskalyk, R. R. (2004). Review of germanium processing worldwide. *Minerals engineering* **17**, 393–402.

Muslim, N., Soon, Y. W., Lim, C. M., and Voo, N. Y. (2015). Influence of sputtering power on properties of titanium thin films deposited by rf magnetron sputtering. *ARPN Journal of Engineering and Applied Sciences* **10**, 7184–7189.

Nah, Y.-C., Paramasivam, I., and Schmuki, P. (2010). Doped TiO_2 and TiO_2 nanotubes: synthesis and applications. *ChemPhysChem* **11**, 2698–2713.

Nair, P. B., Justinvictor, V. B., Daniel, G. P., Joy, K., Ramakrishnan, V., and Thomas, P. V. (2011). Effect of RF power and sputtering pressure on the structural and optical properties of TiO_2 thin films prepared by RF magnetron sputtering. *Applied Surface Science* **257**, 10869–10875.

Naldoni, A., Allieta, M., Santangelo, S., Marelli, M., Fabbri, F., Cappelli, S., Bianchi, C. L., Psaro, R., and Dal Santo, V. (2012). Effect of nature and location of defects on bandgap narrowing in black TiO_2 nanoparticles. *Journal of the American Chemical Society* **134**, 7600–7603.

Navinšek, B., Panjan, P., and Milošev, I. (1999). PVD coatings as an environmentally clean alternative to electroplating and electroless processes. *Surface and Coatings Technology* **116**, 476–487.

Nolan, N. T., Seery, M. K., and Pillai, S. C. (2009). Spectroscopic investigation of the anatase-to-rutile transformation of sol- gel-synthesized TiO_2 photocatalysts. *The Journal of Physical Chemistry C* **113**, 16151–16157.

Ohring, M. (1992). The Materials Science of Thin Films Academic Press Inc. *San Diego*, 454.

Okuya, M., Nakade, K., and Kaneko, S. (2002). Porous TiO_2 thin films synthesized by a spray pyrolysis deposition (SPD) technique and their application to dye-sensitized solar cells. *Solar energy materials and solar cells* **70**, 425–435.

O'Leary, S. K., Johnson, S. R., and Lim, P. K. (1997). The relationship between the distribution of electronic states and the optical absorption spectrum of an amorphous semiconductor: An empirical analysis. *Journal of applied physics* **82**, 3334–3340.

O'regan, B. and Grätzel, M. (1991). A low-cost, high-efficiency solar cell based on dye-sensitized colloidal TiO_2 films. *nature* **353**, 737.

Pankove, J. I. (1975). "Optical processes in semiconductors." Courier Corporation.

Pansila, P., Witit-anun, N., and Chaiyakun, S. (2012). Influence of sputtering power on structure and photocatalyst properties of DC magnetron sputtered TiO_2 thin film. *Procedia Engineering* **32**, 862–867.

Pelaez, M., Nolan, N. T., Pillai, S. C., Seery, M. K., Falaras, P., Kontos, A. G., Dunlop, P. S., Hamilton, J. W., Byrne, J. A., and O'shea, K. (2012). A review on the visible light active titanium dioxide photocatalysts for environmental applications. *Applied Catalysis B: Environmental* **125**, 331–349.

Poruba, A., Fejfar, A., Remeš, Z., Špringer, J., Vaněček, M., Kočka, J., Meier, J., Torres, P., and Shah, A. (2000). Optical absorption and light scattering in microcrystalline silicon thin films and solar cells. *Journal of Applied Physics* **88**, 148–160.

Pulker, H. K. (1979). Characterization of optical thin films. *Appl. Opt.* **18**, 1969.

Pullar, R. C., Penn, S. J., Wang, X., Reaney, I. M., and Alford, N. M. (2009). Dielectric loss caused by oxygen vacancies in titania ceramics. *Journal of the European ceramic society* **29**, 419–424.

Rahim, M. S., Sahdan, M. Z., Bakri, A. S., Said, N. D. M., Yunus, S. H. A., and Lias, J. (2017). Effect of gas on the structural and electrical properties of titanium dioxide film. *In* "AIP Conference Proceedings," Vol. 1788, pp030134. AIP Publishing.

Randeniya, L. K., Bendavid, A., Martin, P. J., and Preston, E. W. (2007). Photoelectrochemical and structural properties of TiO_2 and N-doped TiO_2 thin films synthesized using pulsed direct current plasma-activated chemical vapor deposition. *The Journal of Physical Chemistry C* **111**, 18334–18340.

Rani, S., Roy, S. C., Paulose, M., Varghese, O. K., Mor, G. K., Kim, S., Yoriya, S., LaTempa, T. J., and Grimes, C. A. (2010). Synthesis and applications of electrochemically self-assembled titania nanotube arrays. *Physical Chemistry Chemical Physics* **12**, 2780–2800.

Rossnagel, S. M., Mikalsen, D., Kinoshita, H., and Cuomo, J. J. (1991). Collimated magnetron sputter deposition. *Journal of Vacuum Science & Technology A: Vacuum, Surfaces, and Films* **9**, 261–265.

Ru, C., Zhang, Y., Sun, Y., Zhong, Y., Sun, X., Hoyle, D., and Cotton, I. (2011). Automated four-point probe measurement of nanowires inside a scanning electron microscope. *IEEE Transactions on Nanotechnology* **10**, 674–681.

Sarantopoulos, C., Gleizes, A. N., and Maury, F. (2009). Chemical vapor deposition and characterization of nitrogen doped TiO_2 thin films on glass substrates. *Thin Solid Films* **518**, 1299–1303.

Sarkar, A., Shchukarev, A., Leino, A.-R., Kordas, K., Mikkola, J.-P., Petrov, P. O., Tuchina, E. S., Popov, A. P., Darvin, M. E., and Meinke, M. C. (2012). Photocatalytic activity of TiO_2 nanoparticles: effect of thermal annealing under various gaseous atmospheres. *Nanotechnology* **23**, 475711.

Senain, I., Nayan, N., and Saim, H. (2010). Structural and electrical properties of TiO_2 thin film derived from sol-gel method using titanium (IV) butoxide. *International Journal of Integrated Engineering* **3**, 1–35.

Shinen, M. H., AlSaati, S. A. A., and Razooqi, F. Z. (2018). Preparation of high transmittance TiO_2 thin films by sol-gel technique as antireflection coating. *In* "Journal of Physics: Conference Series," Vol. 1032, pp012018. IOP Publishing.

Song, Y., Bac, B. H., Lee, Y.-B., Kim, M. H., Yoon, W.-S., Kim, J. H., and Moon, H.-S. (2010). Ge-incorporation into 6-line ferrihydrite nanocrystals. *CrystEngComm* **12**, 1997–2000.

Stengl, V. and Bakardjieva, S. (2010). Molybdenum-doped anatase and its extraordinary photocatalytic activity in the degradation of orange II in the UV and vis regions. *The Journal of Physical Chemistry C* **114**, 19308–19317.

Štengl, V., Houšková, V., Bakardjieva, S., Murafa, N., and Bezdička, P. (2010). Niobium and tantalum doped titania particles. *Journal of Materials Research* **25**, 2015–2024.

Stengl, V., Velická, J., Maríková, M., and Grygar, T. M. (2011). New generation photocatalysts: how tungsten influences the nanostructure and photocatalytic activity of TiO_2 in the UV and visible regions. *ACS Applied Materials & Interfaces* **3**, 4014–4023.

Suda, Y., Kawasaki, H., Ueda, T., and Ohshima, T. (2004). Preparation of high quality nitrogen doped TiO_2 thin film as a photocatalyst using a pulsed laser deposition method. *Thin solid films* **453**, 162–166.

Suhail, M. H., Rao, G. M., and Mohan, S. (1992). dc reactive magnetron sputtering of titanium-structural and optical characterization of TiO_2 films. *Journal of Applied Physics* **71**, 1421–1427.

Takahashi, J., Itoh, H., Motai, S., and Shimada, S. (2003). Dye adsorption behavior of anatase-and rutile-type TiO_2 nanoparticles modified by various heat-treatments. *Journal of materials science* **38**, 1695–1702.

Tan, B. and Wu, Y. (2006). Dye-sensitized solar cells based on anatase TiO_2 nanoparticle/nanowire composites. *The Journal of Physical Chemistry B* **110**, 15932–15938.

Tang, H., Berger, H., Schmid, P. E., and Levy, F. (1994). Optical properties of anatase (TiO_2). *Solid State Communications* **92**, 267–271.

Tavares, C. J., Castro, M. V., Marins, E. S., Samantilleke, A. P., Ferdov, S., Rebouta, L., Benelmekki, M., Cerqueira, M. F., Alpuim, P., and Xuriguera, E. (2012). Effect of hot-filament annealing in a hydrogen atmosphere on the electrical and structural properties of Nb-doped TiO2 sputtered thin films. *Thin Solid Films* **520**, 2514–2519.

Theiss, W. (2012). W.Theiss Hard- and Software.

Tian, M., Mahjouri-Samani, M., Eres, G., Sachan, R., Yoon, M., Chisholm, M. F., Wang, K., Puretzky, A. A., Rouleau, C. M., and Geohegan, D. B. (2015). Structure and formation mechanism of black TiO_2 nanoparticles. *ACS nano* **9**, 10482–10488.

Tighineanu, A., Albu, S. P., and Schmuki, P. (2014). Conductivity of anodic TiO_2 nanotubes: Influence of annealing conditions. *physica status solidi (RRL)–Rapid Research Letters* **8**, 158–162.

Tiginyanu, I., Topala, P., and Ursaki, V. (2016). Nanostructures and thin films for multifunctional applications. *Editura Springer, 2016, 550 pg*.

Tong, H., Deng, Z., Liu, Z., Huang, C., Huang, J., Lan, H., Wang, C., and Cao, Y. (2011). Effects of post-annealing on structural, optical and electrical properties of Al-doped ZnO thin films. *Applied Surface Science* **257**, 4906–4911.

Tsai, T.-H., Chiou, S.-C., and Chen, S.-M. (2011). Enhancement of dye-sensitized solar cells by using graphene-TiO_2 composites as photoelectrochemical working electrode. *Int. J. Electrochem. Sci* **6**, 3333–3343.

Usha, K., Mondal, B., Sengupta, D., Das, P., Mukherjee, K., and Kumbhakar, P. (2014). Development of multilayered nanocrystalline TiO_2 thin films for photovoltaic application. *Optical Materials* **36**, 1070–1075.

Vossen, J. L., Kern, W., and Kern, W. (1991). "Thin film processes II." Gulf Professional Publishing.

Wafula, H. B., Simiyu, J., Waita, S., Aduda, B. O., and Mwabora, J. M. (2008). Effect of nitration on pressed TiO_2 Photoelectrodes for Dye-Sensitized solar cells. *AJST J. Eng. Appl. Sc.* **8**, 63–71.

Waita, S. M., Aduda, B. O., Mwabora, J. M., Granqvist, C. G., Lindquist, S.-E., Niklasson, G. A., Hagfeldt, A., and Boschloo, G. (2007). Electron transport and recombination in dye sensitized solar cells fabricated from obliquely sputter deposited and thermally annealed TiO_2 films. *Journal of Electroanalytical Chemistry* **605**, 151–156.

Wang, G., Wang, H., Ling, Y., Tang, Y., Yang, X., Fitzmorris, R. C., Wang, C., Zhang, J. Z., and Li, Y. (2011). Hydrogen-Treated TiO_2 Nanowire Arrays for Photoelectrochemical Water Splitting. *Nano Lett.* **11**, 3026–3033.

Wang, H. and Lewis, J. P. (2005). Effects of dopant states on photoactivity in carbon-doped TiO_2. *Journal of Physics: Condensed Matter* **17**, L209.

Wang, J., Mei, Y., Lu, X., Fan, X., Kang, D., Xu, P., and Tan, T. (2016). Effects of annealing pressure and Ar+ sputtering cleaning on Al-doped ZnO films. *Applied Surface Science* **387**, 779–783.

Weisstein, E. W. (2003). Eric weisstein's world of physics. *http://scienceworld. wolfram. com/physics/MoessbauerSpectroscopy. html*.

Went, M. R., Vos, M., and Werner, W. S. (2008). Extracting the Ag surface and volume loss functions from reflection electron energy loss spectra. *Surface science* **602**, 2069–2077.

Woan, K., Pyrgiotakis, G., and Sigmund, W. (2009). Photocatalytic Carbon-Nanotube–TiO_2 Composites. *Advanced Materials* **21**, 2233–2239.

Xiao, P., Liu, D., Garcia, B. B., Sepehri, S., Zhang, Y., and Cao, G. (2008). Electrochemical and photoelectrical properties of titania nanotube arrays annealed in different gases. *Sensors and Actuators B: Chemical* **134**, 367–372.

Yakuphanoglu, F., Sekerci, M., and Ozturk, O. F. (2004). The determination of the optical constants of Cu (II) compound having 1-chloro-2, 3-o-cyclohexylidinepropane thin film. *Optics communications* **239**, 275–280.

Yamada, N., Hitosugi, T., Hoang, N. L. H., Furubayashi, Y., Hirose, Y., Shimada, T., and Hasegawa, T. (2007). Fabrication of low resistivity Nb-doped TiO_2 transparent conductive polycrystalline films on glass by reactive sputtering. *Japanese Journal of Applied Physics* **46**, 5275.

Yellishetty, M., Huston, D., Graedel, T. E., Werner, T. T., Reck, B. K., and Mudd, G. M. (2017). Quantifying the potential for recoverable resources of gallium, germanium and antimony as companion metals in Australia. *Ore Geology Reviews* **82**, 148–159.

Yin, B., Wang, J., Xu, W., Long, D., Qiao, W., and Ling, L. (2013). Preparation of TiO_2/mesoporous carbon composites and their photocatalytic performance for methyl orange degradation. *New Carbon Materials* **28**, 47–54.

Yousif, A., Aadim, Dr. K., and Al-Isawi, N. (2016). Influence of Ag doping on Optical Properties of Nanocrystalline Titanium Dioxide prepared by PLD. *IOSR Journal of Applied Physics* **08**, 50–56.

Youssef, Z., Colombeau, L., Yesmurzayeva, N., Baros, F., Vanderesse, R., Hamieh, T., Toufaily, J., Frochot, C., Roques-Carmes, T., and Acherar, S. (2018). Dye-sensitized nanoparticles for heterogeneous photocatalysis: Cases studies with TiO_2, ZnO, fullerene and graphene for water purification. *Dyes and Pigments* **159**, 49–71.

Zaleska, A. (2008). Doped-TiO_2: a review. *Recent patents on engineering* **2**, 157–164.

Zeng, Y., Wu, W., Lee, S., and Gao, J. (2007). Photocatalytic performance of plasma sprayed Pt-modified TiO_2 coatings under visible light irradiation. *Catalysis Communications* **8**, 906–912.

Zhang, W., Zhu, S., Li, Y., and Wang, F. (2007). Photocatalytic Zn-doped TiO_2 films prepared by DC reactive magnetron sputtering. *Vacuum* **82**, 328–335.

Zhang, Z., Wang, C.-C., Zakaria, R., and Ying, J. Y. (1998). Role of particle size in nanocrystalline TiO_2-based photocatalysts. *The Journal of Physical Chemistry B* **102**, 10871–10878.

Zheng, Z., Huang, B., Meng, X., Wang, J., Wang, S., Lou, Z., Wang, Z., Qin, X., Zhang, X., and Dai, Y. (2013). Metallic zinc-assisted synthesis of Ti 3+ self-doped TiO_2 with tunable phase composition and visible-light photocatalytic activity. *Chemical Communications* **49**, 868–870.

Zhou, M., Yu, J., and Cheng, B. (2006). Effects of Fe-doping on the photocatalytic activity of mesoporous TiO_2 powders prepared by an ultrasonic method. *Journal of Hazardous Materials* **137**, 1838–1847.

Zhu, G., Cheng, Z., Lv, T., Pan, L., Zhao, Q., and Sun, Z. (2010). Zn-doped nanocrystalline TiO_2 films for CdS quantum dot sensitized solar cells. *Nanoscale* **2**, 1229–1232.